On dwarf galaxies and dark satellites

Tjitske Starkenburg

Supervisor:
Amina Helmi

In collaboration with:
Laura Sales
Claudio Dalla Vecchia

Kapteyn Astronomical Institute
University of Groningen

4th November 2011

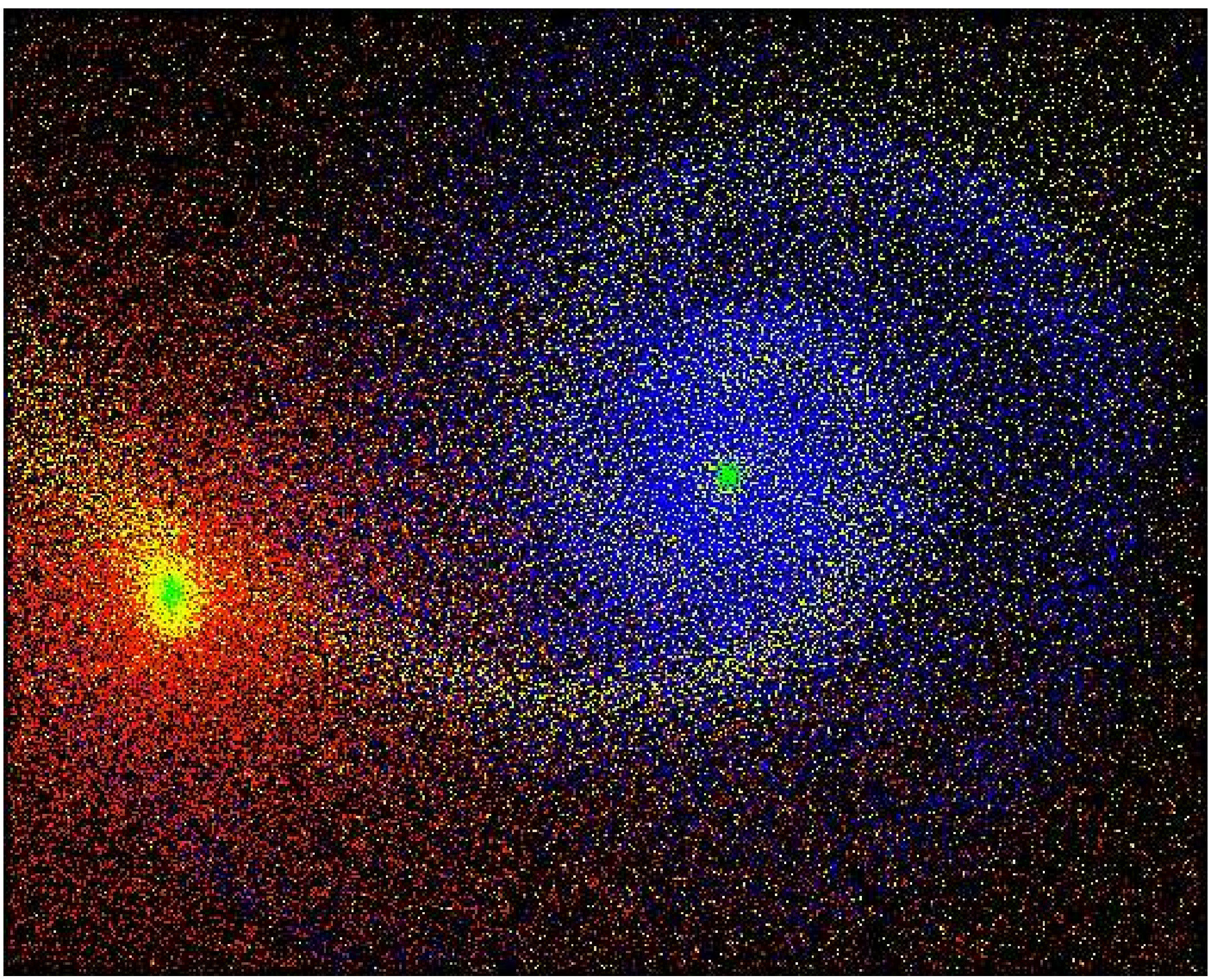

Front cover:

Snapshot from a simulation involving the a $M_{vir} = 10^{10} M_{\odot}$ *dwarf galaxy (model H4 14) and a* $M_{vir} = 2 \times 10^{9} M_{\odot}$ *dark satellite on a planar orbit. The time is 1.5 Gyr after the start of the simulation. Shown are the stellar particles in the disk of the dwarf galaxy (blue), the gas particles from the disk (yellow), the dark matter particles from the satellite (red; 50 % of the particles shown) and the gas particles of the disk of the dwarf galaxy that are forming stars at this moment (green). The dwarf galaxy has a dark matter halo and a bulge in addition which are not shown in this plot.*

Chapter 1

Introduction

1.1 Hierarchical galaxy formation

In the most favoured cosmogony today, the ΛCDM (Λ cold dark matter) model, galaxies form through hierarchical clustering. Small perturbations due to quantum fluctuations in the very early universe, grow and lead to the formation of small dark matter haloes which grow further through merging. The dark matter initially has negligible thermal velocities and a Gaussian scale-free distribution of density fluctuations and is therefore termed 'cold'. The baryonic matter falls into the small haloes at high redshift, cools and forms galaxies which then also grow through merging.

The first theoretical descriptions (e.g. Press & Schechter 1974; White & Rees 1978; Rees & Ostriker 1977) of the involved processes were soon followed by N-body simulations of the dark matter component. These simulations have contributed enormously to the popularity of the hierarchical paradigm. The evolution of dark matter structures in the universe is very well suited to N-body simulations as both the initial conditions and the evolution equations are well known. Predictions for the large-scale structure of the universe from cosmological cold dark matter simulations so far compare well with the observed large-scale structure (Springel, Frenk & White 2006; Springel et al 2005).

The success of the ΛCDM paradigm on smaller scales is still a matter of discussion. Longair (2008) describes how the first simulations seemed to show that small-scale structure was wiped-out in the accumulation and merging processes. In contrast smaller-scale objects can observationally be distinguished as for example satellites and streams in galaxy haloes and individual galaxies within galaxy clusters. This now appears to have been the result of a lack of resolution: more recent N-body simulations have highlighted the opposite problem: these are finding more 'subhaloes' than what can be accounted for by the observed galaxy luminosity function. This has become known as the 'missing satellite problem' (Klypin et al. 1999; Moore et al. 1999). Though many more very faint small systems around the Milky Way have been found since the problem was posed, there is still a discrepancy between the predicted number in simulations and the observations. Most astronomers who address this discrepancy see two possibilities: either the hierarchical cold dark matter models are incorrect or there are no missing satellites but they are below our current observational limits. Questions about the existence of a lower bound on the mass of galaxies have been there for a few decades. Arp (1965) posed it after finding a small, faint and compact galaxy and in addition wondered whether we would be able to detect the smallest, faintest galaxies. Klypin et al. (1999) suggested that observations missed a large set of satellites because these were so called dark galaxies, systems that hardly formed stars and so were very faint. The suppression of star formation could be because of supernova-driven winds or because of gas heating by the UV ionizing background during and after reionization. The dwarf satellite galaxies of the Milky Way, which are the most dark matter dominated objects known, are found to have approximately the same central density irrespective of their luminosity (Gilmore et al. 2007; Strigari et al. 2007; Strigari et al. 2008). This could indicate that there is a special threshold or scale in the formation of dwarf galaxies that indicates whether it can form stars or not. Okamoto & Frenk (2009) show that in their models there is a threshold in maximum circular velocity at reionization that divides haloes into those where gas can cool and form stars and haloes in which this cannot take place. Read, Pontzen & Viel (2006) advocate the existence of a critical mass $M_{\mathrm{crit}} \sim 10^8 M_{\odot}$ necessary for small haloes to be able to light up. This critical mass is close to the limit below which a galaxy cannot retain its gas if blown out by a supernova (Mac Low & Ferrara 1999). Secondly, this value for the critical mass roughly corresponds to the mass a halo would need to reach a virial temperature high enough to enable more efficient (atomic line) cooling for hydrogen before the epoch of reionization. There exist many models that describe how a small dark matter halo could evolve into a starless galaxy, either by the blowing out of gas by supernova-driven winds, a photoionizing background preventing star formation or a too small baryonic mass in the galaxy to develop the instabilities that lead to star formation (Dekel & Silk 1986; Mac Low & Ferrara 1998; Mac Low & Ferrara 1999; Verde et al. 2002; Davies et al. 2006; Bullock et al. 2000; Somerville 2002; Trentham et al. 2001; Ricotti 2009). The predictions from these models however, have not yet been confirmed by observations. A few ‘candidates’ for dark galaxies are discussed in the literature, in most cases an isolated HI-cloud, but most are suspected to be part of tidal features or could be high-velocity clouds (Davies et al. 2004; Kent et al. 2007; Duc & Bournaud 2008).

Another debate with respect to the predictions of ΛCDM on small scales revolves around the conviction that CDM haloes have cuspy inner density profiles. This might or might not be consistent with the rotation curves for dark matter dominated galaxies. The Aquarius Project (Springel et al. 2008) studies the structure of Galaxy-sized and smaller CDM haloes in order to address both above-mentioned subjects of discussion. In this project a suite of six different cosmological N-body simulations of the formation of Milky Way-like systems were run at different resolution levels. In the largest run the gravitational softening length is just 20.5 pc and the total number of particles is $4,397,586,154$. The simulations follow bound structures as small as $\sim 10^5 M_{\odot}$ and has enough resolution to detect several layers of substructure. This can be seen in Figure 1.1 from Springel et al. (2008). The overall substructure mass fraction however is much lower in subhaloes than in the main halo. On all scales substructures reside preferentially in the outer regions of their parent haloes and have a higher concentration than field haloes of the same mass or of the same circular velocity. These three properties can all be explained by the subhaloes being influenced by their parent halo: tidal stripping removes the outer, substructure-rich, parts of subhaloes, the subhalo does not accrete new substructures and tidal truncation and mass loss result in a higher concentration for subhaloes. The structure of dark matter haloes and their surroundings are thus highly influenced by hierarchical clustering and the process of merging.

1.2 Dwarf galaxies

One advantage of working on dwarf galaxies is that several are so nearby that reasonably detailed information is available on the properties of individual stars. Moreover dwarf galaxies give the opportunity to study galaxy formation and evolution on a small scale. On the other hand many, and especially the nearest dwarf galaxies known, are also satellites and thus influenced by a more massive system. One can deliberate long about the correct definition of a dwarf galaxy. Here we will only mention a working definition used in the review on dwarf galaxies in the local group by Tolstoy, Hill & Tosi (2009): a dwarf galaxy is a system fainter than $M_V \leq -17$ and is more spatially extended than globular clusters (Tamman 1994). This roughly coincides with the mass limit at which the baryonic content of the galaxy could be affected by outflows (Tolstoy, Hill & Tosi 2009). One can distinguish at

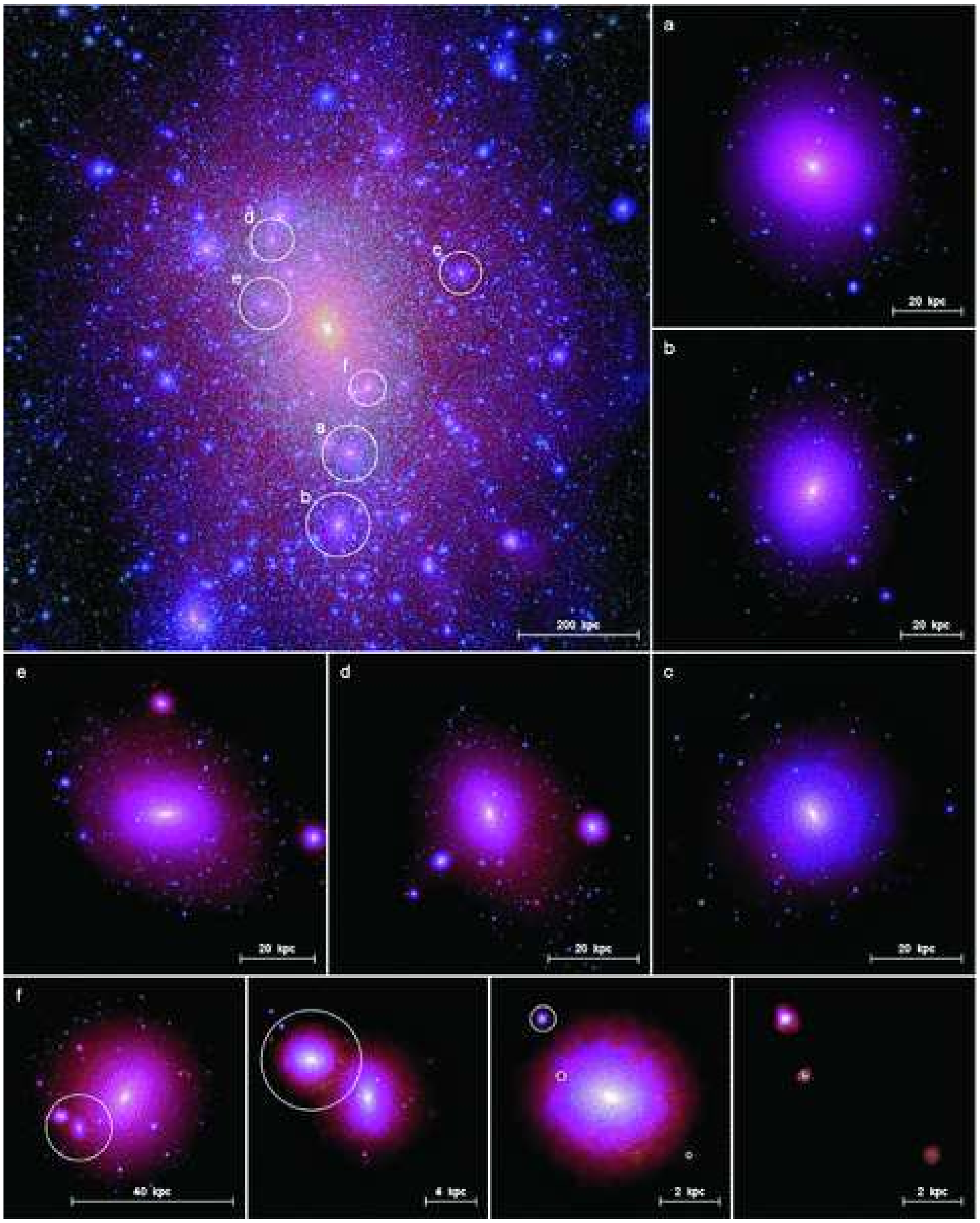

Figure 1.1: *Figure 13 from Springel et al. (2008): "Images of substructure within substructure. The top left-hand panel shows the dark matter distribution in a cubic region of side* $2.5 \times r_{50}$ *centred on the main halo in the Aq-A-1 simulation. The circles mark six subhaloes that are shown enlarged in the surrounding panels, and in the bottom left-hand panel, as indicated by the labels. All these first generation subhaloes contain other, smaller subhaloes which are clearly visible in the images. SUBFIND finds these second generation subhaloes and identifies them as daughter subhaloes of the larger subhaloes. If these (sub)subhaloes are large enough, they may contain a third generation of (sub)subhaloes, and sometimes even a fourth generation. The bottom panels show an example of such a situation. The subhalo shown on the bottom left-hand side contains another subhalo (circled) which is really made up of two main components and several smaller ones (bottom, second from left-hand side). The smaller of the two components is a third generation substructure (bottom, third from left-hand side) which itself contains three subhaloes which are thus fourth generation objects (bottom right-hand side)."* r_{50} *here denotes the radius at which the mean enclosed overdensity of the halo is 50 times the critical density at that redshift.*

least two types in this regime, of which the two and best known are the early type dwarf-spheroidals (dSphs) and the late-type star-forming dwarf irregulars (dIrrs). Additionaly centrally concentrated actively star forming and extreme compact dwarfs have been discovered in the last decade (BCDs (blue compact dwarfs) and UCDs (ultra-compact dwarfs)), more recently joined by the very-low surface brightness, ultrafaint dwarfs (uFds). The ultra-compact dwarfs populate the region, or boundary, between dwarf galaxies and globular clusters. Their compactness is comparable to that of globular clusters but they are identified to be dwarf galaxies from spectra (Tolstoy, Hill & Tosi 2009). Basic properties of a number of types of galaxies are compared in Figure 1.2 from Tolstoy, Hill & Tosi (2009).

On the high-mass end of the dwarf galaxy spectrum the boundary is even more ambiguous, as can be seen in Figure 1.2. There is no clear break between the late-type and spheroidal dwarfs on one side, and the larger late-type galaxies on the other. And while there is a clear, physically founded, distinction between properties of elliptical and spirals, this is not the case for the dwarf galaxies. In addition, due to the large range in distance, surface brightness, concentration and size, the techniques and the difficulty in studying dwarf galaxies varies significantly. Kinematics and metallicity for irregulars are for instance quite easily obtained using their interstellar medium while this is not possible for dwarf spheroidals. Almost all we know about the dwarf spheroidals kinematic properties and metallicity is from their evolved stellar populations which are harder to study in the more distant late-type dwarfs (Tolstoy, Hill & Tosi 2009). This difference in amount and detail of the data greatly complicates the understanding of dwarf galaxies and the relation between their properties and the different classes (Walker et al. 2009).

Dwarf galaxies in general are found to have higher mass-to-light ratios than the normal spirals or ellipticals. The dwarfs form stars less efficiently and have problems accreting new gas (if they become satellites) and keeping their own due to their smaller mass. Figure 1.3, from Sales et al. (in prep.), shows the galaxy efficiency $\eta_{\rm gal} = M_{\rm d}/(M_{\rm vir} f_{\rm baryons})$, where M_d is in this case the amount of baryons collected by the galaxy and $f_{\rm baryons}$ is the universal baryon fraction, as a function of halo mass. This relation has been obtained combining the Aquarius simulations and a semi-analytic model of galaxy formation (Starkenburg et al. 2011). It can clearly be seen that the galaxy efficiency is much lower for halo masses about and below $10^{10} M_{\odot}$. A significant fraction of the haloes of this size have quite some gas but do not form many stars. Dwarf galaxy stellar population analysis and star formation histories in simulations, on the other hand, have shown that many dwarfs probably possess a bursty star formation history (Stinson et al. 2007; Pelupessy, van der Werf & Icke 2008; Wadepuhl & Springel 2011; Okamoto et al. 2010). This bursty behaviour is suggested to originate from internal as well as external processes. Supernova outflows due to strong star formation might inhibit star formation in a dwarf galaxy untill the gas has fallen back and cooled. But mergers and accretion processes could just as well be a cause for a sudden episode of enhanced star formation. In the Aquarius simulations it has been found that the small dark matter haloes (and even subhaloes) have substructures themselves (see Figure 1.1) and that they merge with similar and smaller subhaloes before falling into the bigger systems. Therefore, in the context of the ΛCDM paradigm the above considerations mean that the substructures falling into a small dark matter halo must be predominantly dark.

For our research we are interested both in the dwarf irregulars and the dwarf spheroidals. The latter systems are usually devoid of gas and dominated by old and intermediate-age stars, though their star formation histories seem to be complex. The radial light profiles of spheroidals are shallow and can be fitted by various functional forms, all declining at large radii. The spheroidals are generally thought not to be rotational supported, even though they can appear flattened, but whether this is actually true for all known spheroidals is not yet clear. These small galaxies seem to have low densities of luminous matter but high total mass densities and are mainly found in dense cosmic environments. They may seem to be related to the large elliptical galaxies but while a consensus

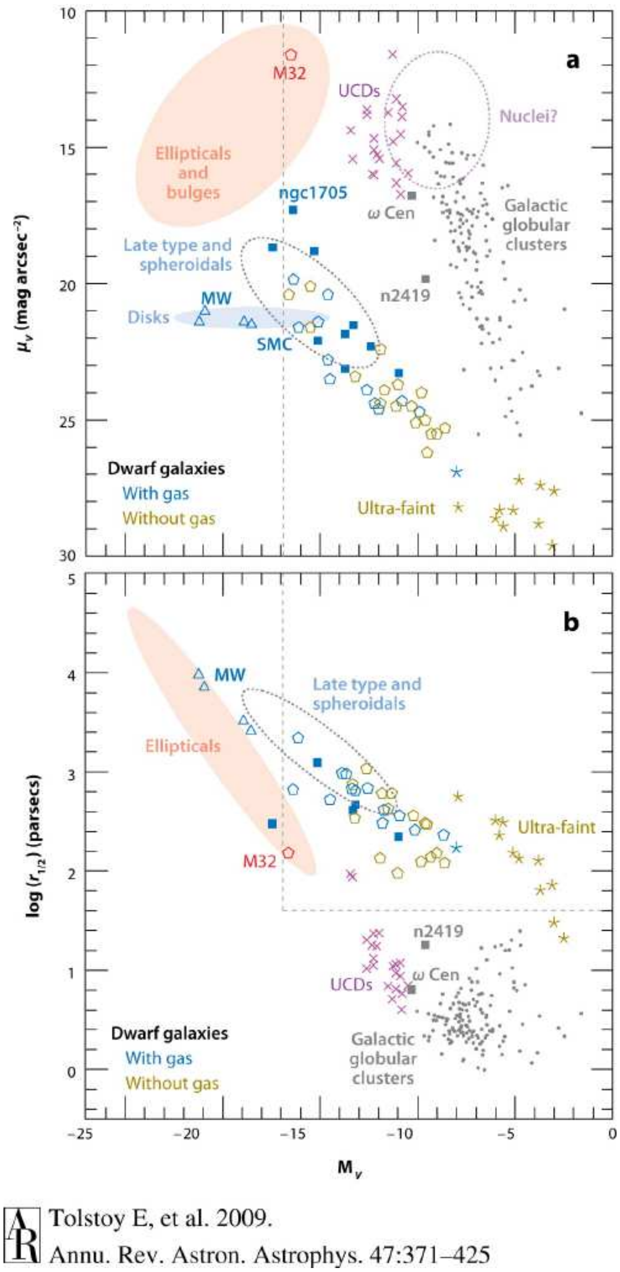

Figure 1.2: *Figure 1 from Tolstoy, Hill & Tosi (2009): "Here are plotted the relationships between structural properties for different types of galaxies (after Kormendy 1985), including as dotted lines the classical limits of the dwarf galaxy class as defined by Tammann (1994). (a) The absolute magnitude, MV, versus central surface brightness, μV, plane; (b) The MV versus half light radius,* $r_{1/2}$*, plane. Marked with colored ellipses are the typical locations of elliptical galaxies and bulges (light red), spiral galaxy disks (light blue), galactic nuclei (dashed purple), and large early-(spheroidals) and late-type systems (dashed gray). Galactic globular clusters are plotted individually as small gray points. M31, the Milky Way (MW), M33 and LMC are shown as blue open triangles. Some of the blue compact dwarfs with well-studied color-magnitude diagrams are marked as blue solid squares. The peculiar globular clusters ω Cen and NGC 2419 are marked close to the globular cluster ellipse, M32 in the region of elliptical galaxies, and the SMC near the border of the dwarf class. The ultracompact dwarfs (UCDs) studied in the Virgo and Fornax clusters are marked with purple crosses. Local Group dwarf galaxies are plotted as open pentagons, blue for systems with gas, and yellow for systems without gas. The recently discovered ultrafaint dwarfs are given star symbols, and the same color code." For references see Tolstoy, Hill & Tosi (2009).*

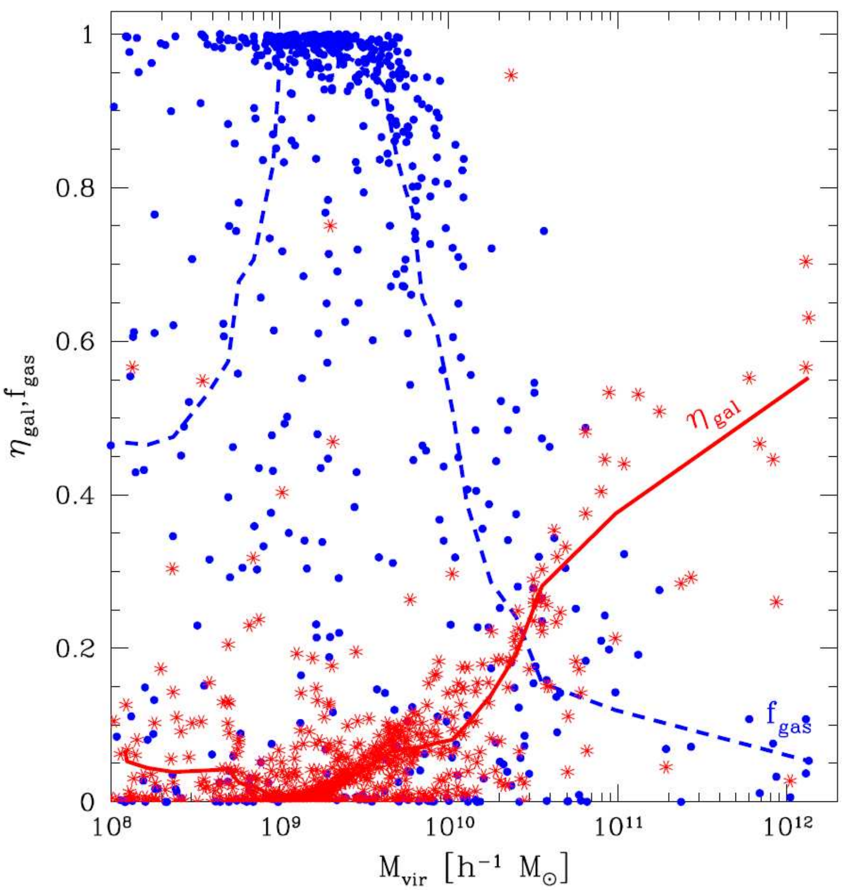

Figure 1.3: *From Sales et al. in prep.: Gas fraction f_{gas} (blue circles) and galaxy formation efficiency η_{gal} (red asterisks) for our model galaxies as a function of host mass, as predicted by our semi-analytic model. The dashed blue and solid red curves indicate the respective median trends. The data comes from a semi-analytic model by Starkenburg et al. (2011) based on the Aquarius suite of simulations.*

more or less exists for the formation of large ellipticals through the mergers of spirals, the formation of spheroidal dwarf galaxies is still a matter of debate. Grebel, Gallagher & Harbeck (2003) mention three, not necessarily independent, scenarios which are subject of discussion in the literature. The spheroidals could have lost their gas on the way or have been prevented to form new stars through the same physical processes (reionization, feedback, environment) that have affected the lowest mass dark matter halos (Larson 1974; Dekel & Silk 1986). This has also been found through simulations to be a possible trajectory for the genesis of the Local Group dwarf spheroidals (Sawala et al. 2011) and probable blown-outs have been observed (Young et al. 2007; Wilman et al. 2005). Another suggestion is that the spheroidal dwarfs are fragments of larger galaxies, expelled during heavy interactions or mergers (Gerola, Carnevali & Salpeter 1983) or developed in tidal tails (see for instance the discussion around the object VIRGOHI 21 (Davies et al. 2004; Kent et al. 2007; Duc & Bournaud 2008)). Take the opposite perspective: some recently found ultra-faint dwarf galaxies close to the Milky Way may be related to streams, for example from Sagittarius, within the Milky Way halo and could therefore also be overdensities along those streams instead of original dwarf galaxies (Tolstoy, Hill & Tosi 2009). The third suggestion is that the spheroidals were originally irregular, field, dwarf galaxies but lost their gas and became rotation-free spheroidal galaxies due to ram-pressure stripping and tidal interactions (e.g. Kormendy 1985; Sofue 1994; Mayer et al. 2001a, 2001b).

All the scenarios described above have their pros and cons. Regarding the idea of irregulars becoming spheroidals, arguments against it mainly revolve around two exceptional spheroidals in the Local Group and the apparantly lower metallicity of spheroidal dwarf galaxies in comparison to irregular dwarfs (Grebel, Gallagher & Harbeck 2003). Two of the spheroidals in the Local Group, Tucana and Cetus, are quite distant from any of the larger galaxies. They posses the same characteristics as the spheriodals close to, or in, the Milky Way or M31 halo but are out of reach for significant tidal forces. There are, however, still counter-arguments to this problem. It could be that both Tucana and Cetus did interact with other members of the Local Group but ended up on the edge of the Group (Kazantzidis et al. 2011). They could for example be ejected due to three-body interactions (Sales et al 2007). With respect to the metallicity difference, that seems to be due to the difference in measuring the metallicity for the respective types. As for irregular dwarfs the metallicity data comes from the HI gas and star formation regions the metallicity is naturally higher than that found in the dwarf spheroidals, old or intermediate-aged, evolved stars. The dwarf irregulars are generally too distant to be able to observe individual stars with satisfying precision. Furthermore, as the spheroidals are devoided of young stars, no 'current' metallicity can be obtained for them. On top of this, if the trlations found in dwarf spheroidals for metallicity with respect to stellar age are expanded to younger stars, the young stars in dwarf irregulars seem to fit in. In that light spheroidals could very well be dwarf irregulars that lost their gas (Tolstoy, Hill & Tosi 2009).

Overall it looks like the dwarf galaxies around us have been severely influenced by external or internal 'tidal' interactions. Not only can they be affected by the tidal forces due to confrontations with, or even accretion by, much more massive galaxies, following the ΛCDM paradigm the smaller galaxies or subhaloes should also encounter similar-sized subhaloes and accrete much smaller, possibly dark, subsubhaloes themselves. Even these haloes that have not been able to form stars might have influenced the evolution of dwarf galaxies around the Milky Way.

1.3 Merging galaxies

In the hierarchical paradigm baryonic matter falls into dark matter haloes, forms galaxies and grows through merging, just like their host haloes. The tidal torques that arise in this process often give rise to tidal bridges, tails, and streams of stars during the interaction. A pair of interacting galaxies during an encounter will convert a part of their orbital energies into random motions of their individual stars. For mergers where the respective galaxies are of comparable size, major mergers, this process can be quite spectacular as the orbits decay so quickly that the galaxies are merged in a few crossing times. This process of a major merger has been well studied in numerical simulations and it has been demonstrated that major mergers between spiral galaxies generally produce remnants that resemble elliptical galaxies, which are pressure supported and whose projected mass distributions scale as $\sim r^{1/4}$ (e.g. Cox et al. 2008; Barnes & Hernquist 1992). This idea that elliptical galaxies may just be the byproduct of major mergers of spirals is commonly known as the 'merger hypothesis' (Toomre 1977). The major mergers, between spirals as well as ellipticals, answered the question of the morphological origin of the objects formerly known as peculiars, from Arp's Atlas of peculiar galaxies (Arp 1966). These galaxies were found to have tails and bridges or other highly irregular structures and seemed highly disturbed. By simulating the dynamics of interactions they were found to resemble the observations at different stages of the merging process. Simulations of interacting galaxies could explain not only the bridges and tails of peculiar galaxies but also the ongoing processes within the galaxies and the behaviour of the dark matter halo and the spheroid before, during and after the interaction or merger. These kind of simulations have given a tremendous insight in galaxy formation and evolution (e.g. Toomre & Toomre 1972; Barnes & Hernquist 1992; Cox et al. 2008).

Apart from the purely dynamical effects on the dark matter, stars and gas, mergers are also often characterized by starbursts. Just like the stars, the gas also responds to the tidal field. Bournaud (2011) describes the response of the gas and the star formation in interactions and mergers. The disruptive tidal field of a companion galaxy can expell material and create tidal tails. However, if the merger is more advanced and the galaxies begin to overlap the tidal field can become compressive. The main culprit for the development of long tidal tails and central gas inflows, is the reaction of the gas disk on the tidal forces which reveal themselves as gravitational torques. These torques originate from the symmetry-breaking of the potential by the tidal field and can for instance create an interaction-driven pair of grand-design spiral arms. Inside corotation the gas concentrates on the leading side of the valley of the potential while outside corotation the gas concentrates on the trailing side, thus creating a spiral pattern. Related is the observed inflow of gas to the center in mergers. This is more pronounced in barred galaxies but a spiral arm can also develop a tidal bar which channels gas into the central region. Inside corotation the gas undergoes negative torques, therefore looses angular momentum and flows rapidly into the central region of the galaxy. This inflow then might be able to power a nuclear starburst. Outside corotation the gas gains angular momentum and flows out to larger radii in the long tidal tails which we recognised as merger characteristics (Bournaud 2011). Di Matteo et al. (2007, 2008) studied a suite of merger simulations and found that while some cases could power a very strong starburst (increasing their star formation rates (SFRs) by factors of 10-100) most interacting galaxies only increase their SFR by a factor of a few and this increase only lasts for a few Myr. Couterintuitive, the star formation enhancement by the merger was found to be less if the first pericentric passage was very close and with strong tidal fields. This is explained by observing that if the first pericentric passage causes a very strong reaction in the disk, there will be less gas in the disk to fuel the starburst later on in the merger.

If one of the galaxies is much smaller than the other the merger is called a minor merger. From the moment the secondary galaxy is inside the virial radius of the main object, it will slowly be stripped of its dark matter halo and stars and eventually be torn apart and absorbed by the main halo and galaxy. The stripped satellites are expected to wrap around the host galaxy in streams throughout the halo (e.g. Helmi & White 2001; Mayer et al. 2002). But although the infalling satellite is so much smaller than the primary, it still can have a large influence on the main galaxy (Quinn & Goodman 1986), causing fine structures as 'shells', 'ripples', 'plumes', boxy isophotes, 'X-features' (Barnes & Hernquist 1992), heating and warping of a disk (Toth & Ostriker 1992; Quinn, Hernquist & Fullager 1993;

Walker, Mihos & Hernquist 1997; Huang & Carlsberg 1997; Velázquez & White 1999) and possibly bulge formation (e.g. Barnes & Hernquist 1992; Quinn, Hernquist & Fullagar 1993; Schweizer 1990). Cox et al. (2008) describe it as: "... it is likely that the more prevalent minor mergers give rise to the wide variety of galaxy morphology that defines many classification systems". An increasing amount of these varying effects of minor mergers, stellar streams, thick disks and other fine structures in disks and haloes, are indeed found in the Local Universe (e.g. Ibata et al. 2001ab; Dalcanton & Bernstein 2002; Bekki & Chiba 2006).

The strength of the effect that the minor merger, or accretion event, has on a galaxy however, seems to be related to the mass ratio between the merging galaxies. Merging events with smaller companions will cause less strong starbursts (Cox et al. 2008) and less heating (Toth & Ostriker 1992). Moreover the effect a minor merger has on the primary galaxy also strongly depends on the structure and composition of the galaxies and the characteristics of the encounter. Gas-rich mergers will produce stronger star formation enhancements and the presence of a bar, or the occurance of a bar instability during the encounter, will drive gas to the center more efficiently (Di Matteo et al. 2007). Not all mergers result in a starburst, as explained earlier. The presence of strong tidal fields can even work against star formation enhancement as they can remove a large amount of gas from the galaxy disks early in the merger. The ejected gas is then only partly re-accreted in a much later stage of the merging event.

The realization that minor mergers could heat a disk is now used to explain the existence of thick disks in galaxies, including the Milky Way (e.g. Villalobos & Helmi 2008). Toth & Ostriker (1992) derived an analytic relation between mass ratio of the merging galaxies and the amount of disk heating induced in the primary. Assuming a circular orbit and a local energy deposition in the primary they estimate the drag on the satellite by the disk and the halo of the primary using Chandrasekhar's formula

$$F_{\mathrm{drag}} = \frac{4\pi G^2 M_{\mathrm{sat}}^2 \rho(v < v_{\mathrm{rel}}) \ln\Lambda}{v_{\mathrm{rel}}^2} \tag{1.1}$$

where v_{rel} is the relative velocity of the disk or halo particles with respect to the satellite particles and $\ln\Lambda$ is the Coulomb logarithm (~ 1 for both the halo and the disk). For the part of the energy that is deposited in the disk the local virial theorem is used to estimate the response of the disk, using the thin-disk approximation. The part of the energy that is added to the vertical energy density of the disk will cause a thickening of the disk. For the Mestel disk Toth & Ostriker give as working example this becomes

$$\Delta H^{(\text{Mestel disk})} = \left(\frac{0.49 R_{\text{at the sun}}}{1 + 4.34 H/r}\right) \left(\frac{M_{\mathrm{sat}}}{M_{\text{disk, at the sun}}}\right) \tag{1.2}$$

where the numerical term on the right hand mostly comes from a correction by the halo. For a Mestel disk this can be rewritten as dependent on the circular velocity and the vertical velocity dispersion

$$\left(\frac{\Delta H}{H}\right)^{(\text{Mestel disk})} \simeq 0.0814 \left(\frac{v_{\mathrm{circ}}}{\sigma_z}\right)^2 \left(\frac{M_{\mathrm{sat}}}{M_{\mathrm{disk}}(r)}\right). \tag{1.3}$$

Toth & Ostriker used this relation as an argument that the high merger rate predicted by the CDM paradigm could not be realistic as the percentage of galaxies with a thin, cold disk would then be much lower than the percentage that is observed in the local universe. This idea placed a constraint on the impact minor mergers could have on disks. After this claim more numerical simulations of 'sinking in' satellites were performed with varying results. Widely different initial conditions and codes seemed to lead to very different results. Walker, Mihos & Hernquist (1996) found that a satellite of 10 per cent of the disk mass caused a thickening of 60 per cent of the stellar disk at the solar circle while Huang & Carlberg (1997) found that satellites up to 20 per cent of the disk mass on nearly-circular orbits produce no observable thickening of the disk. Further studies were performed by, among others, Velázquez & White (1999), Font et al. (2001), Hopkins et al. (2008), Qu et al. (2011), Moster et al. (2010) and Purcell, Kazantzidis & Bullock (2009). The main objective of most of these studies was to explore a suite of accretion events more realistically than done before. Criticism on older simulations was for instance the fact that most satellites were set on circular or nearly-circular orbits while now radial orbits are argued to be much more realistic (Kazantzidis et al. 2009; Hopkins et al. 2008). Also the inclusion of gas in the primary disk can influence the disks response to a satellite accretion (e.g. Moster et al. 2010). Hopkins et al. advocate that as an infalling satellite is generally on a radial orbit instead of a nearly-circular one, and as the orbit will decay more violently than the smooth circular decay Toth & Ostriker used, the energy lost by the satellite and deposited locally in the host should go quadratically with the satellite mass instead of linearly. This means that the thickening of the disk also should depend quadratically on the ratio between the mass of the satellite and the mass of the disk. Hopkins et al. come to the relation

$$\frac{\Delta H}{R_{\mathrm{e,disk}}} \propto (1 - f_{\mathrm{gas}}) \left(\frac{M_{\mathrm{sat}}}{M_d} \right)^2 . \tag{1.4}$$

This means that the effect of minor mergers on disks should be much less than expected if the relation is linear. A number of papers have tried to compare different simulations to look for a general trend. Hopkins et al. combine simulations from Villalobos & Helmi (2008), Younger et al. (2008) and Velázquez & White (1999) arguing that the trend in these simulations supports a quadratic relation. Kazantzidis et al. (2009) on the other hand mention that the thickening in their simulations is significantly more than predicted by the quadratic relation of Hopkins et al. They furthermore argue that the used simulations have an initial too thick disk making the minor merger less efficient in thickening it further. For a ‘proper’, thin, disk the thickening would have been larger, according to Kazantzidis et al. Velázquez & White on the other hand argue that the thickening predicted by Toth & Ostriker is much too high compared to what they find in their simulations.

Purcell, Kazantzidis & Bullock employ simulations of mergers in the regime of mass ratios $\sim 1:10$, according to them common in the merger history of Milky Way-like galaxies. More precisely, their satellite has a mass $M_{\mathrm{sat}} \simeq 3M_{\mathrm{host\ disk}}$. The results of Purcell, Kazantzidis & Bullock show that for all different orbits the host disk is thickened by roughly a factor 3 with respect to its initial thickness. This is much more than Villalobos & Helmi find for similar mass ratios. One reason for this might be that Villalobos & Helmi have thicker disks initially, for a vertical distribution described by $\mathrm{sech}^2\left(\frac{z}{2z_0}\right)$ Villalobos & Helmi initially have $z_0 = 0.35$ kpc while Purcell, Kazantzidis & Bullock use $z_0 = 0.215$ kpc. Moster et al. constructed similar host disks to Purcell, Kazantzidis & Bullock, purposely to be able to compare the results fairly. They also perform similar simulations using a thinner host disk. This shows that while the initial disk is thinner the final scaleheight is similar, so thicker disks are more robust to accretion events. Moster et al. also compare disk with a gas component to disks without gas, and argue that the presence of gas reduces the final scaleheights of disks due to absorption of kinetic impact energy by the gas. However, even while the gasless disks of Moster et al. have similar properties to the disk of Purcell, Kazantzidis & Bullock, they find a final thickening of a factor of ~ 2 with respect to the initial thickness instead of the factor ~ 3 found by Purcell, Kazantzidis & Bullock. Parameters that are suggested to partly explain this discrepancy are the exact masses of the disk and satellite (dark matter and stellar mass), the profiles and concentrations for the stellar and dark matter components and the initial conditions regarding the velocity dispersions as well as the simulation code itself.

This study is also partly aimed at studying the heating of disks through minor mergers. There is however a big difference with previous studies. Up untill now most simulation studies dealing with minor mergers involved dwarf galaxies falling into a Milky Way-like host galaxy. Mergers of dwarf galaxies with comparable and smaller objects are hardly ever studied. A smaller halo falling into a dwarf galaxy probably has a mass in the regime that is expected not to be able to form stars. This means that minor mergers for dwarf galaxies should predominantly be with dark satellites. A dark satellite falling into the halo of a dwarf galaxy might thus be able to heat and thicken the dwarf galaxy's disk and might even cause a starburst. Multiple occurences of these events during the lifetimes of the known dwarf galaxies could have an effect on in the characteristics and morphologies of dwarf galaxies as we observe them now in the Local Group.

1.4 Outline of this thesis

This thesis describes simulations of mergers of a dwarf galaxy and a dark satellite. The above introduction has explained the background of hierarchical galaxy formation, the morphology and kinematics of dwarfs in our Local Group and the process of merging. The detailed methods used in our simulations and a description of their initial conditions can be found in Chapter 2. Then, in Chapter 3, we will describe the results of the simulations of isolated dwarf galaxies. The merger cases will be described in Chapter 4 and 5. These results will then be summarized in Chapter 6 where the main conclusions of this study are presented.

Chapter 2

Methods

To investigate the result of mergers between dwarf galaxies and their satellites we carry out a set of 'controlled' simulations, i.e. in isolation. The initial conditions and parameters in the simulations are motivated by previous studies from the literature. To estimate the probability of a significant merger between a dark satellite and a dwarf galaxy we have analysed the Aquarius simulations, a suite of cosmological dark matter simulations with very good resolution (Springel et al. 2008). In order to have a significant effect on the dwarf galaxy the merger is required to have a mass ratio of about $M_{\text{vir, sat}}/M_{\text{vir, main}} \sim 0.2$ and to occur while the system was in isolation. Further requirements were that the host ends up as a Milky Way-like satellite and that it is supposed to host a luminous galaxy according to semi-analytic models based on the Aquarius simulations (Starkenburg et al. 2011). The properties of the satellite and its host, in Aquarius, formed the basis of the simulations' setup. These properties included the virial mass and virial radius of the host dark matter halo at time of infall of the satellite and $z = 0$, the time of infall, position and velocity of the satellite with respect to the host and the mass of the satellite at the time of infall. The time of infall refers to the moment at which the satellite crosses the virial radius of its host halo (and it does not leave the host halo again). The orbit of the selected satellite around a dwarf halo in the Aquarius-C simulation can be found in Figure 2. The dotted line shows the virial radius of the dwarf sized dark matter subhalo in the Aq-C-2 simulation. The dashed line with data points then show the smaller dark matter halo falling in. Data describing this infall are given in table 2.1. Both the plot and the data are provided by Laura Sales.

t_{infall} (Gyr)	6.14
M_{vir} main at infall time ($M_\odot$ h^{-1})	6.64×10^9
r_{vir} main at infall time (kpc h^{-1})	21.88
M_{vir} main final ($M_\odot$ h^{-1})	8.47×10^9
r_{vir} main final (kpc h^{-1})	33.14
position satellite (kpc h^{-1})	−6.30 11.96 19.17
velocity satellite (km s^{-1})	19.05 −23.20 −3.96
M_{vir} satellite at infall time ($M_\odot$ h^{-1})	5.96×10^8

Table 2.1: *Data describing the masses, position and velocities of the dark satellite and host dwarf galaxy at the point where the satellite crosses the virial radius of the host. Provided by Laura Sales.*

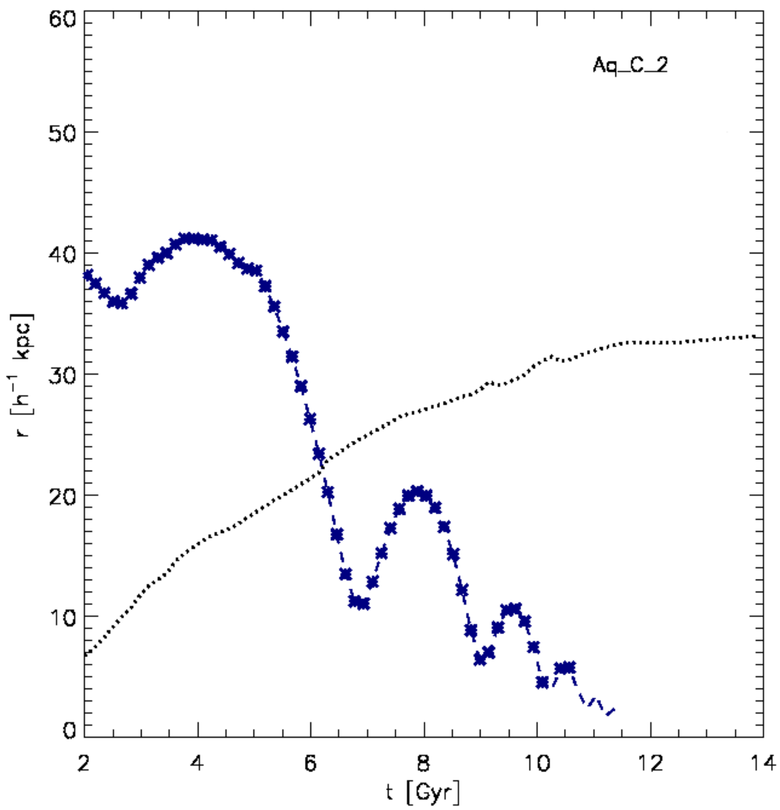

Figure 2.1: *Orbit of a dark satellite falling into a dwarf size dark matter halo in the Aquarius simulation Aq-C-2. The dotted line shows the virial radius of the subhalo on which the plot is centered. From Laura Sales.*

2.1 Simulations

The simulations of a dark satellite merging with a dwarf galaxy in isolation were performed using a modified version of the N-body TreePM/SPH code GADGET (Springel, Yoshida & White 2001; Springel et al. 2005). The code was modified to include the star formation process and supernova feedback by Schaye & Dalla Vecchia (2008) and Dalla Vecchia & Schaye (2008), respectively. Essentially all cosmological codes following the dark matter structure formation represent a collisionless fluid (dark matter) by particles. The difference between the codes is thus how the gravitational field is computed. GADGET is mostly a TreeSPH code (Hernquist & Katz 1989) which uses a hierarchical multipole expansion to compute the gravitational interactions and uses smoothed particle hydrodynamics (SPH) to follow the gas dynamics. This means that here the gas is also represented by particles. The gravitational force of distant particles is then found by grouping these particles into ever larger cells. Their gravity is then accounted for by a single multipole force which reduces the computational costs from $\mathcal{O}(N^2)$ to $\mathcal{O}(N \log N)$ with respect to direct summation methods. The TreeSPH method gives only an approximation of the true force but the error of the computation can be controlled by changing the opening criterion of the tree: one can reach higher accuracy by walking the tree to lower levels.

GADGET also offers the possibility to work with a TreePM code for computing the gravitational field. A hierarchical tree algorithm has no intrinsic resolution limit but it can be slower than a particle-mesh (PM) method. The latter works better on longer ranges but has problems on smaller scales related to the mesh size used. Xu (1995) developed a method to combine both algorithms by computing the long-range gravitational force by means of a PM algorithm while a hierarchical tree algorithm is used on short-range scales. This method is also implemented in GADGET. SPH is a Lagrangian method for following the physical processes affecting the gas. The advantage of Lagrangian methods in cosmological simulations over Eulerian methods (mesh codes) is that a wide dynamic range can be studied as the resolution is automatically increased in higher density regions. There are, however, newer mesh codes that can handle a higher dynamical range by using adaptive mesh refinement (AMR codes). A disadvantage of SPH is that it uses artificial viscosity. This results in the shocks not having their true discontinuities but being broadened by the artificial viscosity over the SPH smoothing scale. One the other hand, some mesh codes make also use of artificial viscosity.

2.1.1 Smoothed particle hydrodynamics

Smoothed particle hydrodynamics (SPH; Gingold & Monaghan 1977; Lucy 1977; Monaghan 1992) uses particles to sample a fluid in a Lagrangian sense. The continuous fluid quantities are then being defined by a kernel interpolation technique. How SPH is implemented in GADGET2 is summarized by Springel (2005). GADGET2 (and 3) define the thermodynamic state of each fluid element by a function of the entropy per unit mass $A \equiv P/\rho^{\gamma} = A(s)$. For a fluid particle with coordinates $\mathbf{r}_i$, velocity $\mathbf{v}_i$ and mass m_i the density estimate that GADGET uses is

$$\rho_i = \sum_{j=1}^{N} m_j W(|\mathbf{r}_{ij}|, h_i) \tag{2.1}$$

where $\mathbf{r}_{ij} \equiv \mathbf{r}_i - \mathbf{r}_j$, and $W(r,h)$ is the SPH smoothing kernel which is set to the spline kernel (Monaghan & Lattanzio 1985). $W(r,h)$ is also used for the collissionless particles to smooth the single particle density distribution with the normalized gravitational softening kernel ϵ, $\tilde{\delta}(\mathbf{x} = W(|\mathbf{x}|, 2.8\epsilon)$.

$$W(r,h) = \frac{8}{\pi h^3} \begin{cases} 1 - 6\left(\frac{r}{h}\right)^2 + 6\left(\frac{r}{h}\right)^3, & 0 \leq \frac{r}{h} \leq \frac{1}{2}, \\ 2\left(1 - \frac{r}{h}\right)^3, & \frac{1}{2} < \frac{r}{h} \leq 1, \\ 0, & \frac{r}{h} > 1. \end{cases} \tag{2.2}$$

In the GADGET formulation of SPH the adaptive smoothing radius h_i is defined such that a kernel volume of a particle contains a constant mass for the estimated density of that particle: $\frac{4\pi}{3} h_i \rho_i = N_{\rm sph}\bar{m}$ where $\bar{m}$ is an average particle mass and $N_{\rm sph}$ is the typical number of smoothing neighbours. Then the additional equations to describe reversible fluid dynamics in SPH become

$$\frac{\mathrm{d}\mathbf{v}_i}{\mathrm{d}t} = -\sum_{j=1}^{N} m_j \left(f_i \frac{P_i}{\rho_i^2} \nabla_i W(|\mathbf{r}_{ij}|, h_i) + f_j \frac{P_j}{\rho_j^2} \nabla_i W(|\mathbf{r}_{ij}|, h_j) \right) \tag{2.3}$$

where the coefficients f_i are

$$f_i = \left(1 + \frac{h_i}{2\rho_i} \frac{\partial \rho_i}{\partial h_i} \right)^{-1} \tag{2.4}$$

and

$$P_i = A_i \rho_i^{\gamma}, \tag{2.5}$$

the equations of motion and the particle pressure respectively.

As already metioned, SPH needs artificial viscosity to describe shocks in a fluid. To this end a viscous force is implemented in GADGET

$$\frac{\mathrm{d}\mathbf{v}_i}{\mathrm{d}t}\Big|_{\rm visc} = -\sum_{j=1}^{N} m_j \Pi_{ij} \nabla_i \bar{W}_{ij} \tag{2.6}$$

where $\Pi_{ij} \leq 0$, and $\Pi_{ij} \neq 0$ only when particles approach each other in physical space. Π_{ij} is defined in a parametrization as derived by Monaghan (1997) using a signal velocity v_{ij}^{sig} between two particles:

$$\Pi_{ij} = \begin{cases} -\left(\frac{\alpha}{2}\right)\frac{w_{ij}v_{ij}^{\mathrm{sig}}}{\rho_{ij}} & \text{if } \mathbf{v}_{ij}\cdot\mathbf{r}_{ij} < 0 \\ 0 & \text{otherwise} \end{cases} \tag{2.7}$$

where $w_{ij} = \mathbf{v}_{ij}\cdot\mathbf{r}_{ij}/|\mathbf{r}_{ij}|$ is the relative velocity projected onto the separation vector and α is typically in the range $\alpha \simeq$ 0.5-1.0. The signal velocity can be estimated as, in the simplest form, $v_{ij}^{\mathrm{sig}} = c_i + c_j - 3w_{ij}$, where c_i is the sound speed for particle i. In the equations of motion the artificial viscosity results in an excess pressure assigned to the fluid particles

$$P_{\mathrm{visc}} \simeq \frac{1}{2}\rho_{ij}^2\Pi_{ij} = \frac{\alpha}{2}\gamma\left(\frac{w_{ij}}{c_{ij}} + \frac{3}{2}\left(\frac{w_{ij}}{c_{ij}}\right)^2\right)P_{\mathrm{therm}} \tag{2.8}$$

where ρ_{ij} denotes the arithmetic mean of ρ_i and ρ_j and c_{ij} the mean sound speed. This viscous pressure depends not explicitly on the particle separation or smoothing length but on a Mach-number-like quantity w/c. It assumes though that the sound speeds and densities of the respective particles are roughly equal at the moment of computation. In order to reduce spurious angular momentum transport in the presence of shear flows an additional viscosity-limiter is used in GADGET2 and GADGET3 following Balsara (1995) and Steinmetz (1996). The viscous tensor is now multiplied by $(f_i + f_j)/2$ with

$$f_i = \frac{|\nabla \times \mathbf{v}|_i}{|\nabla \cdot \mathbf{v}|_i + |\nabla \times \mathbf{v}|_i} \tag{2.9}$$

a measure for the amount of shear in the fluid around particle i, based on standard estimates for divergence and curl in SPH (Monaghan 1992, Springel 2005).

Using the signal-velocity approach for the artificial viscosity leads to the use of a Courant-like hydrodynamical timestep

$$\triangle t_i^{(\mathrm{hyd})} = \frac{C_{\mathrm{Courant}}h_i}{\max_j(c_i + c_j - 3w_{ij})} \tag{2.10}$$

where the maximum is determined over all neighbouring particles j of particle i.

The version of GADGET that has been used here includes radiative cooling using tables for hydrogen and helium, assuming ionization equilibrium in the presence of the Haardt & Madau (2001) model for the $z = 0$ ultraviolet background radiation from quasars and galaxies. The cooling tables are generated using the publicly available package CLOUDY (version 06.02; Ferland 2000).

Schaye & Dalla Vecchia (2008) introduce an analytic conversion of the empirical Kennicutt-Schmidt law of star formation to a pressure law, which is subsequently implemented in the code. The observed Kennicutt-Schmidt law is (Kennicutt 1998)

$$\dot{\Sigma}_\star = (2.5 \pm 0.7) \times 10^{-4} M_\odot \mathrm{yr}^{-1}\mathrm{kpc}^{-2}\left(\frac{\Sigma_g}{1M_\odot \mathrm{pc}^{-2}}\right)^{(1.4\pm0.15)}, \tag{2.11}$$

and if corrected for using a Chabrier IMF instead of a Salpeter IMF

$$\dot{\Sigma}_\star = 1.5 \times 10^{-4} M_\odot \mathrm{yr}^{-1}\mathrm{kpc}^{-2}\left(\frac{\Sigma_g}{1M_\odot \mathrm{pc}^{-2}}\right)^{1.4}. \tag{2.12}$$

Assuming that the disk scaleheight is of the order of the local Jeans length for a self-gravitating disk and an effective equation of state for the multiphase interstellar matter that is polytropic when averaged over large scales ($P_{\rm tot} = P_{\rm tot,c}\left(\frac{\rho_{\rm g}}{\rho_{\rm g,c}}\right)^{\gamma_{\rm eff}}$ where $\gamma_{\rm eff}$ is the polytropic index) the empirical law for surface densities can be transformed to densities in the Schmidt law

$$\dot{\rho}_\star = A\left(1M_\odot{\rm pc}^{-2}\right)^{-n} \times \left(\frac{\gamma}{G} f_g P_c\right)^{(n-1)/2} \rho_{\rm g,c}\left(\frac{\rho_{\rm g}}{\rho_{\rm g,c}}\right)^{(n-1)\gamma_{\rm eff}/2+1} \tag{2.13}$$

with the Schmidt index $n = \frac{2(n_S-1)}{\gamma_{\rm eff}} + 1$ and n_S the index of the empirical Kennicutt-Schmidt law (here $n_S = 1.4$). In the above equation A is a numerical factor, f_g is the gas fraction in the galaxy and P_c is the pressure at the star formation threshold. Implementing this equation for star formation essentially means that gas with densities exceeding a threshold density for the onset of gravitational instability is expected to be multiphase and star forming and thus follows the effective equation of state with pressure $P \propto \rho_g^{\gamma_{\rm eff}}$. The gas then forms stars stochastically, meaning that the probability that a gas particle with star formation rate $\dot{\rho}_\star$ is converted into a star particle in a time-step Δt is $\min\left(\frac{\dot{m}_\star \Delta t}{m_g}, 1\right)$ with

$$\dot{m}_\star = 5.99 \times 10^{-10} M_\odot {\rm yr}^{-1}\left(\frac{m_g}{1M_\odot}\right)\left(\frac{f_g P_{\rm tot}/k}{10^3{\rm cm}^{-3}{\rm K}}\right)^{0.2} \tag{2.14}$$

where k is the Boltzmann constant, m_g is the gas mass of the particles for which $\dot{m}_\star$ is computed. In the equation the index $n_S = 1.4$ from the observed law has been implemented and $\gamma = 5/3$. Note that a star particle is to be interpreted as a simple stellar population.

Feedback from supernovae in Dalla Vecchia & Schaye (2008) is implemented in a way comparable to Springel & Hernquist (2003) with the modification that the winds are local and not decoupled hydrodynamically. The kinetic feedback is specified through two parameters, the wind mass loading parameter η, with the initial wind mass loading $\dot{M}_w$ in units of the star formation rate $\dot{M}_w = \eta \dot{M}_\star$, and the wind velocity v_w. Once a star particle reaches an age corresponding to the maximum lifetime of stars that end their lives as supernovae type II ($t_{SN} = 3 \times 10^7$ yr) a fraction $f_w = \frac{\eta v_w^2}{2\epsilon_{SN}}$ of the energy the supernovae of the star particle is converted to stochastically selected neighbouring gas particles, now called wind particles, which get the wind velocity v_w added to their velocity in a random direction. A wind particle is not allowed to be kicked again, is not allowed to convert into a star particle and remains a wind particle for a time $t_w = 1.5 \times 10^7$ yr. The values used for the above parameters are described in Section 2.3.

2.2 Initial conditions

2.2.1 Stars and dark matter

Initial conditions for the primary are build according to the algorithm by Springel, Di Matteo and Hernquist (2005). The dwarf galaxy consists of a dark matter halo, a stellar disk and a bulge. The halo has a Hernquist (Hernquist 1993) profile but the inner density profile is set to be equal to a NFW-profile with the same dark matter mass within r_{200} and a concentration of $c = 9$. Also the bulge is modelled with a Hernquist profile where the scalelength is a free parameter that is here set to 0.1 times the disk scalelength. The disk component is modelled with an exponential radial surface density profile and an isothermal sheet in the vertical direction

$$\rho_\star = \frac{M_\star}{4\pi z_0 h^2} {\rm sech}^2\left(\frac{z}{2z_0}\right)\exp\left(-\frac{R}{h}\right) \tag{2.15}$$

with the radially constant vertical scalelength $z_0 = 0.1h$, the disk scalelength. This disk scalelength is set assuming that the disk is centrifugally supported and that its thickness is negligible compared to its scalelength. The disk's angular momentum is $J_d = m_d J$ with $m_d = M_d/M_{\rm vir}$ the fraction of the total mass in the disk and J the angular momentum of the halo, where

$$J = \lambda G^{1/2} M_{200}^{3/2} r_{200}^{1/2} \left(\frac{2}{f_c}\right)^{1/2}, \tag{2.16}$$

and f_c depends only on the concentration of the halo and λ is the spin parameter, which in these simulations is set to $\lambda = 0.033$. The disk scalelength h is then found solving

$$J_d = M_d \int_0^\infty V_c(R) \left(\frac{R}{h}\right) \exp\left(-\frac{R}{h}\right) \mathrm{d}R, \tag{2.17}$$

with

$$V_c^2(R) = \frac{G\left[M_{\rm dm}(<R) + M_b(<R)\right]}{R} + \frac{2GM_d}{h}\frac{R}{2h}\left[I_0\left(\frac{R}{2h}\right)K_0\left(\frac{R}{2h}\right) - I_1\left(\frac{R}{2h}\right)K_1\left(\frac{R}{2h}\right)\right] \tag{2.18}$$

where the I_n and K_n are Bessel functions.

The velocity of both collissionless (stars and dark matter) components can be derived approximately once the density distribution is known. For the dark matter and bulge particles it is assumed that the velocity distribution only depends on the energy and the vertical component of the angular momentum. This results in $\langle v_R v_z\rangle = \langle v_z v_\phi\rangle = \langle v_R v_\phi\rangle = 0$ and $\langle v_R\rangle = \langle v_z\rangle = 0$. The velocity distribution can then be approximated as a triaxial Gaussian with axes aligned with R, ϕ and z. The velocity dispersions for R and z, σ_R^2 and σ_z^2 are now equal tot their second moments which can be obtained from the Jeans equation

$$\langle v_R^2\rangle_{\rm bulge/halo} = \langle v_z^2\rangle_{\rm bulge/halo} = \frac{1}{\rho}\int_z^\infty \rho(z', R)\frac{\partial\Phi}{\partial z'}\mathrm{d}z', \tag{2.19}$$

and

$$\langle v_\phi^2\rangle_{\rm bulge/halo} = \langle v_R^2\rangle + \frac{R}{\rho}\frac{\partial\left(\rho\langle v_R^2\rangle\right)}{\partial R} + v_c^2 \tag{2.20}$$

where, in both equations, ρ is the density of the component under consideration, Φ is the total gravitational potential and $v_c^2 = R\partial\Phi/\partial R$ is the circular velocity. If the first moment in the azimuthal direction , $\langle v_\phi\rangle$, does not vanish this implies a streaming motion in that direction. The bulge is set to have no net rotation so $\langle v_\phi\rangle_{\rm bulge} = 0$. For the dark halo it is set to a fixed fraction of the circular velocity $\langle v_\phi\rangle_{\rm halo} = f_s v_c$ where f_s depends only on the spin parameter, λ, and the concentration, c, of the halo (Springel & White 1999). Then the azimuthal velocity dispersion is equal to $\sigma_\phi^2 = \langle v_\phi^2\rangle - \langle v_\phi\rangle^2$.

For the disk also a triaxial Gaussian distribution is assumed for simplicity. In general the velocity structure of a disk can be much more complicated. Observations suggest that both the radial velocity dispersion and the vertical velocity dispersion in a galaxy are proportional to the surface density of the disk, and thus proportional to each other through the whole disk (Hernquist 1993; Kregel, van der Kruit & Freeman 2005; Kregel & van der Kruit 2005). Therefore we assume

$$\sigma_R^2 = \langle v_R^2\rangle = f_R\langle v_z^2\rangle = f_R\sigma_z^2 \tag{2.21}$$

with

$$\langle v_z^2 \rangle_{\rm disk} = \frac{1}{\rho_{\rm disk}} \int_z^{\infty} \rho_{\rm disk}(z', R) \frac{\partial \Phi}{\partial z'} {\rm d}z', \tag{2.22}$$

and the azimuthal second moment is also calculated in a way similar to the second moment for the halo and bulge

$$\langle v_\phi^2 \rangle_{\rm disk} = \langle v_R^2 \rangle_{\rm disk} + \frac{R}{\rho_{\rm disk}} \frac{\partial \left(\rho_{\rm disk} \langle v_R^2 \rangle_{\rm disk} \right)}{\partial R} + v_c^2. \tag{2.23}$$

The parameter that describes the ratio between the radial and the vertical velocity dispersion f_R is usually set to $f_R \sim 1$. In order to have stable disks however, we will set it to a different value for some of our simulations. To specify the mean streaming in the disk, the azimuthal velocity dispersion is related to the radial velocity dispersion through the epicycle approximation

$$\sigma_\phi^2 = \frac{\sigma_R^2}{\eta^2}, \tag{2.24}$$

where

$$\eta^2 = \frac{4\Omega^2}{\kappa^2} = \frac{4}{R} \frac{\partial \Phi}{\partial R} \left(\frac{3}{R} \frac{\partial \Phi}{\partial R} + \frac{\partial^2 \Phi}{\partial R^2} \right)^{-1}. \tag{2.25}$$

Finally the azimuthal mean streaming is

$$\langle v_\phi \rangle = \left(\langle v_\phi^2 \rangle - \frac{\sigma_R^2}{\eta^2} \right)^{1/2}. \tag{2.26}$$

This means that as the azimuthal streaming depends on σ_R, different values of f_R will also influence the azimuthal velocity dispersion and streaming through equations 2.22, 2.21 and 2.24.

In our experiments, and from galaxy to galaxy, the ratio of the vertical and radial velocity dispersions may change under influence of other changing parameters. If the Toomre stability parameter Q is required to be kept fixed from disk to disk, the radial velocity dispersion will depend on the surface density because $Q = \frac{\sigma_R \kappa}{3.36 G \Sigma}$ where κ is the epicyclic frequency, G the gravitational constant and Σ the surface density of the disk. The Toomre Q describes the stability of differentially rotating disks. If the value of this parameter is fixed then for an exponential disk σ_R is proportional to the mass of the disk if the radial disk scalelength is fixed as well. This dependency goes as

$$\frac{\sigma_R}{\sigma_R'} \propto \frac{M_d}{M_d'} \tag{2.27}$$

The vertical velocity dispersion on the other hand has a dependency

$$\frac{\sigma_z}{\sigma_z'} \propto \left(\frac{M_d}{M_d'} \right)^{1/2} \tag{2.28}$$

on the mass of the disk, see equation (2.22). In Chapters 3 and 4 we will present results for four different simulations with varying disk mass. In these simulations the value of the Toomre parameter (Q) has been kept fixed which means that the ratio between σ_z and σ_R, f_R, is changed for each individual galaxy following

$$f_R' = f_R \left(\frac{M_d}{M_d'} \right)^{1/2}. \tag{2.29}$$

Furthermore, the value of f_R is set such that the disk in isolation is generously stable ($Q \sim 2$) at least out to one scalelength. This results in a much larger radial velocity dispersion than the vertical dispersion whereas Springel, Di Matteo & Hernquist (2005) keep both velocity dispersions equal, $f_R = 1$. A more elaborate discussion of this choice can be found in Section 3.1.

2.2.2 Gas

For the dwarf galaxies with gas the initial conditions are built very similarly. The gas in the disk is a fixed fraction of the disk mass, $M_d = M_\star + M_{\rm gas}$, and also has an exponential surface density distribution. The vertical distribution of the gas particles however is determined by requiring hydrostatic equilibrium:

$$-\frac{1}{\rho_g}\frac{\partial P}{\partial z} - \frac{\partial \Phi}{\partial z} = 0, \tag{2.30}$$

where Φ (again) is the gravitational potential due to all components. The vertical distribution of the gas cannot be chosen freely as was done for the stellar component. The vertical scaleheight describes the temperature of the gas in a disk and this temperature is dependent on many physical processes within the gas. The equation of state is assumed to stay close to an effective equation of state (EOS) of the form $P = P(\rho)$. This means that initially the gas height for a given surface density is governed by the pressure due to self-gravity through this EOS. Later on the pressure, density and temperature will be influenced by many physical processes such as cooling and star formation. Here the equation of state is assumed to be effectively polytropic $P_{\rm tot} = P_{\rm tot,c}\left(\frac{\rho_g}{\rho_{g,c}}\right)^{\gamma_{\rm eff}}$ which means that the vertical distribution of the gas in the disk is governed by the two equations

$$\frac{\partial \rho_g}{\partial z} = -\frac{\rho_g^2}{\gamma_{\rm eff} P}\frac{\partial \Phi}{\partial z} \tag{2.31}$$

and

$$\Sigma_{\rm gas}(R,z) = \int \rho_g(R,z){\rm d}z. \tag{2.32}$$

The problem of determining the potential and the resulting gas distribution in a self-consistent way that arises through this approach is solved for both in an iterative way. The velocity field for the gas only consists of an azimuthal streaming velocity

$$v^2_{\phi,\rm gas} = R\left(\frac{\partial \Phi}{\partial R} + \frac{1}{\rho_g}\frac{\partial P}{\partial R}\right). \tag{2.33}$$

In the H2 and H4-simulations described in Chapter 3 and farther, the disk scalelength for the gas in the disk is set to a multiple of the stellar scalelength. In addition to setting a different disk scalelength for the gas, we have run test simulations with different values for the gas fraction, f_g, the star formation density threshold, $\rho_{\rm thresh}$, and the index for the effective equation of state, $\gamma_{\rm eff}$. A more thorough discussion on the reasons for these changes and the results can be found in Section 3.2.

2.2.3 Dark matter satellites

The initial conditions for the dark satellites were generated using a code provided by Alvaro Villalobos (see Villalobos & Helmi 2008). This code sets up a halo with a NFW mass density profile (Navarro, Frenk & White, 1996) given a value for the virial mass of the halo. A relation between concentration and virial mass of haloes is assumed so that effectively the NFW profiles are reduced to a single parameter family. This mass-concentration relation was updated in the code following Muñoz-Cuartas et. al. (2010) $c = 10^{2.099}{\rm M}_{\rm vir}^{-0.097}$ (their results are comparable with those of Macciò, Dutton & Van den Bosch 2008). The virial radius of the halo is defined as the radius at which the mean density is $\Delta_{\rm vir}(z)\rho_c(z)$ where $\rho_c(z)$ is the critical density of the universe and $\Delta_{\rm vir}(z)$ is the virial overdensity in the solution to the dissipational collapse of the spherical top-hat model: $M_{\rm vir}(z) = \frac{4\pi}{3}\Delta_{\rm vir}(z)\rho_c(z)R^3_{\rm vir}$.

Starting at this virial radius an exponential truncation is included since the mass of a NFW profile formally diverges with radius. The truncation decays on a scale $r_{\rm dec}$ (Springel & White 1999), with $r_{\rm dec}$ a free parameter, and exponent ϵ:

$$\rho(r) = \frac{\rho_s}{c(1+c)^2}\left(\frac{r}{R_{\rm vir}}\right)^{\epsilon} \exp\left(-\frac{r-R_{\rm vir}}{r_{\rm dec}}\right) \quad (r > R_{\rm vir}) \tag{2.34}$$

with the NFW mass density profile being

$$\rho_{\rm NFW}(r) = \frac{\rho_s}{(r/r_s)(1+r/r_s)^2}. \tag{2.35}$$

The exponent ϵ is set by requiring continuity between equations (2.35) and (2.34) and their logarithmic slopes. Then $\epsilon = -\frac{1-3c}{1+c} + \frac{R_{\rm vir}}{r_{\rm dec}}$. Depending on the value of $r_{\rm dec}$ the total mass of the halo will become larger than $M_{\rm vir}$, for $r_{\rm dec} = 0.1R_{\rm vir}$ this is $M_{\rm tot} \sim 1.1M_{\rm vir}$ so about 10 per cent larger. The velocity of each halo particle is computed from the distribution function associated to the mass density profile following Kazantzidis, Magorrian & Moore (2004). Finally the velocities are generated using the rejection method (Press et al. 1992).

The satellite is left to relax in isolation for 2 Gyr. The density profile is found to remain fairly stable and not to change significantly during that time as can be seen in Figure 2.2. Two satellites with different mass have been used, one with $M_{\rm vir} = 5.96 \times 10^8\ M_\odot\ \rm h^{-1}$ as found in the original Aquarius simulation, see Section 2, and one with $M_{\rm vir} = 2.0 \times 10^9\ M_\odot\ \rm h^{-1} = 0.2M_{\rm vir,\ main}$.

2.3 Numerical parameters

Evolving the dwarf galaxy and dark satellite in N-body/SPH simulations requires fixing a few parameters. For the N-body part the most important are the softening length and the number of particles. In all our simulations the softening length for the dark matter halo of the dwarf galaxy is $\epsilon_{\rm DM,host} = 0.034$ h^{-1} kpc while that for the dark matter satellite and all baryonic particles is $\epsilon_{\rm DM,sat} = \epsilon_{\rm baryon} = 0.02$ h^{-1} kpc. The dark matter halo of the dwarf galaxy is always represented by 492708 particles and the bulge has 34313 particles if present. In the simulations without gas (disk1, disk2 and disk3) the stellar disk has 68627 particles, in the simulations with gas the total number of particles for the disk is 98238 of which a fraction $f_{\rm gas} \times 98238$ is gas particles and $1 - f_{\rm gas} \times 98238$ is s star particle. The dark satellite with a mass of $5.96 \times 10^8\ M_\odot\ h^{-1}$ has 145485 particles and the satellite with a mass of $2.0 \times 10^9\ M_\odot\ h^{-1}$ has 490487 particles. The number of particles in each component, combined with the fraction of total mass in that component will give the mass per particle $m_{\rm baryon}$, $m_{\rm DM,host}$ and $m_{\rm DM,sat}$. To describe the structure of the dwarf galaxy we need to specify also the parameters giving the fraction of total mass in the disk and bulge, m_d and m_b, the gas fraction of the disk $f_{\rm gas}$, the scalelength of the bulge, $h_{\rm bulge}$, and the scaleheight, z_0, of the disk with respect to the disk scalelength h, the scalelength of the gas disk, $h_{\rm gas}$, with respect to the scalelength of the stellar disk h and the value describing the ratio between the radial and vertical velocity dispersion, f_R. Other fixed parameters involving the processes governed by SPH and subgrid models include the energy given to a supernova, ϵ_{SN}, its wind efficiency, η, and wind velocity, v_w, as described in Section 2.1.1, the star formation density threshold, $\rho_{\rm thresh}$, and the exponent for the multiphase equation of state $\gamma_{\rm eff}$. Finally, describing the orbit of the satellite with respect to the dwarf, is the inclination of the merger, i. Tables 2.2 and 2.3 show the parameters that are kept constant in all simulations. All varying parameters are summarized in table 2.4.

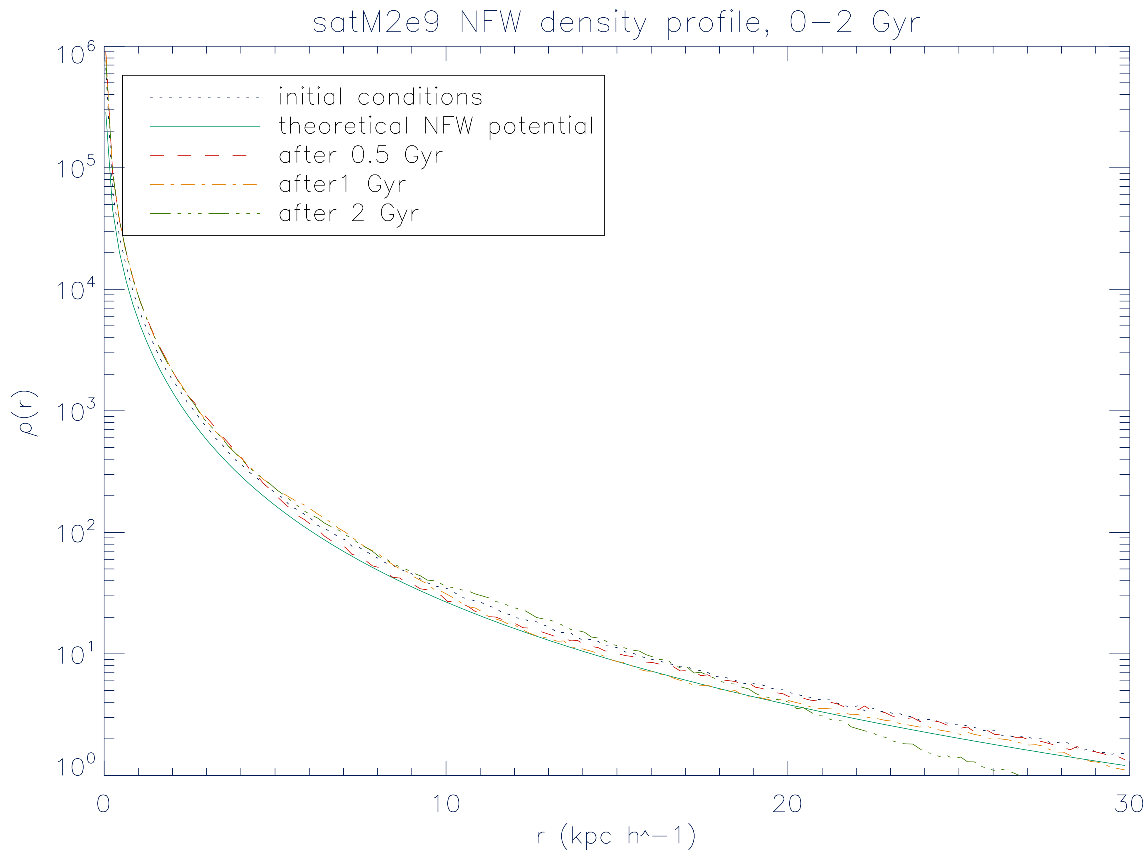

Figure 2.2: *Evolution of the density profile of the satellite with* $M_{vir} = 2.0 \times 10^9\ M_\odot\ h^{-1}$ *in isolation.*

Unchanging parameters:	$M_{\rm vir}$ ($M_\odot\ h^{-1}$)	z_0	$h_{\rm bulge}$	$\epsilon_{\rm baryon}$ (h^{-1} pc)	$\epsilon_{\rm DM,host}$ (h^{-1} pc)	$\epsilon_{\rm DM,sat}$ (h^{-1} pc)	$m_{\rm DM,sat}$ ($M_\odot\ h^{-1}$)
all simulations	1.0×10^{10}	$0.1h$	$0.1h$	20	34	20	4.1×10^3

Table 2.2: *Parameters governing the configuration and resolution of the dwarf galaxy and dark satellite that are fixed to these values for all simulations.*

Unchanging parameters:	η	v_w km s^{-1}	ϵ_{SN} erg $M_\odot^{-1}$
all simulations	2	600	1.8×10^{49}

Table 2.3: *Parameters governing the feedback by supernovae that are fixed to these values for all simulations, except for the simulations where the feedback is completely turned off.*

Changing parameters:	m_d	m_b	f_g	h (h^{-1} pc)	$h_{\rm gas}$ (h^{-1} pc)	$N_{\rm tot}$	$m_{\rm baryon}$ ($M_\odot$ h^{-1})	$m_{\rm DM,host}$ ($M_\odot$ h^{-1})	f_R	$\rho_{\rm thresh}$ n_H (cm^{-3})	$\gamma_{\rm eff}$	T$_c$ (°)	i ($M_\odot$ h^{-1})	$M_{\rm satellite}$
disk1 no merger	0.04	0	0	0.67	-	561335	5.86×10^3	1.96×10^4	9	-	-	-	-	-
disk2f9 no merger	0.02	0	0	0.67	-	561335	2.93×10^3	2.00×10^4	9	-	-	-	-	-
disk2f18 no merger	0.02	0	0	0.67	-	561335	2.93×10^3	2.00×10^4	18	-	-	-	-	-
disk3 no merger	0.008	0	0	0.67	-	561335	1.17×10^3	2.02×10^4	45	-	-	-	-	-
disk1 merger	0.04	0	0	0.67	-	1051822	5.86×10^3	1.96×10^4	9	-	-	-	30	2.0×10^9
disk2f9 merger	0.02	0	0	0.67	-	1051822	2.93×10^3	2.00×10^4	9	-	-	-	30	2.0×10^9
disk2f18 merger	0.02	0	0	0.67	-	1051822	2.93×10^3	2.00×10^4	18	-	-	-	30	2.0×10^9
disk3 merger	0.008	0	0	0.67	-	1051822	1.17×10^3	2.02×10^4	45	-	-	-	30	2.0×10^9
no merger	0.04	0.014	0.3	0.53	0.53	625059	4.1×10^3	1.9×10^4	1	0.1	4/3	10^5	-	-
frontal merger	0.04	0.014	0.3	0.53	0.53	770544	4.1×10^3	1.9×10^4	1	0.1	4/3	10^5	80	5.96×10^8
polar merger	0.04	0.014	0.3	0.53	0.53	770544	4.1×10^3	1.9×10^4	1	0.1	4/3	10^5	80	5.96×10^8
planar merger	0.04	0.014	0.3	0.53	0.53	770544	4.1×10^3	1.9×10^4	1	0.1	4/3	10^5	10	5.96×10^8
no merger no fb	0.04	0.014	0.3	0.53	0.53	625059	4.1×10^3	1.9×10^4	1	0.1	4/3	10^5	-	-
planar merger no fb	0.04	0.014	0.3	0.53	0.53	770544	4.1×10^3	1.9×10^4	1	0.1	4/3	10^5	10	5.96×10^8
H2	0.04	0.014	0.3	0.53	1.065	625059	4.1×10^3	1.9×10^4	1	0.1	4/3	10^5	-	-
H4 1	0.04	0.014	0.3	0.53	2.13	625059	4.1×10^3	1.9×10^4	1	0.1	4/3	10^5	-	-
H4 2	0.04	0.014	0.5	0.53	2.13	625059	4.1×10^3	1.9×10^4	1	0.1	4/3	10^5	-	-
H4 3	0.04	0.014	0.7	0.53	2.13	625059	4.1×10^3	1.9×10^4	1	0.1	4/3	10^5	-	-
H4 4	0.04	0.014	0.3	0.53	2.13	625059	4.1×10^3	1.9×10^4	1	0.1	1	10^5	-	-
H4 5	0.04	0.014	0.3	0.53	2.13	625059	4.1×10^3	1.9×10^4	1	0.1	1.4	10^5	-	-
H4 6	0.04	0.014	0.3	0.53	2.13	625059	4.1×10^3	1.9×10^4	1	10	4/3	10^5	-	-
H4 7	0.04	0.014	0.3	0.53	2.13	625059	4.1×10^3	1.9×10^4	1	200	4/3	10^5	-	-
H4 8	0.04	0.014	0.3	0.53	2.13	625059	4.1×10^3	1.9×10^4	1	10	1	10^5	-	-
H4 9	0.04	0.014	0.3	0.53	2.13	625059	4.1×10^3	1.9×10^4	1	10	1.4	10^5	-	-
H4 10	0.04	0.014	0.5	0.53	2.13	625059	4.1×10^3	1.9×10^4	1	200	4/3	10^5	-	-
H4 11	0.04	0.014	0.7	0.53	2.13	625059	4.1×10^3	1.9×10^4	1	200	4/3	10^5	-	-
H4 12	0.04	0.014	0.5	0.53	2.13	625059	4.1×10^3	1.9×10^4	1	10	4/3	10^5	-	-
H4 13	0.04	0.014	0.5	0.53	2.13	625059	4.1×10^3	1.9×10^4	1	10	1	10^5	-	-
H4 14	0.04	0.014	0.5	0.53	2.13	625059	4.1×10^3	1.9×10^4	1	10	1.4	10^5	-	-
H4 15	0.04	0.014	0.7	0.53	2.13	625059	4.1×10^3	1.9×10^4	1	10	4/3	10^5	-	-
H4 16	0.04	0.014	0.7	0.53	2.13	625059	4.1×10^3	1.9×10^4	1	10	1	10^5	-	-
H4 17	0.04	0.014	0.7	0.53	2.13	625059	4.1×10^3	1.9×10^4	1	10	1.4	10^5	-	-
H4 1 T$_c = 10^4$	0.04	0.014	0.3	0.53	2.13	625059	4.1×10^3	1.9×10^4	1	0.1	4/3	10^4	-	-
30 merger H4 12	0.04	0.014	0.5	0.53	2.13	1115546	4.1×10^3	1.9×10^4	1	10	1.4	10^5	30	2.0×10^9
planar merger H4 12	0.04	0.014	0.5	0.53	2.13	1115546	4.1×10^3	1.9×10^4	1	10	1.4	10^5	10	2.0×10^9
polar merger H4 12	0.04	0.014	0.5	0.53	2.13	1115546	4.1×10^3	1.9×10^4	1	10	1.4	10^5	80	2.0×10^9
frontal merger H4 12	0.04	0.014	0.5	0.53	2.13	1115546	4.1×10^3	1.9×10^4	1	10	1.4	10^5	80	2.0×10^9
planar merger H4 1	0.04	0.014	0.3	0.53	2.13	1115546	4.1×10^3	1.9×10^4	1	0.1	4/3	10^5	10	2.0×10^9

Table 2.4: *All simulations listed with the parameters for which the values vary for different simulations.*

Chapter 3

Objects in isolation

To make sure changes in the morphology and kinematics of the dark matter satellite in our merger simulations are not due to instabilities in its initial configuration, this is relaxed for 2 Gyr in isolation before placed in a simulation with external influences, i.e. a host galaxy. We also perform simulations of the dwarf galaxy in isolation to make sure it is in equilibrium initially, as well as to separate clearly the effect induced by the dark satellite from internal processes. Our isolated dwarf simulations also allow us to understand the effect of changing the various parameters on the local star formation rates and morphological properties of isolated systems. Moreover, in order to investigate the effect of a merger with a dark satellite on a dwarf galaxy it is best if the simulated isolated dwarf is stable in its configuration and star formation rate. These should be representative of real dwarf galaxies.

3.1 Dwarf galaxies without gas

As described in Section 2.2, the ratio between the radial and vertical velocity dispersion is related to the stability of the disk. As we aim to study the heating induced by a merger on the disk of the dwarf galaxy, it is important that this disk initially is stable. In Figure 3.1 we plot the variation with radius R of the Toomre stability parameter Q and the velocity dispersions for four different values of $f = \sigma_R^2/\sigma_z^2$. In this figure it can be seen that σ_z remains the same while σ_R and Q change with varying f. σ_ϕ is defined as a function of σ_R, and so should change with varying f as σ_R depends on f. In order to obtain reasonable radial velocity dispersions (i.e. not very large) while also making sure that almost the whole disk is quite stable we set $f = \sigma_R^2/\sigma_z^2 = 9$ for the experiment denoted as disk1.

In the case of experiments disk2 and disk3 we have changed the mass of the disk to the following: $M_{\mathrm{d,\,disk2}} = 0.5 M_{\mathrm{d,\,disk1}}$ and $M_{\mathrm{d,\,disk3}} = 0.2 M_{\mathrm{d,\,disk1}}$. Recall that the radial and vertical velocity dispersion vary in a different way with the mass of the disk (see Section 2.2.1). This implies that if the Toomre stability parameter of the disk is kept constant, then the value of the ratio $f = \sigma_R^2/\sigma_z^2$ will change as well. For disk2 we should have $f_2 = 2f_1 = 18$ and for disk3 the ratio should be $f_3 = 5f_1 = 45$. These values are used for the simulations denoted as disk2f18 and disk3. In order to see how big the effect of the initial stability of the disk is on the heating by the merger, we have performed also a simulation for disk2 with $f_2 = 9 = f_1$. The initial variation of Q, σ_R, σ_z and $/\sigma_\phi$ with R can be found in Figure 3.2. As the thickness of the disks does vary significantly while the disk is relaxing the disks are first run in isolation before the satellite is placed in the simulation. Figure 3.3 shows the values for the Toomre stability parameter, Q, and the velocity dispersions after letting the disk galaxies relax and stabilize in isolation. There can be seen that all disks evolve into a more stable configuration and that the smallest disk has stabilized more in its outskirts than the other disks. This could well be related to that disk being much less massive and therefore also becoming radially

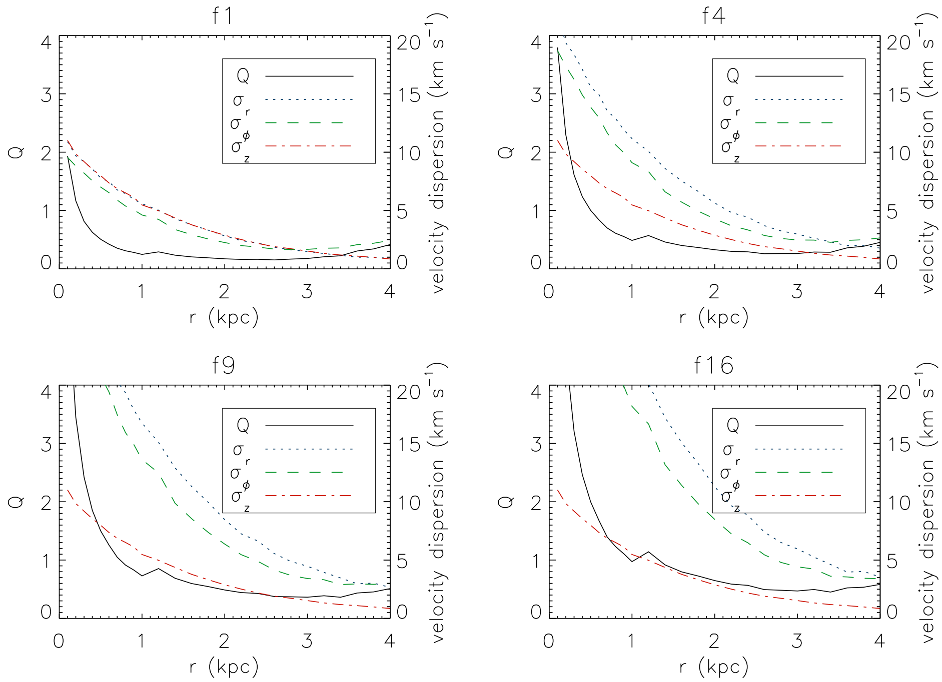

Figure 3.1: *Q, σ_R, σ_ϕ and σ_z with changing value for $f = \sigma_R^2/\sigma_z^2$. From left to right, top to bottom: $f = 1$, 4, 9 and* 16

less extended than the other disks while stabilizing. In the inner parts the disks with an equal fixed value for Q, disk1, disk2f18 and disk3, do still have very similar values for Q with radius. The one disk with a different value for Q, disk2f9, is seen to be less stable than disk2f18 over the whole range in radius. When run in isolation the disks also change their vertical density profile. The less massive disks already become slightly thicker than the more massive disks. Figure 3.4 shows this evolution in vertical surface density for the most and the least massive disks, disk1 and disk3. Disk3 needs longer to relax to a stable vertical distribution and that stable distribution is thicker than the vertical profile for disk1. Disk3 might need more time to reach equilibrium because it is initially colder in σ_z while it has the same vertical scale as disk1. Figure 3.3 shows that for disk3 both σ_z and σ_ϕ change significantly compared to changes in these parameters for the other three disks.

3.2 Dwarf galaxies including gas

The dwarf galaxy simulations with gas in the disk were initially set up in the same way as the dwarf case ($M_{\rm vir} = 10^{10} M_\odot$) presented by Dalla Vecchia & Schaye 2008. When this isolated galaxy is run over a timescale of 2 Gyr (comparable to the expected duration of the mergers to be simulated) it shows an initial peak in the star formation rate with a steep decline which appears to be somewhat artificial and a very low, slowly declining star formation rate after this (see Figure 3.5). Literature studies of dwarfs (both observational and theoretical) show that these generally have a low but on average almost constant star formation rate and individually often depict a bursty behaviour (Okamoto et al. 2010; Stinson et al. 2007; Immeli et al 2004; Sawala et al. 2010, 2011; Hunter et al. 1998; Pelupessy et al. 2008; Weisz et al. 2011). Figure 3.5 shows that a simulation without the inclusion of feedback (from supernovae winds) does not have the steep decline after the initial peak but only a slow continuous decline. This could suggest that either the feedback was too strong

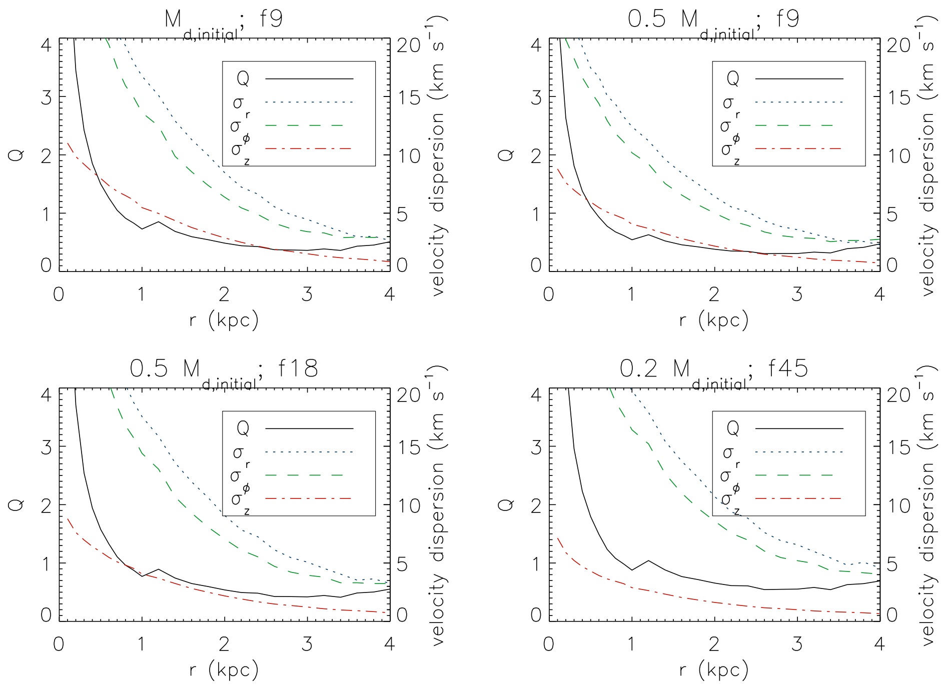

Figure 3.2: *Q, σ_R, σ_ϕ and σ_z with changing disk mass and so changing value for $f = \sigma_R^2/\sigma_z^2$ if Q is kept constant. From left to right and from top to bottom: $M_d = M_{d,\ initial}$ and $f = 9$, $M_d = 0.5M_{d,\ initial}$ but still $f = 9$ (so Q does change!), $M_d = 0.5M_{d,\ initial}$ and $f = 18$ and $M_d = 0.2M_{d,\ initial}$ and $f = 45$*

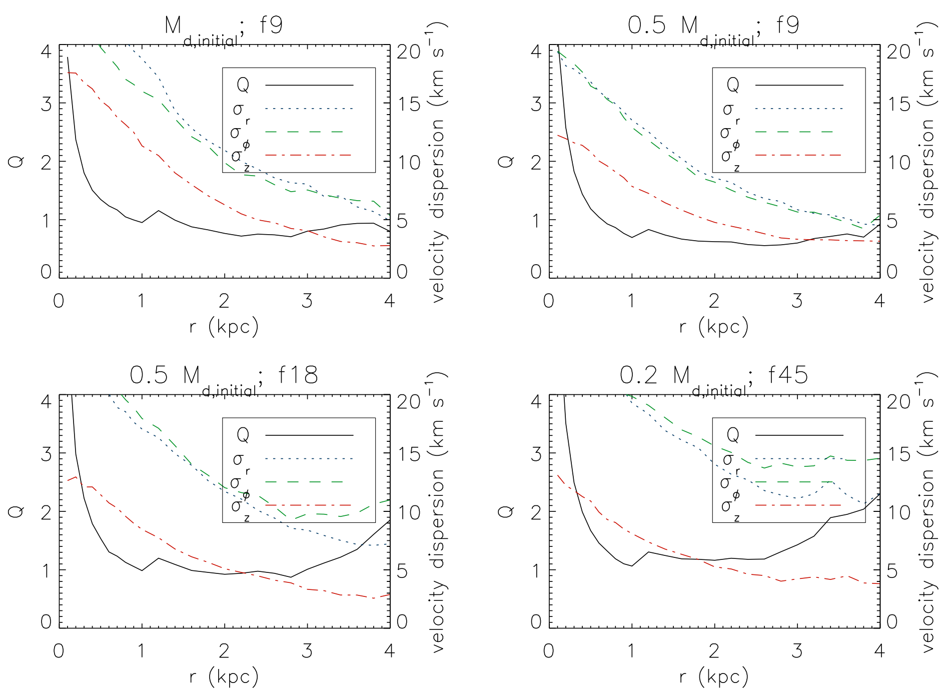

Figure 3.3: *The same as Figure 3.2 but after being run in isolation (without a merger) for 6 Gyr.*

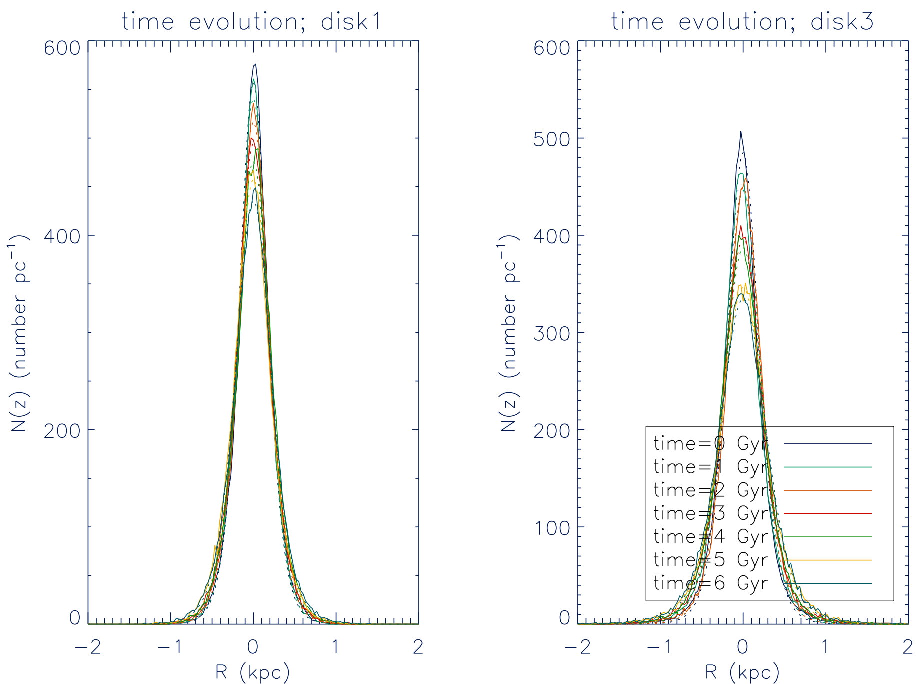

Figure 3.4: *Change of the vertical surface density profile of disk1 and disk3 without a merger while it is relaxed in isolation for 6 Gyr.*

in the original model and blew out the gas, or initially so many star particles were formed that due to their feedback again most of the gas was blown out. Figure 3.6 shows how the gas content in the inner regions (within 0.5 kpc and within 3 kpc) decreases with time. Especially in the most central region, (within 0.5 kpc, see Figure 3.6a) the gas content is lost after the initial peak in star formation for the simulations including supernova feedback although at larger radii, gas is still present in this case. Considering that also the initial central gas surface density is quite high (above 100 $M_\odot$ pc^{-2} as can be seen in Figure 3.7b), the gas is probably lost due to the high initial star formation.

Generally observational studies show that the gas extends farther out than the stellar disk. In our initial simulations the exponential gas disk had the same scalelength as the stellar disk, which led to the central surface density of the gas to be much higher than observed for dwarf galaxies (Walter & Brinks 2001; Hunter, Elmegreen & Baker, 1998; Swaters et al. 2002; van der Kruit & Freeman 2011). Van der Kruit & Freeman (2011) review that the HI surface density averaged over the whole HI disk seems to be constant from galaxy to galaxy with a well-defined maximum surface density for disk galaxies, of approximately 10 $M_\odot$ pc^{-2}. We should note that the star formation threshold for the gas density in simulations is usually close to this value when translated into surface density. This led us to revisit our initial conditions.

Extending the gas disk farther out than the stellar disk and so building a disk gas surface density which is closer to observed disk surface densities has a direct effect on the star formation rate. Figure 3.8 shows that the initial peak that was present for the disks with $h_{\rm gas} = h_{\rm stars}$ is much reduced. However the star formation rate over the whole time period of 4 Gyr is rather low ($\sim 0.001 M_\odot$ year^{-1} for most of the time) and the initial peak is still present. This urges us to look at the parameters influencing the star formation in a more general way.

There are a number of numerical parameters that can influence the star formation as it is implemented in the simulation code. One parameter is of course the index for the Kennicutt-Schmidt law (see Section 2.1) which we will leave as it is. However, we will re-examine and explore changes in

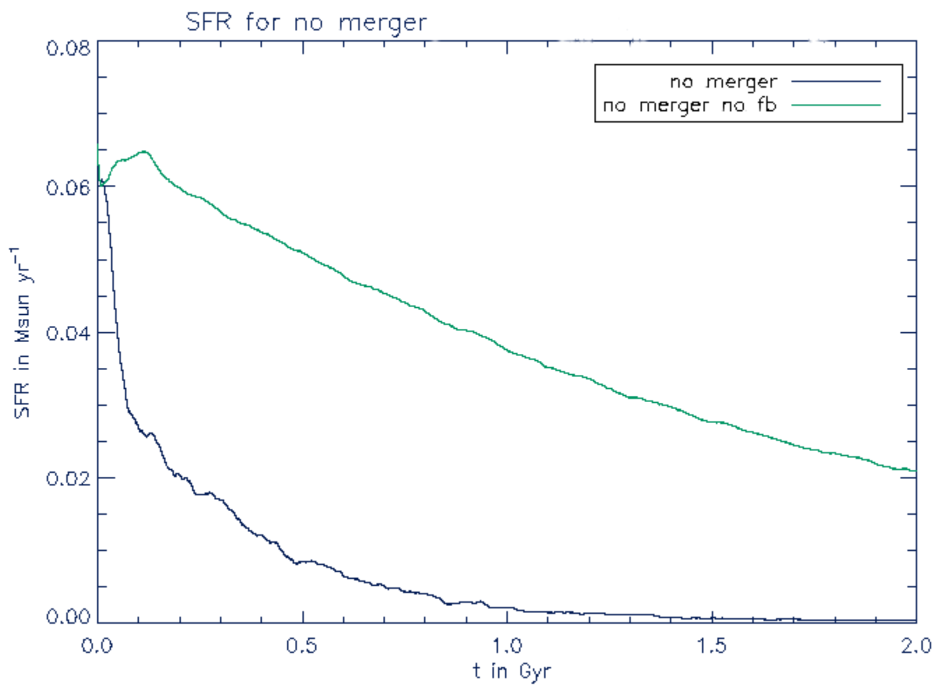

Figure 3.5: *Star formation rate for the initial settings of the dwarf with gas, in isolation and with and without feedback.*

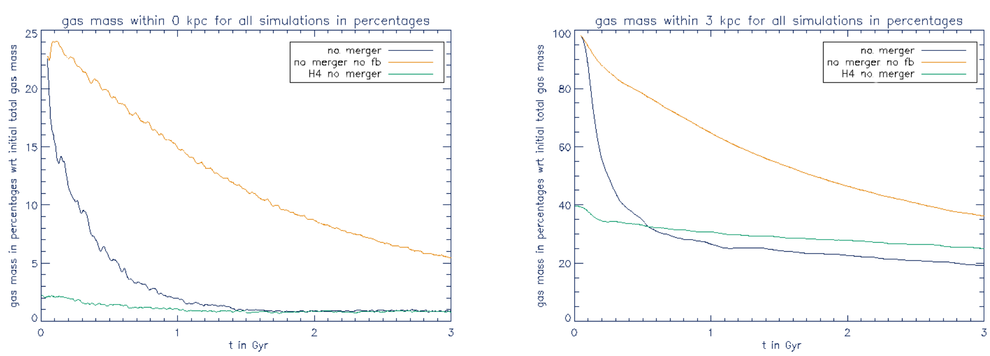

(a) *Gas mass within the inner 0.5 kpc* **(b)** *Gas mass within the inner 3 kpc*

Figure 3.6: *Gas mass in the inner regions with time for simulations with and without supernova feedback.*

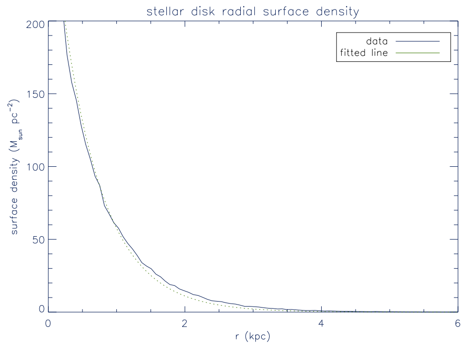

(a) *Stellar disk surface density.*

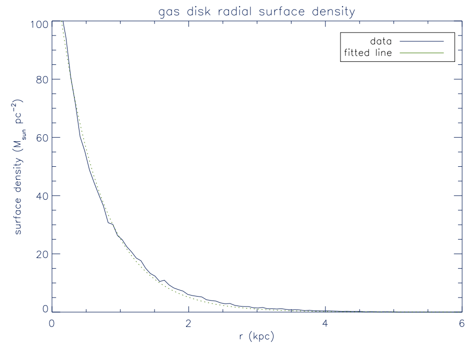

(b) *Gas disk surface density with a disk scalelength equal to the stellar disk scalelength $h_{gas} = h$.*

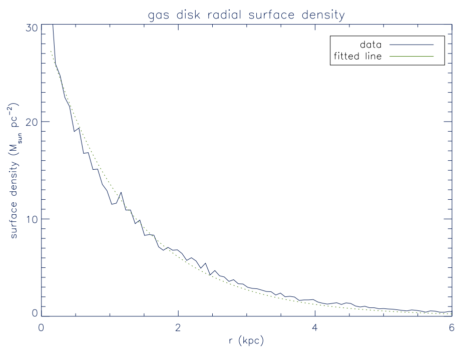

(c) *Gas disk surface density with a disk scalelength twice the stellar disk scalelength $h_{gas} = 2h$.*

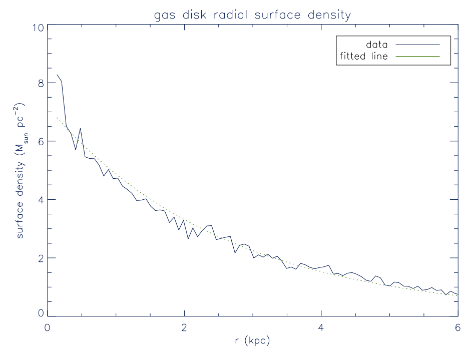

(d) *Gas disk surface density with a disk scalelength four times the stellar disk scalelength $h_{gas} = 4h$.*

Figure 3.7: *Initial surface densities for stars and gas for different scalelengths for the gas disk.*

the index for the polytropic equation of state, γ_{eff}, the initial fraction of gas in the disk, f_g, and the density threshold for star formation, ρ_{thresh}.

The polytropic equation of state that we use introduces a minimum pressure explicitely that guarantees that the available resolution is sufficient for resolving the Jeans mass (Parry et al. 2011). Failure to resolve the Jeans mass or Jeans length is known to lead to artificial fragmentation as particles then can have masses greater than the local Jeans mass (Bate & Burkert 1997). For a polytropic equation of state, $P_{\text{tot}} \propto \rho_g^{\text{eff}}$, the Jeans mass and length scale as

$$M_J \propto f_g^{3/2} \rho_g^{(3\gamma_{\text{eff}}-4)/2} \tag{3.1}$$

$$L_J \propto f_g^{1/2} \rho_g^{(\gamma_{\text{eff}}-2)/2}. \tag{3.2}$$

The initial value for $\gamma_{\text{eff}} = 4/3$ now gives a Jeans mass independent of the gas density. For a smaller value of γ_{eff} the Jeans mass decreases with increasing gas density which ensures collapse but might lead to spurious fragmentation. For a larger value, $\gamma_{\text{eff}} > 4/3$ collapse is expected, while the Jeans length decreases with increasing gas density ($\gamma_{\text{eff}} < 2$). We thus choose to explore this parameter by performing simulations with $\gamma_{\text{eff}} = 1$ and $\gamma_{\text{eff}} = 1.4$.

The initial gas fraction in the disk, f_g, determines the gas reservoir that can be used for star formation. The Jeans mass and length and the Kennicutt-Schmidt law are also weakly dependent on f_g. In general irregular (disky) dwarf galaxies appear to have a higher gas fraction than larger spirals or irregulars (with the exception of those that have become satellites and so are stripped of their gas). Therefore we explore different values of f_g, namely $f_g = 0.5$ and $f_g = 0.7$ instead of $f_g = 0.3$.

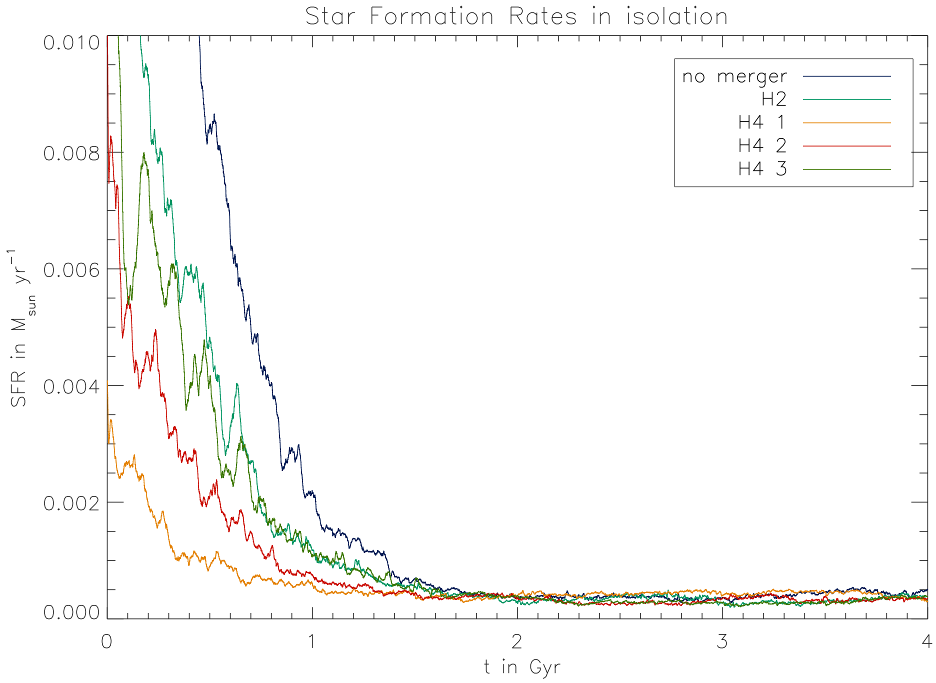

Figure 3.8: *Star formation rate for a dwarf galaxy with gas, where the gas disk has a different scalelength than the stellar disk: $h_{gas} = h_{stars}$ (the original dwarf) in isolation, $h_{gas} = 2h_{stars}$ in isolation, $h_{gas} = 4h_{stars}$ in isolation and $h_{gas} = 4h_{stars}$ with a merger.*

The star formation threshold density is in numerical simulations one of the key parameters governing star formation. Theoretically the initial value of $n_H = 0.1$ cm^{-3} corresponds to a surface density of $\Sigma_{\rm thresh} = 7.3 M_\odot$ pc^{-2} (Schaye 2004). This is close to the empirically found value of $\Sigma_{\rm thresh} \sim 10 M_\odot$ pc^{-2} and also falls in the range of theoretically predicted values for a star formation threshold due to the thermogravitational instability that is triggered on the transition from the warm gas phase to the cold gas phase $\Sigma_{\rm thresh} \approx$3-10 $M_\odot$ pc^{-2} (Schaye & Dalla Vecchia 2008; Schaye 2004). However, numerically the threshold density is also related to the resolution. Better resolution will increase the maximum density that is resolved. Parry et al. 2011 state that for an irradiated primordial gas with an isothermal density profile, as they set in the Aq-C-4, Aq-C-5 and Aq-C-6 simulations, the maximum density that is resolved is increased by a factor of four if the gravitational softening is decreased by a factor two. Moreover, House et al. 2011 argue that generally a too low star formation threshold is used in numerical simulations which creates a 'dispersion floor' as the gas does not cool enough before stars are formed. Governato et al. 2010 succesfully simulated the first bulgeless disk galaxy using a star formation density threshold of 100 cm^{-3} with a spatial resolution of about $\sim$ 100 pc. We therefore explore two higher values for the star formation density threshold, namely 10 cm^{-3} and 200 cm^{-3}. These values are based on the relations between numerical parameters found for the Aq-C simulation by Parry et al. Extrapolating their findings for the Aquarius-C simulations to our simulation, our much smaller gravitational softening and much larger number of particles indicate that a threshold density of 10-200 cm^{-3} should be used. Governato et al. do have similar resolution and softening length and choose their density threshold for star formation to be 100 cm^{-3} based on Tasker & Bryan (2008) and Saitoh et al. (2008). Tasker & Bryan however show that the multiphase ISM is strongly affected by the processes involved with star formation but that its exact structure does not have to be modelled in detail to obtain the correct general star formation properties for disk galaxies. On the other hand, having a higher density threshold with a higher star formation efficiency does affect the locations and burstiness of star formation and thus the complexity of the disk in their simulations. Saitoh et al. argue that this is an important reason to aim for higher resolution simulations which can employ high density thresholds for star formation. Moreover they claim that a higher density threshold not only reproduces the complexity of the ISM, star forming regions and the eventual stellar disk much better, but is also more insensitive to free parameters in the star formation model and reproduces the empirical laws more naturally.

We have explored different values for the parameters γ_{eff}, f_g and ρ_{thresh}. All simulations that have been performed are listed in table 2.4. Values for configuration and wind parameters which are kept constant for all simulations are summarized in tables 2.2 and table 2.3 respectively. The results for the star formation rate of the isolated dwarf galaxy are shown in Figures 3.9, 3.10 and 3.11. In these figures one of the three changing parameters is kept constant while the other is allowed to vary. In Figure 3.9 the gas fraction f_g is kept fixed at the old value, $f_g = 0.3$, in Figure 3.10 the value for γ_{eff} is fixed at the value $\gamma_{\mathrm{eff}} = 4/3$ and in Figure 3.11 the density threshold ρ_{thresh} is fixed on the new value $\rho_{\mathrm{thresh}} = 10\ \mathrm{cm}^{-3}$. In general it can be seen that increasing the density threshold has the effect that the star formation is delayed. The gas, presumably, needs more time to reach the required density to form new stars. Changing the gas fraction itself increases the star formation rate slightly, but mostly in the beginning of the simulation. The star formation rates after 4 Gyr are very comparable for $f_g = 0.3$ and $f_g = 0.7$. Finally, changing the parameter governing the effective equation of state does not seem to have a strong structural effect.

Figure 3.12 shows the gas mass with respect to the initial gas mass for the simulations in question. This figure clearly shows that none of the galaxies forms stars very efficiently, that a large fraction of the gas remains present but is not dense enough to form stars, and that there is little difference to be found from simulation to simulation. Figures 3.13 to 3.16 show the star formation rate with respect to the local surface density of the gas. These figures show that the star formation approximately does follow the Kennicutt law (dashed line) for all cases. The lower plot shows the star formation rate and surface density computed in cilindrical rings centered on the center of the disk with each ring having the same area. The upper plot shows the star formation rate and surface density around star forming gas particles in the simulation. The area considered around the individual particle is the same as the area for the cilindrical bins, 0.1 kpc^2. Generally one can see that while the star formation in the center averaged over cilidrical bins generally lies on or slightly above the Kennicutt law but below the density threshold, the average around star forming particles lies above the density threshold but can lie below the Kennicutt law. This shows that local star forming regions lie in denser environments (the local surface density average is higher than the average over the whole cilindrical ring at that radius from the center) but that the star forming clouds itself are very local peaks so that the star formation rate is not as high as the average density would predict following the Kennicutt law. These figures show that as the density threshold for star formation is increased there is be less star formation but the star formation that is present is much more efficient so that globally the star formation rates are comparable. For a density threshold of $\rho_{\mathrm{thresh}} = 200\ \mathrm{cm}^{-3}$ there are but very few locations of star formation but the local density in these star forming clumps is so high compared to its surroundings that the density averaged over 0.1 kpc^2 lies below the Kennicutt law.

Figures 3.17 to 3.20 show scatter plots of the temperature and density of gas particles at three different times in the simulations. These figures support the view that the gas behaves very similarly in all the simulations performed, and that there is less gas above the threshold if the density threshold in increased. In all these figures most of the gas is located in the third quadrant, so the gas is cold and in diffuse form.

Finally Figure 3.21 shows the percentage of gas particles that satisfy the star formation criteria: the percentage of gas particles having a density that is above the density threshold and the percentage of gas particles having a temperature that is below the threshold temperature. This plot emphasizes that the density threshold is in general the stricter criterium: almost all of the gas is below the temperature threshold for all simulations but only a small fraction of the gas particles is above the density threshold. The value of the temperature threshold does however have an indirect effect on the star formation rate. One test simulation has been performed changing the temperature threshold from 10^5 K to 10^4 K. The effect can be seen as the dotted green line in Figure 3.21: initially less gas is below the temperature threshold, therefore the gas cools further and gets more dense, so a larger fraction of the gas is above the density threshold. This effect wears out quickly however as the gas stabilizes in the new situation. After that the fraction of gas below the temperature threshold or above the density threshold is comparable to the other, $T_c = 10^5$ K, simulations. The evolution of the total gas mass in the isolated dwarf galaxy for the $T_c = 10^4$ K simulation can be found in Figure 3.12. There also can be seen that in the first Gyr the gas is consumed faster than for the other simulations so the star formation rate is higher as there is more gas above the star formation density threshold. However, in the second Gyr the gas consumption slows down so that the star formation rate after 2 Gyr is probably comparable to that of the $T_c = 10^5$ K simulations.

One clear observation can be made regarding all these star formation rate histories. Despite significant variations in the numerical parameters governing star formation, they all still are in the same range; there are individual differences at different points in time but averaged over the whole 4 Gyr they are very similar. This means that none of the explored parameters has a strong impact on the star formation rates for these models. In order to change the star formation rates to values more comparable with those found in other simulations for galaxies of approximately the dynamical mass cosidered here ($\sim 0.01 M_{\odot}\mathrm{yr}^{-1}$), we have to look for other parameters globally governing the star formation process. This is beyond the scope of this thesis but we will discuss some options here.

The rate at which gas particles form stars in the used model is implemented based on a analytic approach to convert the observed two-dimensional surface density criterion (associated to the Kennicutt law) into a three-dimensional volume density based Schmidt law in a physical way. The rate of star formation thus effectively depends strongly on the Kennicutt law that is assumed. The Kennicutt law that has been used so far is that found by Kennicutt (1998) by measuring global star formation rates and surface densities for spiral galaxies and starburst galaxies. A similar law just taking the global star properties of the spirals, however, already has a significantly different slope. This slope converges closer towards the slope of the general Kennicutt law when the SFR and surface density is measured more locally in these spirals (Kennicutt 1998). But other studies also have found indications that the Kennicutt law might have a steeper slope in the outskirts of spirals and in dwarf galaxies (Roychowdhury et al. 2009; Bigiel et al. 2008; Bigiel et al. 2010). This could in fact have a major influence on the star formation rates in our simulated isolated dwarfs since it gives a steeper dependence on the gas, and hence a higher star formation rate for a given gas mass above the threshold density.

Other parameters that could be explored more thoroughly are those associated to the modelling of feedback, i.e. in our case the wind parameters. The wind parameters used were optimized for larger galaxies, where the resolution is generally somewhat poorer. The winds in our simulations therefore, could well be overly efficient. Figure 3.5 shows that shutting of the supernovae winds completely does result in a higher star formation rate for a longer time. In this case the star formation rate does drop but that could well be because the star formation is so high that the gas present is consumed and therefore starts to form stars less fast. Exploring slower and less efficient winds in combination with different gas fractions and star formation thresholds could give us a better view or insights into how to model the physical conditions present in dwarf galaxies.

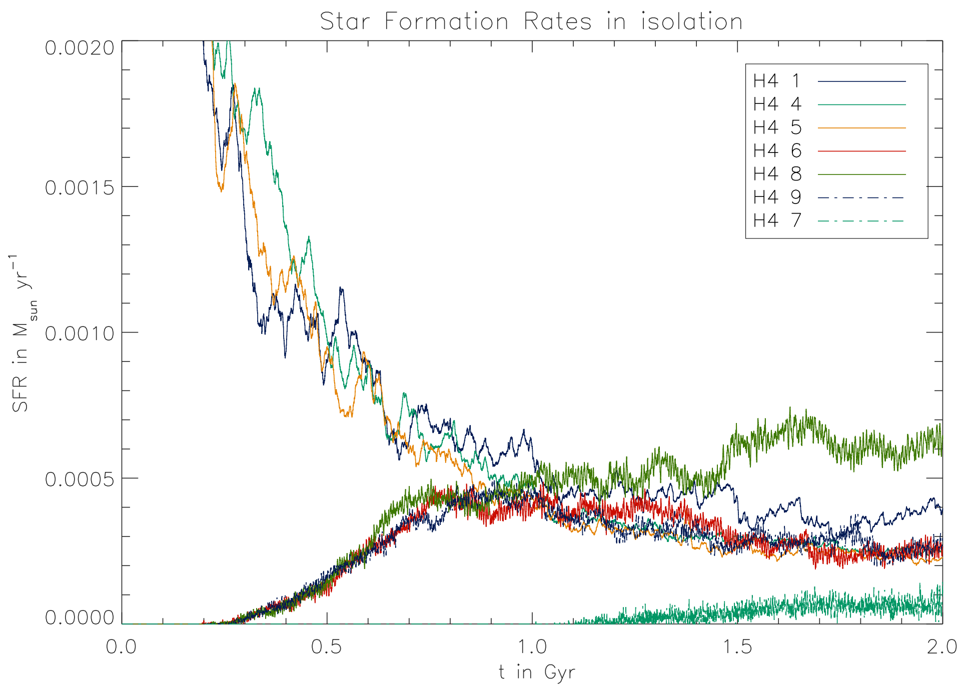

Figure 3.9: *Star formation rate for a dwarf galaxy with gas, where* $h_{gas} = 4h_{stars}$*,* $\gamma_{eff} = 1,\ 4/3,\ 1.4$*,* $f_g = 0.3$ *and* $\rho_{thresh} = 0.1$*, 10 and 200* cm^{-3}.

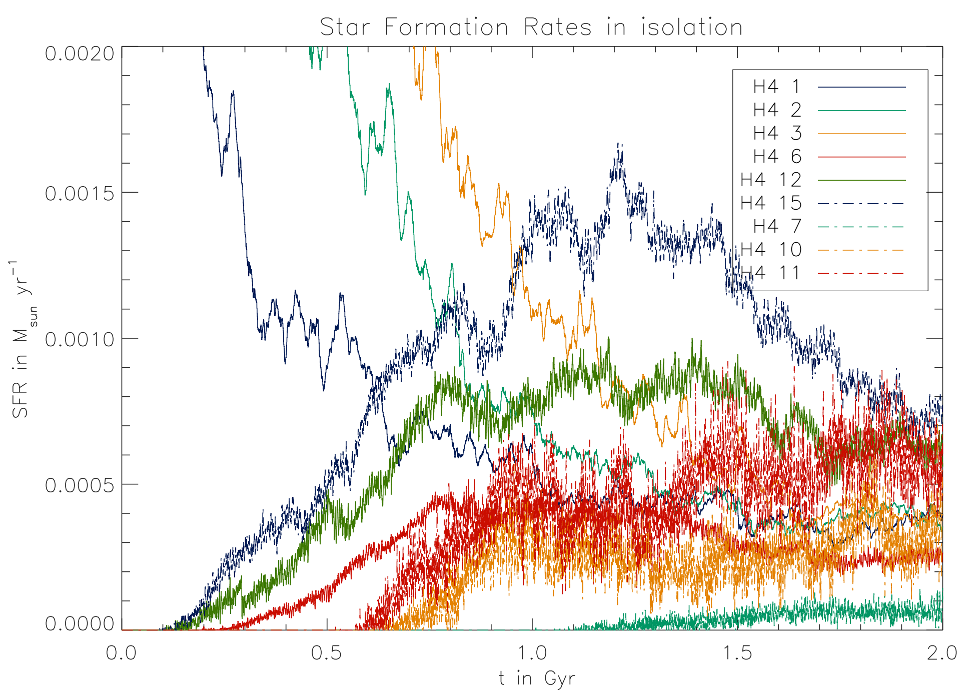

Figure 3.10: *Star formation rate for a dwarf galaxy with gas, where* $h_{gas} = 4h_{stars}$*,* $\gamma_{eff} = 4/3$*,* $f_g = 0.3$*, 0.5, 0.7 and* $\rho_{thresh} = 0.1$*, 10, and 200* cm^{-3}.

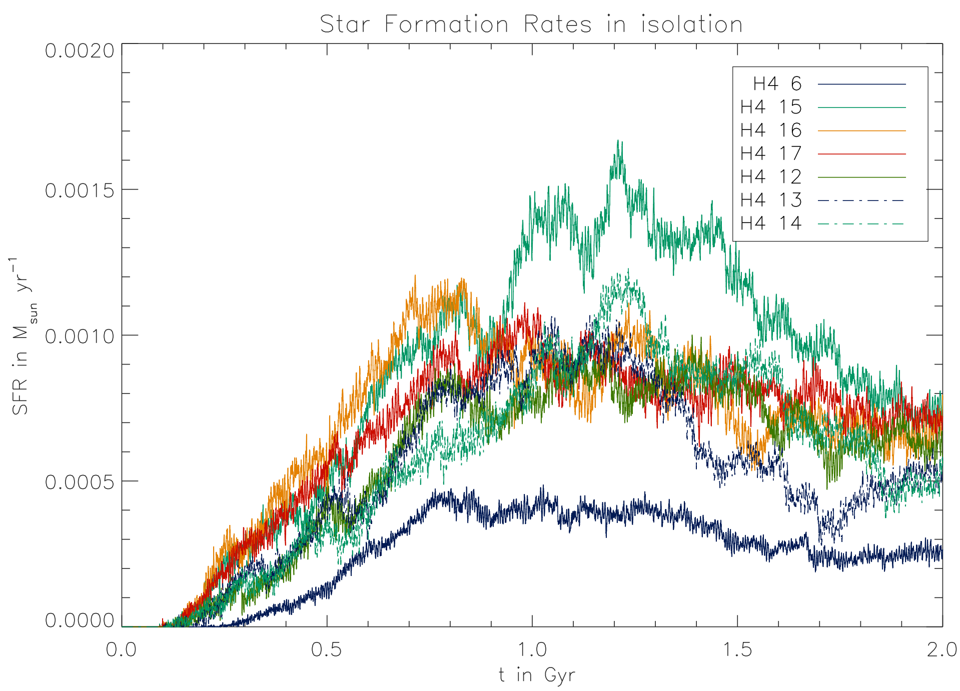

Figure 3.11: *Star formation rate for a dwarf galaxy with gas, where* $h_{gas} = 4h_{stars}$, $\gamma_{eff} = 1$, 4/3, 1.4, $f_g = 0.3$, *0.5, 0.7 and* $\rho_{thresh} = 10\ cm^{-3}$.

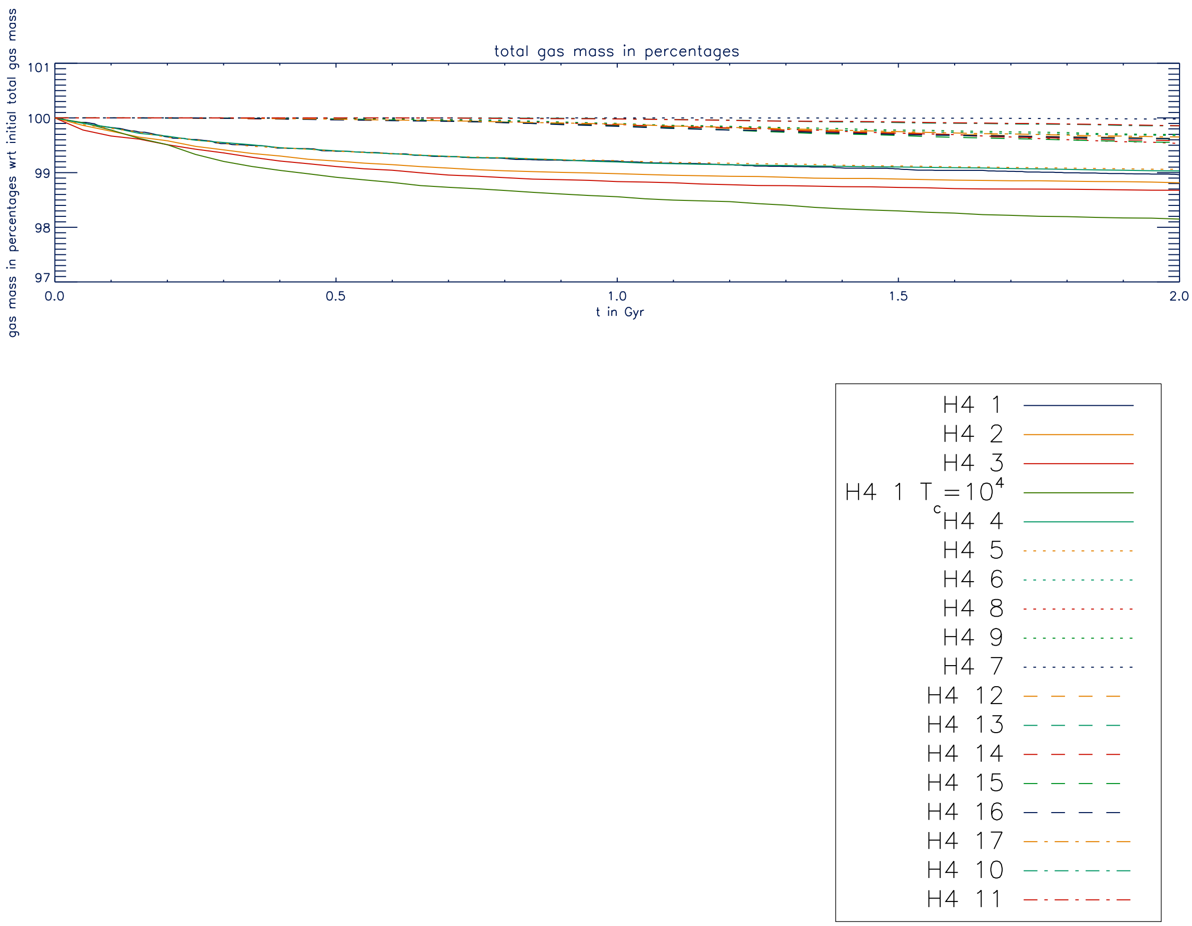

Figure 3.12: *Mass in gas in percentages of the initial mass in gas, where* $h_{gas} = 4h_{stars}$, $\gamma_{eff} = 1,\ 4/3,\ 1.4,$ $f_g = 0.3$, *0.5, 0.7 and* $\rho_{thresh} = 0, 1,\ 10$ *and* $200\ cm^{-3}$.

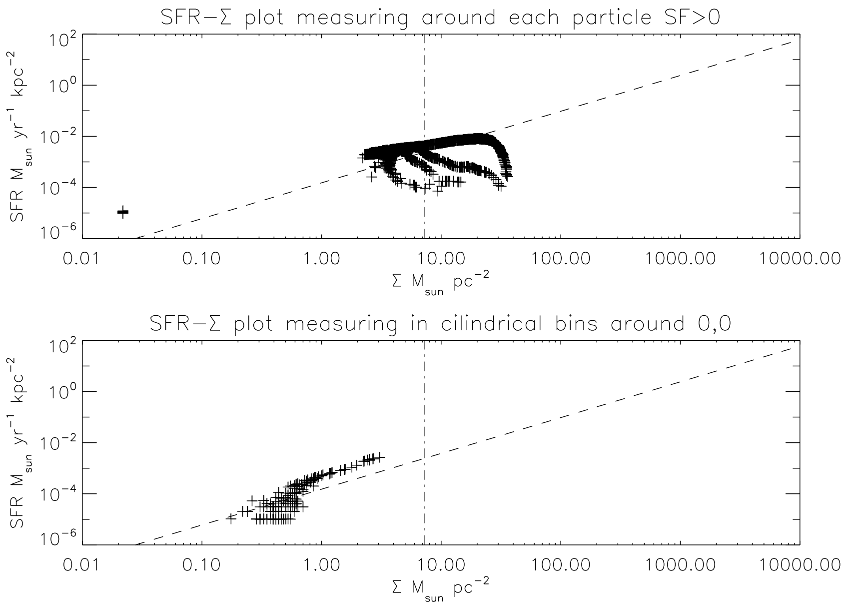

Figure 3.13: *Star formation rate-surface density plot for the simulation with a gas fraction of 0.3, a star formation density threshold of 0.1 cm^{-3} and an effective equation of state parameter $\gamma_{eff} = 4/3$. Upper plot: surface density measured in a region of 1 kpc^2 around each star forming particle. Lower plot: sfr and surface density in cilindrical bins of equal area (1 kpc^2) around the center of the disk*

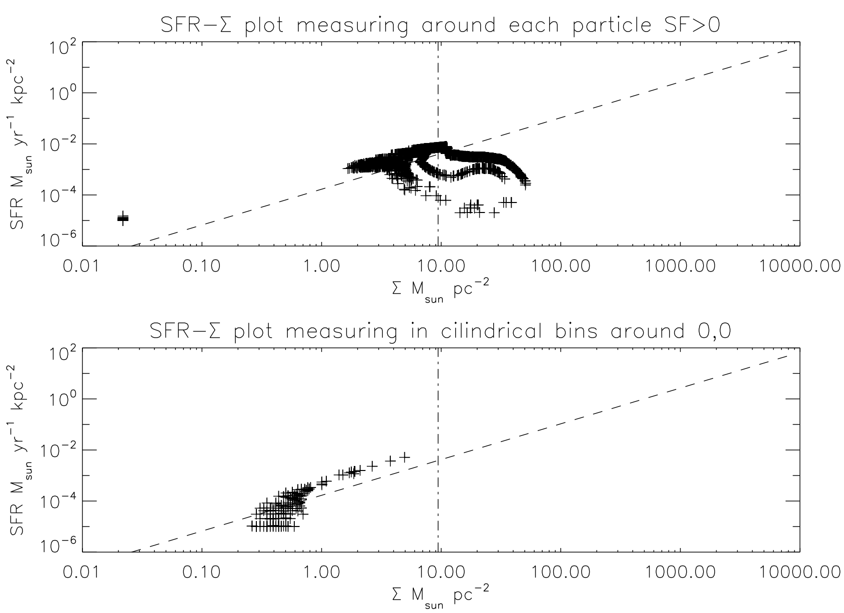

Figure 3.14: *Star formation rate-surface density plot for the simulation with a gas fraction of 0.5, a star formation density threshold of 0.1 cm^{-3} and an effective equation of state parameter $\gamma_{eff} = 4/3$. Upper plot: surface density measured in a region of 1 kpc^2 around each star forming particle. Lower plot: sfr and surface density in cilindrical bins of equal area (1 kpc^2) around the center of the disk*

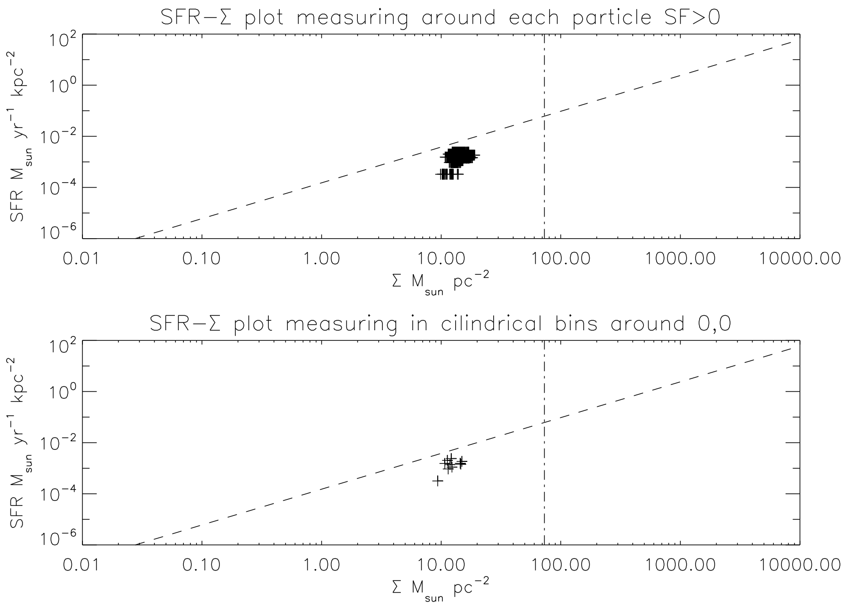

Figure 3.15: *Star formation rate-surface density plot for the simulation with a gas fraction of 0.3, a star formation density threshold of 10 cm^{-3} and an effective equation of state parameter $\gamma_{eff} = 4/3$. Upper plot: surface density measured in a region of 1 kpc^2 around each star forming particle. Lower plot: sfr and surface density in cilindrical bins of equal area (1 kpc^2) around the center of the disk*

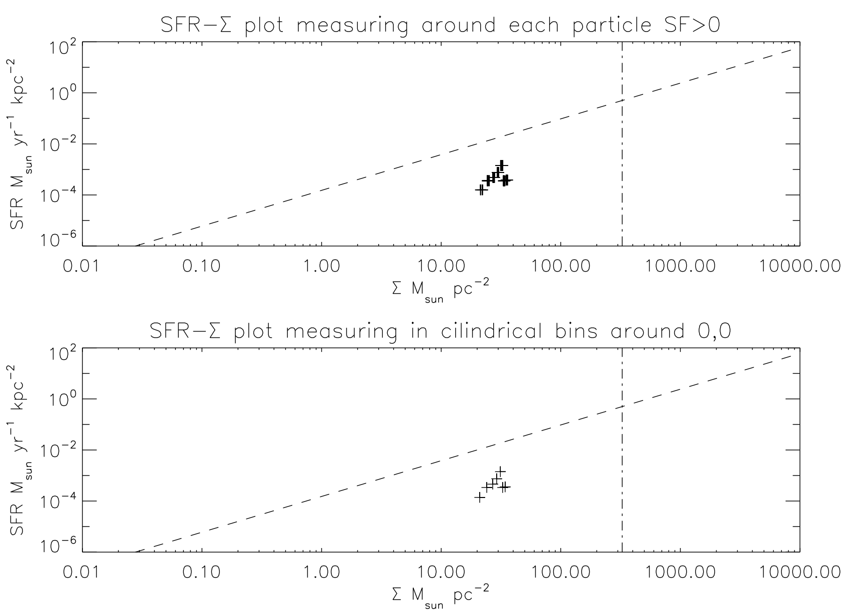

Figure 3.16: *Star formation rate-surface density plot for the simulation with a gas fraction of 0.3, a star formation density threshold of 200 cm^{-3} and an effective equation of state parameter $\gamma_{eff} = 4/3$. Upper plot: surface density measured in a region of 1 kpc^2 around each star forming particle. Lower plot: sfr and surface density in cilindrical bins of equal area (1 kpc^2) around the center of the disk*

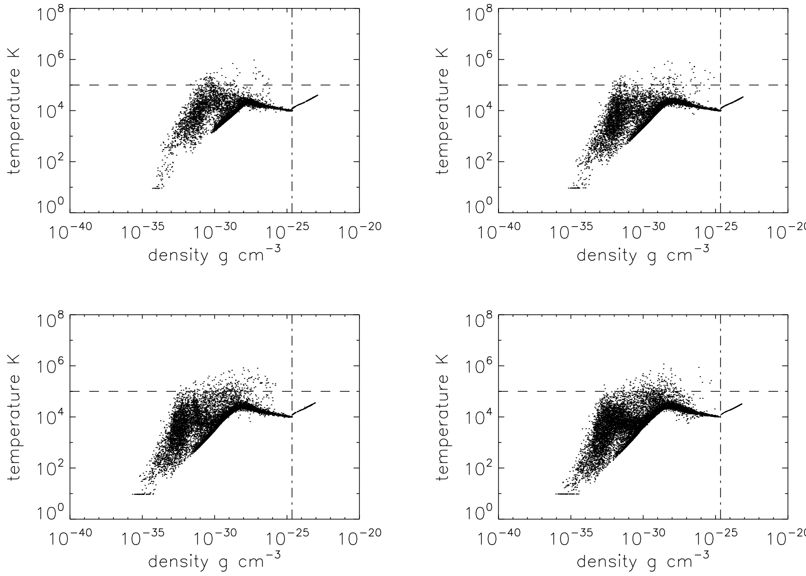

Figure 3.17: *Temperature-density plot for the simulation with a gas fraction of 0.3, a star formation density threshold of 0.1 cm^{-3} and an effective equation of state parameter $\gamma_{eff} = 4/3$. The plots are at 1, 2, 3 and 4 Gyr.*

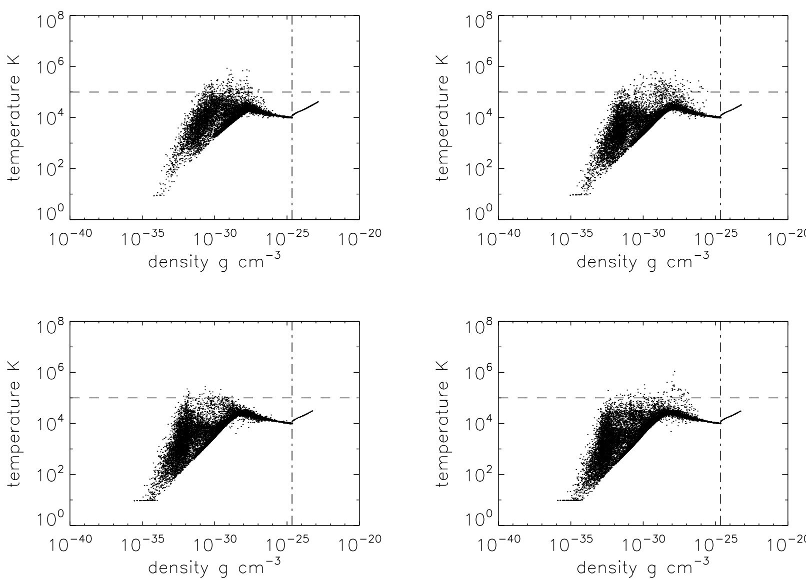

Figure 3.18: *Temperature-density plot for the simulation with a gas fraction of 0.5, a star formation density threshold of 0.1 cm^{-3} and an effective equation of state parameter $\gamma_{eff} = 4/3$. The plots are at 1, 2, 3 and 4 Gyr.*

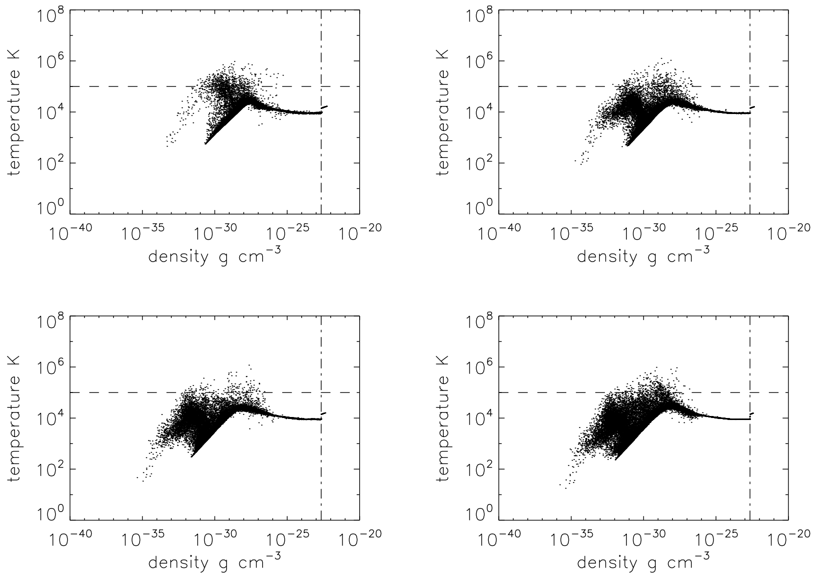

Figure 3.19: *Temperature-density plot for the simulation with a gas fraction of 0.3, a star formation density threshold of 10 cm*$^{-3}$ *and an effective equation of state parameter* $\gamma_{eff} = 4/3$*. The plots are at 1, 2, 3 and 4 Gyr.*

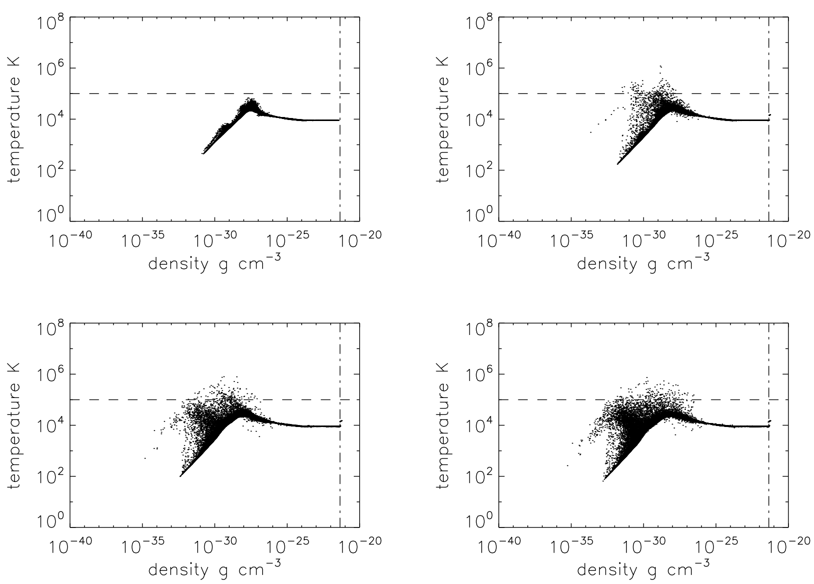

Figure 3.20: *Temperature-density plot for the simulation with a gas fraction of 0.3, a star formation density threshold of 200 cm*$^{-3}$ *and an effective equation of state parameter* $\gamma_{eff} = 4/3$*. The plots are at 1, 2, 3 and 4 Gyr.*

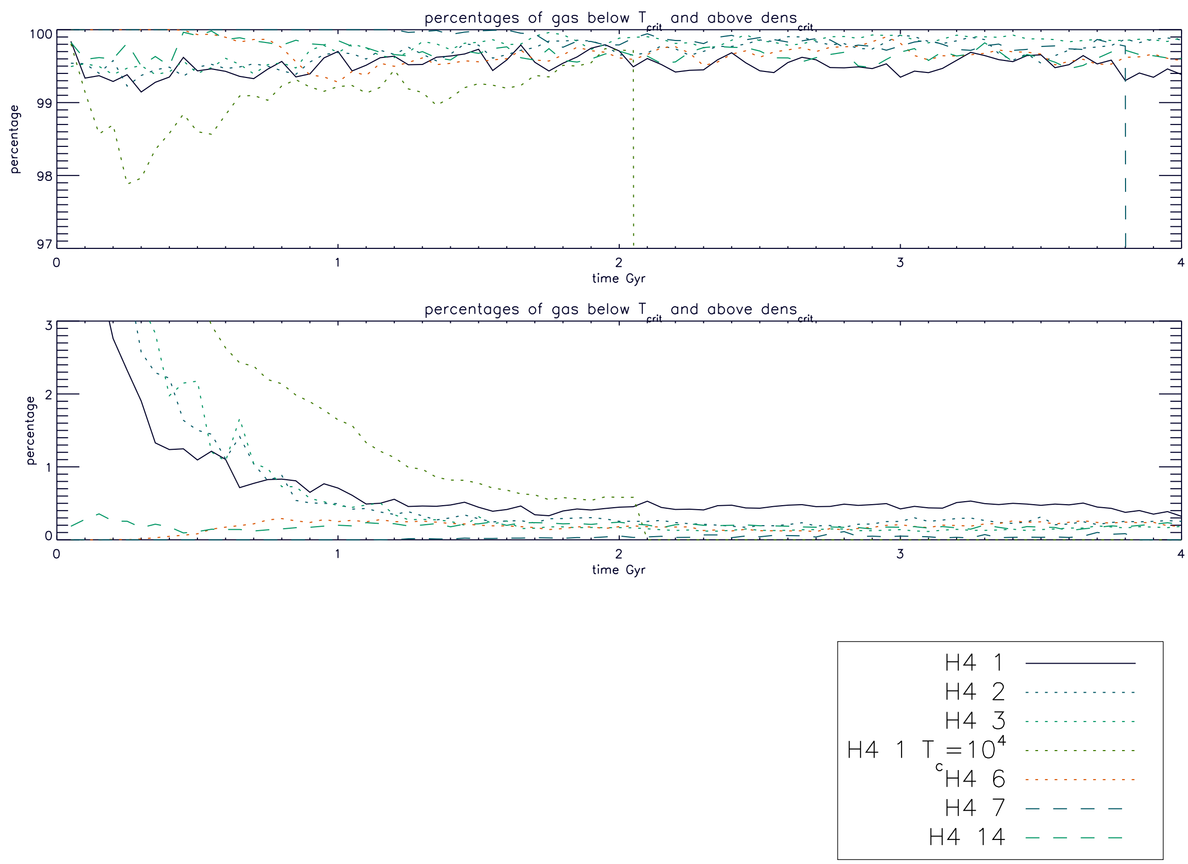

Figure 3.21: *Percentages of the gas below the temperature threshold ($T_c = 10^5$ K) and above the density threshold ρ_c for different simulations.*

Chapter 4

Mergers without gas

4.1 Introduction

In order to extend the studies on thickening of disks to higher mass ratio ranges and to study the thickening in dwarf galaxies we performed a set of four simulations. Four different disks, described in Section 3.1, are subjected to an accreting satellite. The disks have different masses, $M_{\rm disk2} = 0.5 M_{\rm disk1}$ and $M_{\rm disk3} = 0.2 M_{\rm disk1}$, the stability of the disks is the same for disk1, disk2_f18 and disk3 as their initial velocity dispersions are set in order to keep Q constant, while disk2_f9 has the same relations between the initial velocity dispersions as disk1 but therefore has a different initial value for Q. The satellite, its orbit and initial position and velocity are kept the same over the different simulations. The merger is followed for 6 Gyr and the inclination of the orbit is 30 degrees. A comparison of the mergers for the four different disks can be found in Section 4.2, while these results are compared to results of Hopkins et al. (2008), Velázquez & White (1999), Villalobos & Helmi (2008), Moster et al. (2010) and Purcell, Kazantzidis & Bullock (2009) in Section 4.3.

4.2 Results

The satellite clearly influences all four disks. The first pericenter passage is a very significant event. After this passage the satellite, even though it is much more massive than the disk, is almost completely destroyed, as can be seen in Figure 4.1, and the particles of the dark satellite slowly settle on orbits around the host halo center. All disks develop tails, rings and warps. For the most heavy disk, disk1, these features and some heating is about all the damage the satellite does. However for the lightest disk, disk3, the satellite seems to cause a rearrangement in the whole disk. This difference can be seen in Figure 4.2 where we show the evolution in time of disk1 and disk3. The axes are re-aligned such that they are along the principal axes of the disk, the x-axis along the major axis and the z-axis along the minor axis, respectively. All the following analysis is performed, and its findings are plotted, in the principal axes reference frame.

The idea that the satellite perturbs the lighter disks more strongly is evidenced by the vertical number density profiles. In Figure 4.3 we can see that immediately after the first passage, around 0.7 Gyr, the lighter disks are much more perturbed than disk1. The difference between the two disk2 experiments can be explained by the fact that disk2_f18 has a lower vertical velocity dispersion with respect to its radial and angular velocity dispersions than disk2_f9. Therefore it might be more easily disturbed in the vertical direction. The disk on average is initially more stable in the plane and is probably therefore more easily disturbed vertically. It can also be seen that the initial stability of both the disk2 does not have a large impact on the final vertical density profile, i.e. after 6 Gyr of

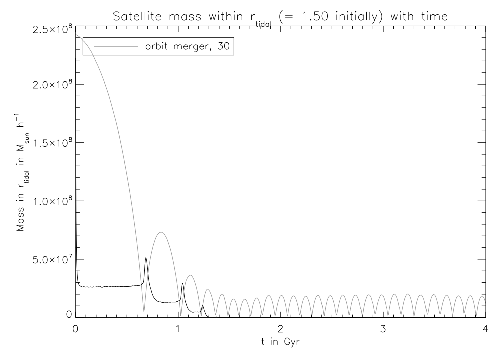

(a) *disk1*

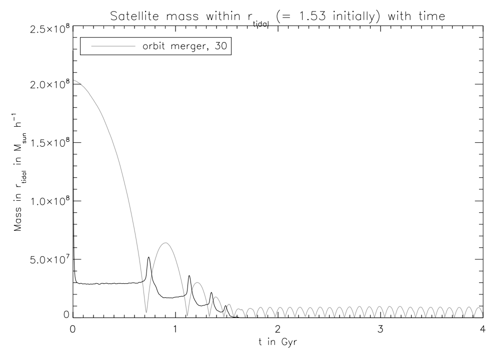

(b) *disk2f9*

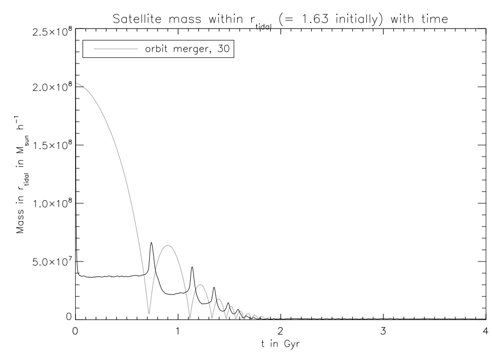

(c) *disk2f18*

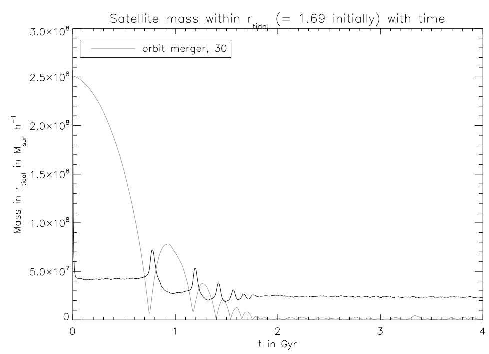

(d) *disk3*

Figure 4.1: *Mass of the satellite within the tidal radius during the merger events for all four disks. The initial tidal radius is given in equation 4.1 where r_{sat} denotes the initial position of the satellite with respect to the center of the host dwarf galaxy.*

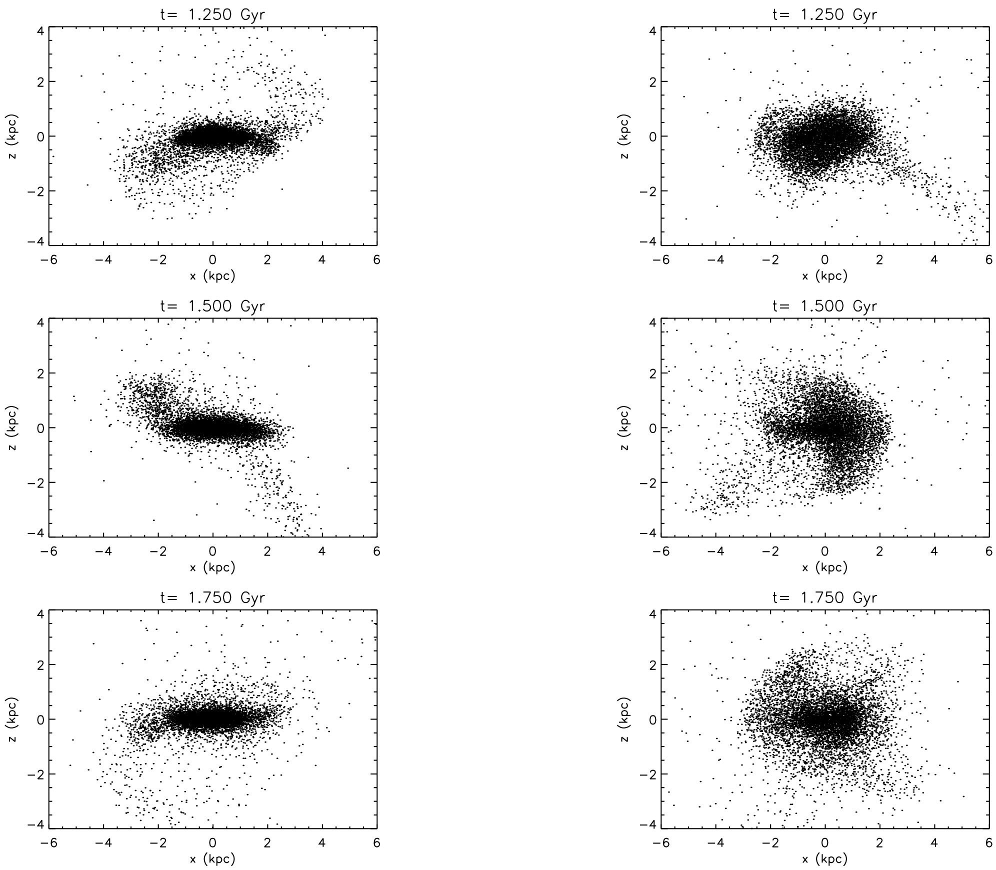

Figure 4.2: *Response of disk1 (left) and disk3 (right) on the disruption by the dark satellite. The distribution of 'star' particles is shown in the principal axes reference frame at each time.*

evolution. Both the disk2 have a comparable final vertical density profile while that of the lighter disk3 is much broader (a thicker and hotter disk) and that of disk1 is narrower (a thinner and colder disk). The big difference between disk1 and disk3, not only in final density profiles but also in speed of the reaction of the disk to the satellite, can be seen in Figure 4.4. This Figure shows the radial and vertical surface density profiles for the merger case. The vertical profile evidences that while disk1 thickens in steps, disk3 reaches its final thickness directly after the first pericenter passage. For the isolated case the less massive disk also has a thicker vertical distribution than disk1 as is discussed in Section 3.1. Figure 4.4 moreover shows that while the vertical profile changes due to the merger the radial surface density is very comparable to the isolated case (the initial, $t = 0$ Gyr, profile) for both disk1 and disk3. During the merger the radial profile is seen to change slightly, going back to a configuration similar to the original one later on in the simulations. This is in agreement with Purcell, Kazantzidis & Bullock, who find only slight changes in the radial scalelength for all their simulations.

Figure 4.1 shows the mass loss of the satellite during the accretion event for all four the disk models. Ideally one would use the gravitational potential to estimeate the tidal radius and mass loss of the satellite. This, however, is computationally expensive and we use an approximation for the tidal radius of the satellite instead. Initially the tidal radius is computed as

$$r_{\rm tidal} = \left(\frac{M_{\rm vir,sat}}{M_{\rm host}(\text{within } \mathrm{r}_{\rm sat})} \right)^{1/3} \tag{4.1}$$

where $r_{\rm sat}$ denotes the initial position of the satellite with respect to the center of the host dwarf galaxy. Following the merger the mass of the satellite within the tidal radius is measured. The tidal radius itself is recomputed every timestep using the satellite's mass within the tidal radius from the previous timestep. The tidal radius is updated only if that causes it to decrease in size. This causes the tidal radius to decrease sharply after each pericenter passage while it stays almost constant in between. The mass within the tidal radius then decreases in steps, going one step down every pericenter passage, though it increases for a very short time during pericenter as the satellite gets compressed in one direction and elongated in the other at pericenter. This effect disappears however if radii smaller than the initial tidal radius are considered.

Figure 4.5 shows how the vertical density profile of all four disks changes over time at different radii in units of the scalelength of the disks. Comparing the profiles for disk1 at different radii, one can see that disk1 maintains its disky appearance, evidenced by the exponential density profiles, even in the outskirts. The experiment disk3 on the other hand, appears to be very boxy in its outskirts, as the density distribution at large radii does not fall off exponentially anymore but seems to be nearly constant with height above the plane. Farther out all disks react faster to the merger and flares (it is more fragile in this region). This is of course also related to the plumes and tails that can be seen during the merging event. But even after the satellites settles in at the host center the outer disk is much more perturbed than the inner disk. This is in agreement with earlier studies (Kazantzidis et al. 2009; Velázquez & White 1999). Moreover, Velázquez & White (1999) found that the relation between radius and thickening is linear by rough approximation though Kazantzidis et al. (2009) claim that the flaring in the outskirts is more than a linear relation can explain. This means that one should be careful in comparing the thickening of disks with reference to the radius at which it is measured.

4.3 The mass ratio - disk thickening relation

Figures 4.5 and 4.3 show that there indeed seems to be a relation between the amount of thickening and the ratio of the mass of the disk and the mass of the satellite.

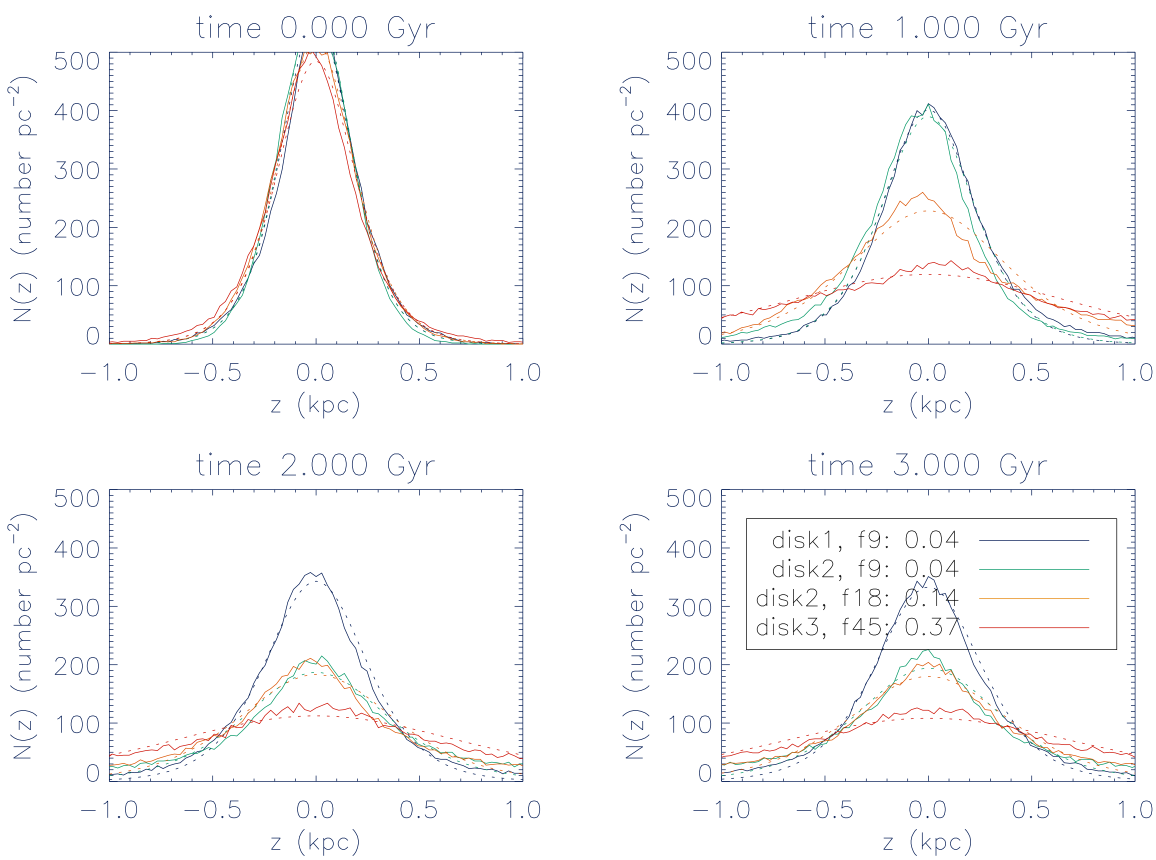

Figure 4.3: *Change in the Z profile during the merger for all four disks. The last value in the legenda indicates the value for z_0 fitted with $\Sigma_z \propto \frac{1}{z_0} sech^2\left(\frac{z}{2z_0}\right)$ at $t = 6$ Gyr*

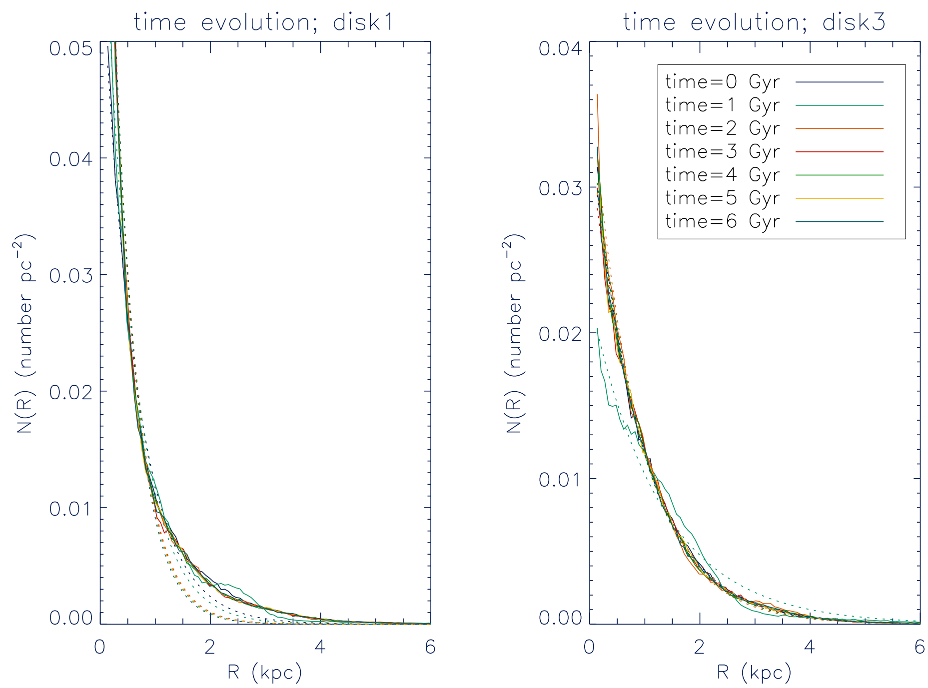

(a) *Radial profile*

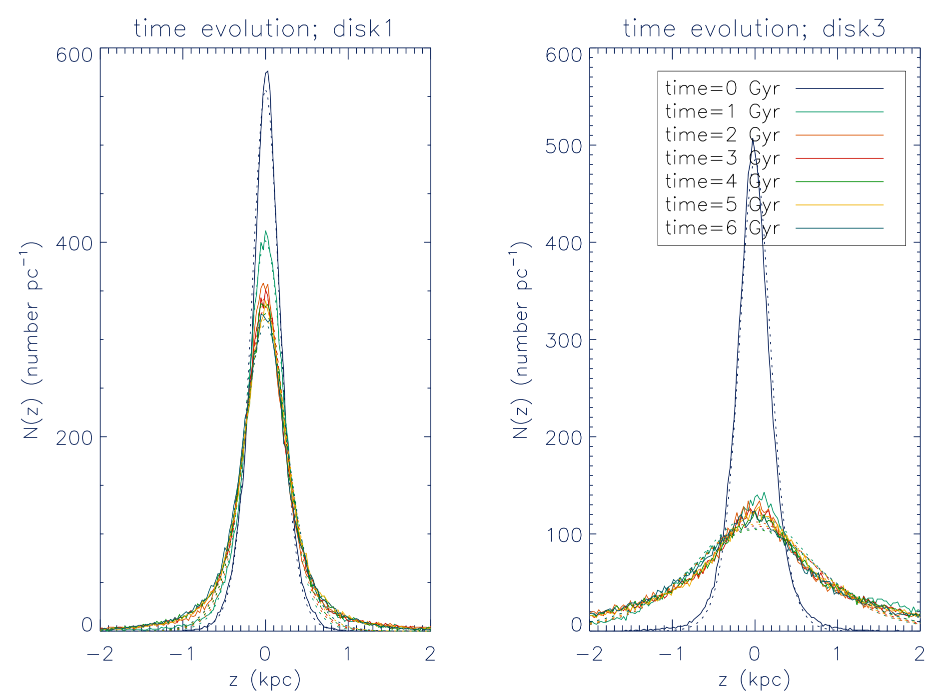

(b) *Vertical profile*

Figure 4.4: *Profiles plotted and fitted for disk1 and disk3 in the simulations with the satellite.*

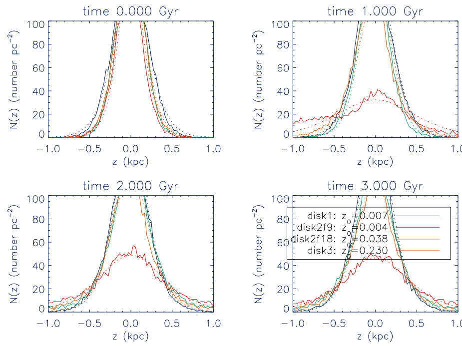

(a) *Within 0-1 scalelength in radius*

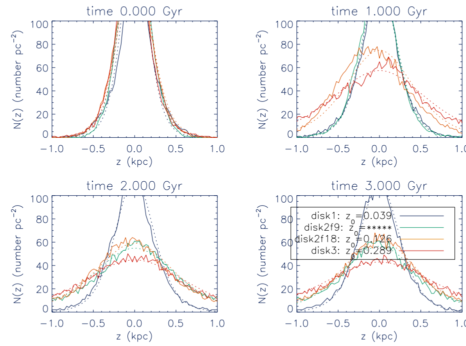

(b) *Within 1-2 scalelength in radius*

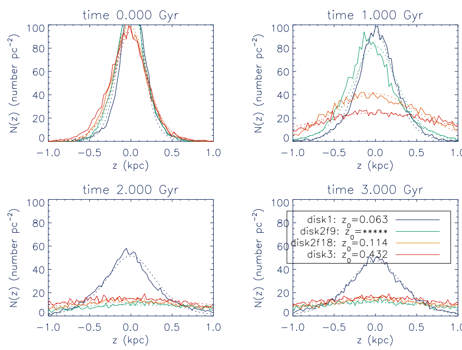

(c) *Within 2-3 scalelength in radius*

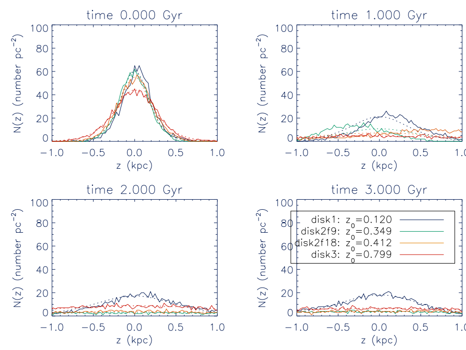

(d) *Within 3-4 scalelength in radius*

Figure 4.5: *Density profile for the Z direction in rings.*

In order to determine the form of this relation the data described above is compared and combined with data from Villalobos & Helmi (2008), Velázquez & White (1999), Purcell, Kazantzidis & Bullock (2009) and Moster et al. (2010). Hopkins et al. (2008) argue that the data from these first three papers and Younger et al. (2008) show that the relation is quadratic. It should be pointed out, however, that some of the data used is treated incorrectly by Hopkins et al. and overall, different definitions for the mass ratio are used and the range in mass ratios used to find the dependencies is very small. The indepedent variable for all data is said to be the mass of the satellite over the mass of the disk as is used in equations 1.3 and 1.4. For the data of Velázquez & White this is indeed what is done. For the data of Villalobos & Helmi however the plotted value of M_2/M_1 is the value of the total mass of the satellite over the virial mass of the host, not $M_{\rm sat}/M_{\rm disk}$. Correcting these points in the plots would indeed change the fitted relation already and very significantly so.

Figure 4.6 shows the thickening of disks due to mergers with respect to ratio between the virial mass of the satellite and the mass of the disk itself. The thickening is measured as the change in the scaleheight at the 'solar radius', and in these plots it is normalized to the initial value of the scalelength. This means that the radius at which the difference in disk thickness is measured has been converted to be approximately the same factor of scalelengths of the disk for data from Villalobos & Helmi and for data from this thesis as for the disks of Purcell, Kazantzidis & Bullock, Moster et al. and Velazquez & White. Velázquez & White, Moster et al. and Purcell, Kazantzidis & Bullock all simulate Milky Way-like disks and measure at a solar radius of 8.5 and 8.0 kpc with their disks having a radial scalelength of 3.5 and 2.84 kpc, respectively. We convert their solar radius to a solar-like radius for the smaller disks of the experiments presented in this thesis and the disks of Villalobos & Helmi by approximating it to be at 8/3 scalelengths. In this way the thickening is measured at respectively equal radii for all disks. This is very important even though we measure $\Delta H/R$ because of flaring in the outer regions of the disks as is explained in Section 4.2.

In the top panel in Figure 4.6 we plot in a linear scale, while the bottom is in logarithmic scale. The data points are from this thesis, Villalobos & Helmi (2008), Velázquez & White (1999), Purcell, Kazantzidis & Bullock (2009) and Moster et al. (2010) as listed in the figures. The points from Moster et al. are extracted directly from their figures instead of from tables so they are not as precise as the other data points. Moster et al. performed accretion simulations with and without a gas component in the host disk which partly describes their spread in $\Delta H/R$. They also found that, just as was shown by Purcell, Kazantzidis & Bullock, for an initial thinner disk the thickening is larger. This also is one of the possible explanations why the points of Purcell, Kazantzidis & Bullock lie distinctively higher than all other points. Furthermore, Purcell, Kazantzidis & Bullock do decribe their final disks as flaring. Moster et al. also noticed that the disks of Purcell, Kazantzidis & Bullock experienced significantly more thickening than theirs, despite the fact that the disk parameters used by Moster et al. were modelled after Purcell, Kazantzidis & Bullock. In Section 1.3 in this thesis is described how Moster et al. attempt to answer why their thickening is less. Influences other than initial disk thickness include the total masses of the disk and satellite, the orbit of the satellite and the profiles and concentrations of both the satellite and the host galaxy. In all studies it is clear that many parameters influnce the particular effect a merger has on a disk, globally as well as locally. In general Figure 4.6 shows that the data could be fit by a linear relation between disk thickening and satellite:disk mass ratio, but it clearly is not well fit by a quadratic function. This implies that though the reasons why Hopkins et al. changed the relation from Toth & Ostriker are generally supported, their arguments and mathematics seem to be flawed. The analysis and dependence by Toth & Ostriker clearly describe the relation for satellite accretion and disk thickening better.

One of the reasons for the large scatter is possibly that all studies use different measures for the thickening of the disk, Velázquez & White use $< z^2 >^{1/2}$, while Purcell, Kazantzidis & Bullock estimate $< |z| >$, median($|z|$) and fit a double sech^2 to find a $z_{0,\rm thin}$ and a $z_{0,\rm thick}$, i.e. they fit two disks simultaneously. For the data of this thesis and of Moster et al. and Villalobos & Helmi a single sech^2 has been fitted to find a scaleheight. This means that in order to compare the different simulations in a fair way some measures had to be converted in others. We measure the values for $< z^2 >^{1/2}$, z_0 and $< |z| >$ for all simulations from Villalobos & Helmi and this thesis at different radii. The values for all three measures at different radii for both sets of simulations can be found in Figure 4.7. These are then used to fit a relation between the different measures, as is plotted in Figure 4.8. There is significant scatter between the different scalheight measures but the ratio between them remains fairly constant with radius. Finally, these transformations are used to convert the measurements of $< z^2 >^{1/2}$ and $< |z| >$ provided by the different authors to a value for the scaleheigth of a single sech^2 distribution, z_0. As the radius at which the thickening is measured does have an influence on the measured thickening, the difference in scaleheight between the initial disk and the final disk is divided by the radius at which it is measured. This reduces the differences in measurements between the different data sets further. One should note, however, that there can still be a discrepancy between the values found for $\Delta H/R$ around the solar radius and in the outskirts of the disks due to disk flaring as a result of the minor merger, as Purcell, Kazantzidis & Bullock noticed for their disks.

Figure 4.9 shows the relation for all studies discussed here between thickening of the disk due to a minor merger and the ratio between the disk mass and the total virial mass of the host. This last parameter is closely related to the galaxy efficiency used by Sales et al. (in prep.). The relation between galaxy efficiency and thickening of the disk due to a minor merger seems clearer than the relation of the thickening with disk-satellite mass ratios. Smaller disks in a dark matter host halo will thicken more easily than larger disks in the same host halo. The symbols in the figure are color coded based on the ratio $M_{\rm vir,sat}/M_{\rm disk}$ that was presented in Figure 4.6. This, again, shows that mergers with a larger mass ratio between the total satellite mass and the disk mass of the host will thicken

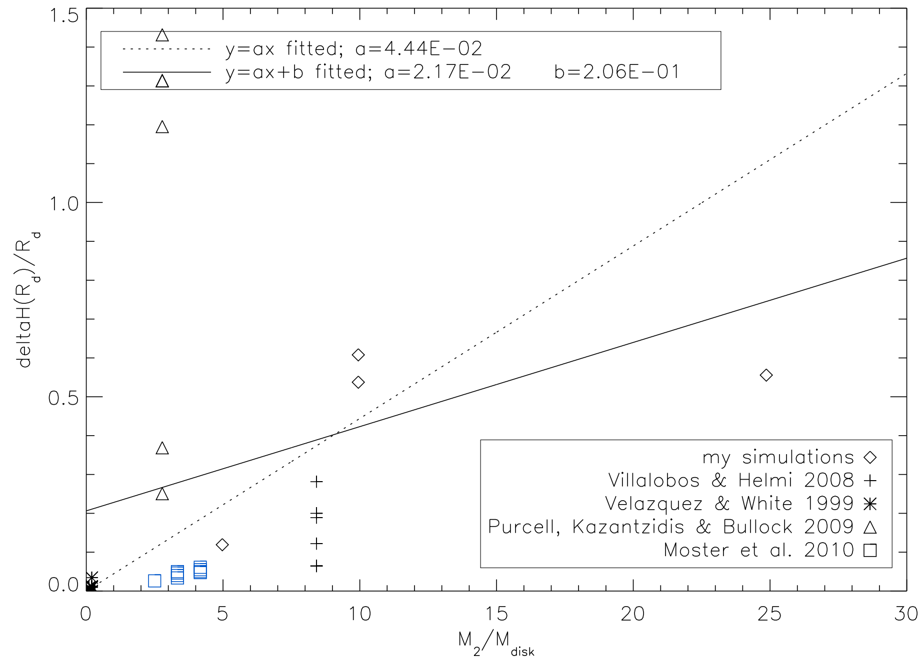

(a) *linear-linear plot*

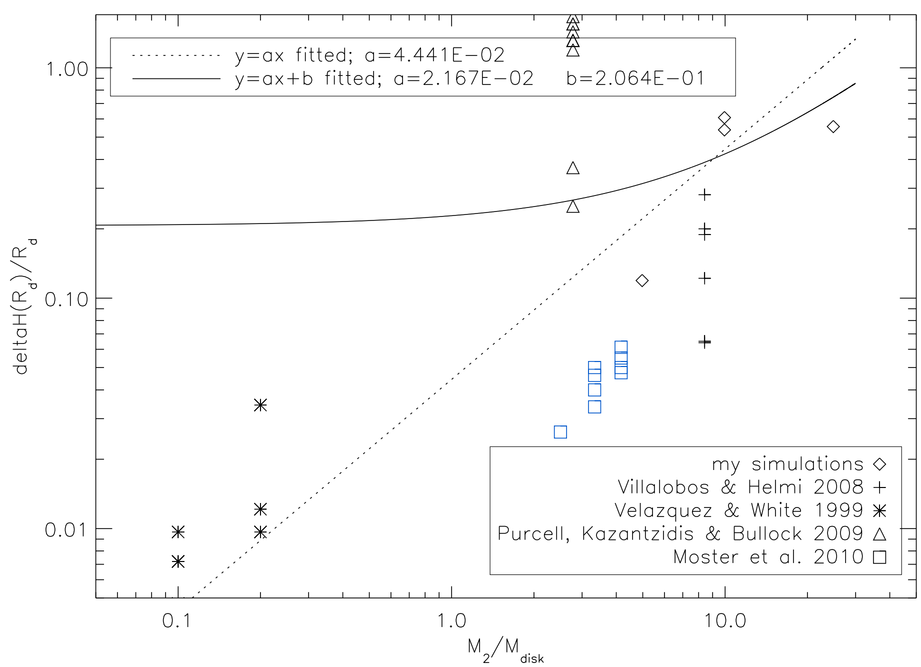

(b) *log-log plot*

Figure 4.6: *The thickening induced by a satellite with respect to the ratio of the mass of that satellite to the mass of the disk for different studies (Villalobos & Helmi (2008), Velázquez & White (1999) Purcell, Kazantzidis & Bullock (2009), Moster et al. (2010) (light blue; taken from figures instead of from tables) and the data presented in this thesis). The lines are simple polynomials fitted to the points.*

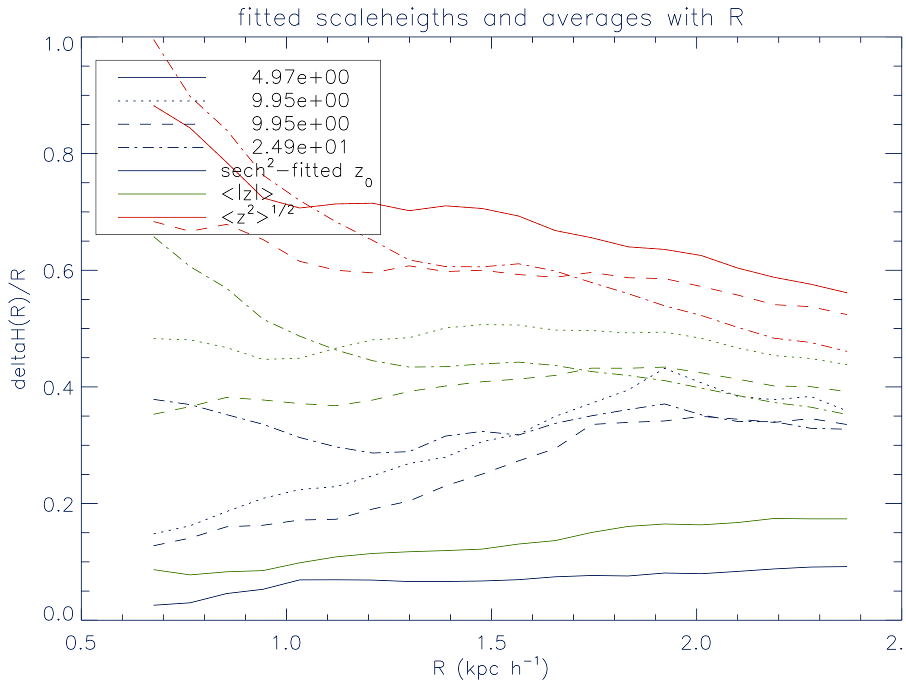

(a) *z_0, $<|z|>$ and $(<z^2>)^{1/2}$ for my data*

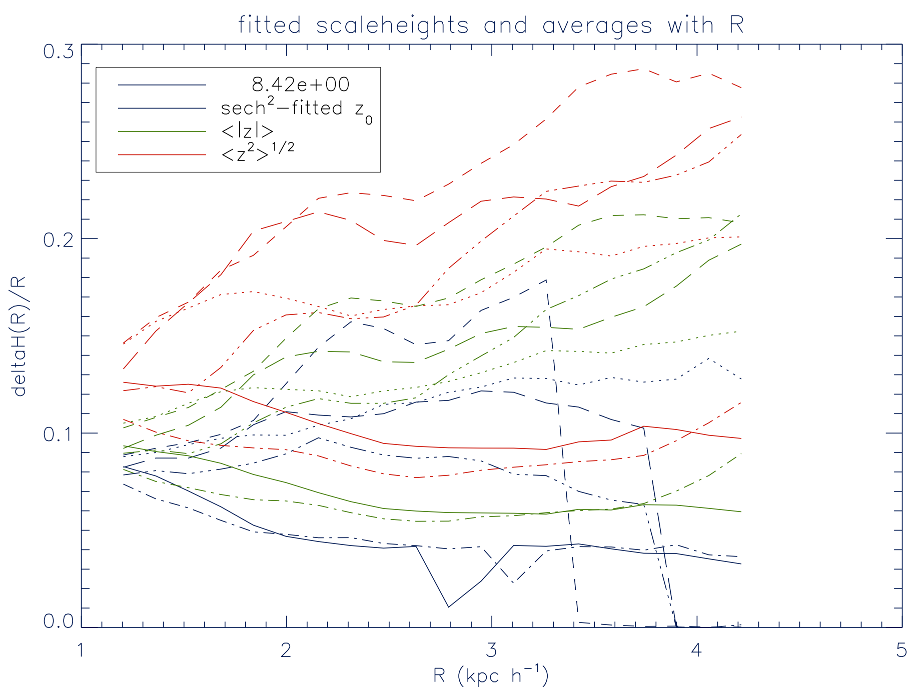

(b) *z_0, $<|z|>$ and $(<z^2>)^{1/2}$ for data from Villalobos & Helmi (2008)*

Figure 4.7: *The thickening induced by a satellite measuring z_0, $(<z^2>)^{1/2}$ and $<|z|>$ at different radii for two different studies.The color codings denote the different measures of scaleheight used and the different lines are different experiments. The values in the legend give the values for the $M_{vir,\,sat}$-M_{disk} ratio.*

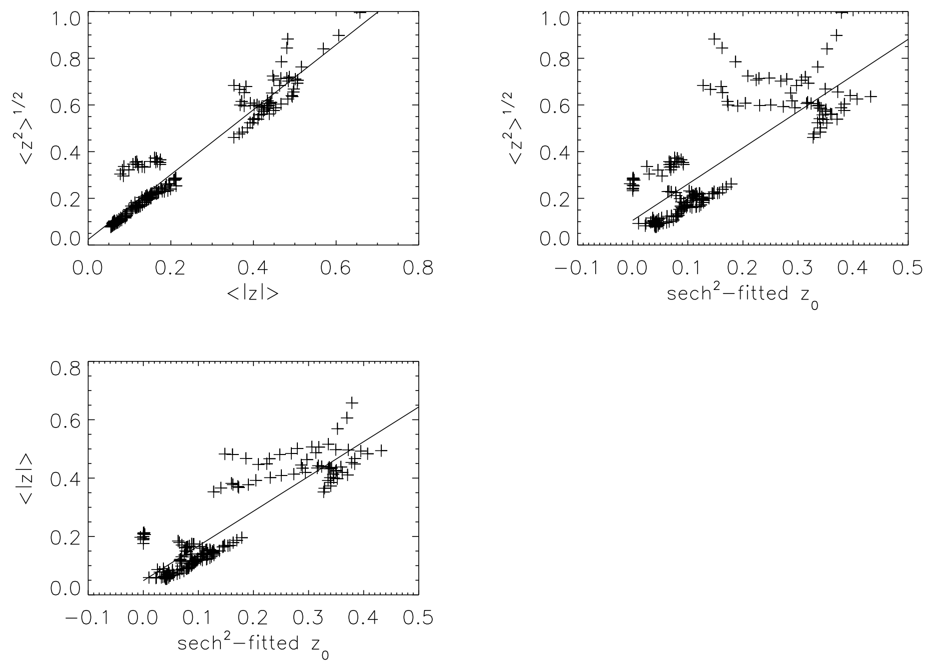

Figure 4.8: *Fitted relations between z_0, $(< z^2 >)^{1/2}$ and $< |z| >$ fot data from this study and data from Villalobos & Helmi (2008). Note that there is quite some scatter within the different measures of scaleheight.*

the host disk more.

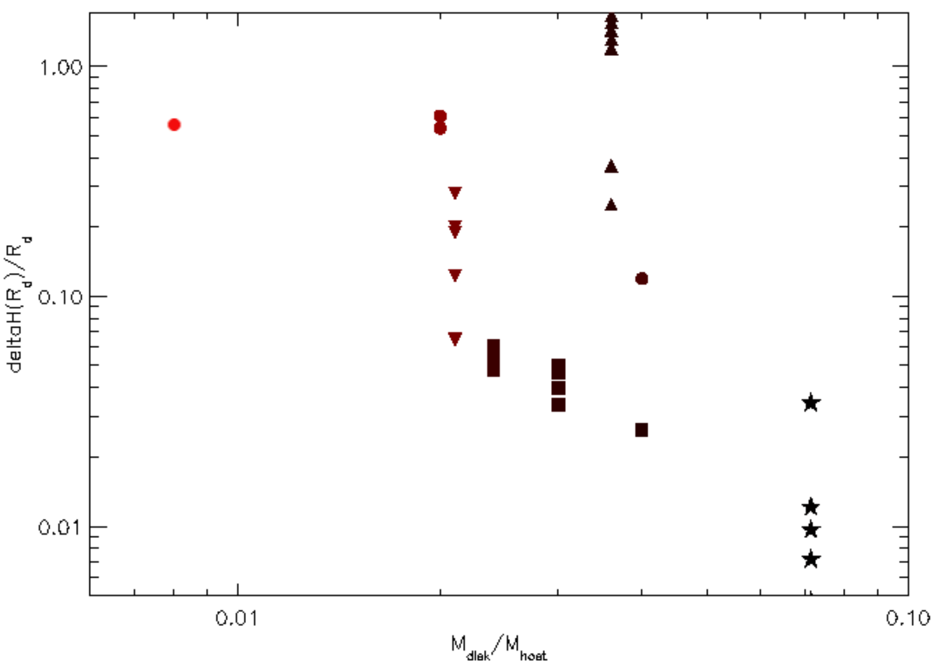

Figure 4.9: *The thickening induced by a satellite with respect to the ratio of the mass of the disk to the virial mass of the host for different studies: Villalobos & Helmi (2008; upside down triangles), Velázquez & White (1999; stars), Purcell, Kazantzidis & Bullock (2009; upright triangles), Moster et al. (2010; squares) and the data presented in this thesis (circles). The symbols are color coded for the satellite-disk mass ratio which was shown in Figure 4.6:a lighter red color means that $M_{vir,sat}/M_{disk}$ is larger.*

Chapter 5

Mergers with gas

5.1 Introduction

The gas in merging galaxies responds to the tidal forces and torques by flowing radially inwards and outwards. A summary of this can be found in Section 1.3 following Bournaud (2011). The outflowing gas will form part of the plumes, bridges and tails which are observed in peculiar galaxies. It has been suggested that tidal dwarf galaxies could form in these outflows. The outflowing gas is lost and eventually could be re-accreted, depending on the gravitational potential of the host and the outflow velocities. Inflowing gas, on the other hand, accumulates near the center and can fuel a starburst if a sufficient amount of gas is flowing in and if the gas gets sufficiently dense. Di Matteo et al. (2008) show that only a small amount of the mergers trigger a starburst in their suite of hydrodynamical simulations. Moreover the mergers that do trigger a starburst are mostly major mergers. We performed simulations of mergers with dark matter halo mass ratios of 1:5 and 1:16, minor mergers. The primary system, however, is a dwarf galaxy, which have less baryonic content. With respect to the disc-satellite mass ratio these can be though of as major mergers. Therefore it is very interesting to see the effect of such a merger on the gas in the disk of a dwarf galaxy.

5.2 Results

The first merger simulations that we performed involved a satellite of a total mass comparable to the disk mass of the dwarf galaxy. The disk setup and the parameters governing the fraction of gas in the disk, the effective equation of state and the star formation threshold here are as the initial isolated disks described in Section 3.2. Though we considered the main characteristics and star formation rates in the disk unrealistic we still performed simulations of mergers of this disk with a dark satellite of $M_{\rm vir} = 5.96 \times 10^8 M_\odot$. The satellite was put on three different orbits in the halo of the host system. Following the properties found for a satellite in a dwarf system in the Aquarius simulations as given in table 2.1 gives a 'polar' orbit: the satellite approaches the central dwarf galaxy with an inclination of almost 90 degrees. The 'frontal' orbit uses the same initial positions but the initial velocity of the satellite is directed straight at the center of the host (a purely radial orbit). This induces the satellite to directly plunge through the disk of the dwarf galaxy at first pericenter. Two more orbits with different inclinations are explored, one prograde, almost in the plane of the disk, and a second, also prograde, with an inclination of 30 degrees. Figure 5.1 shows the star formation rates for the isolated dwarf galaxy, the merger of the dwarf galaxy with a dark satellite on the polar, planar and frontal orbit and for the isolated galaxy without the implementation of supernova feedback and a merger case with the satellite on the planar orbit without feedback. The exact properties of all these

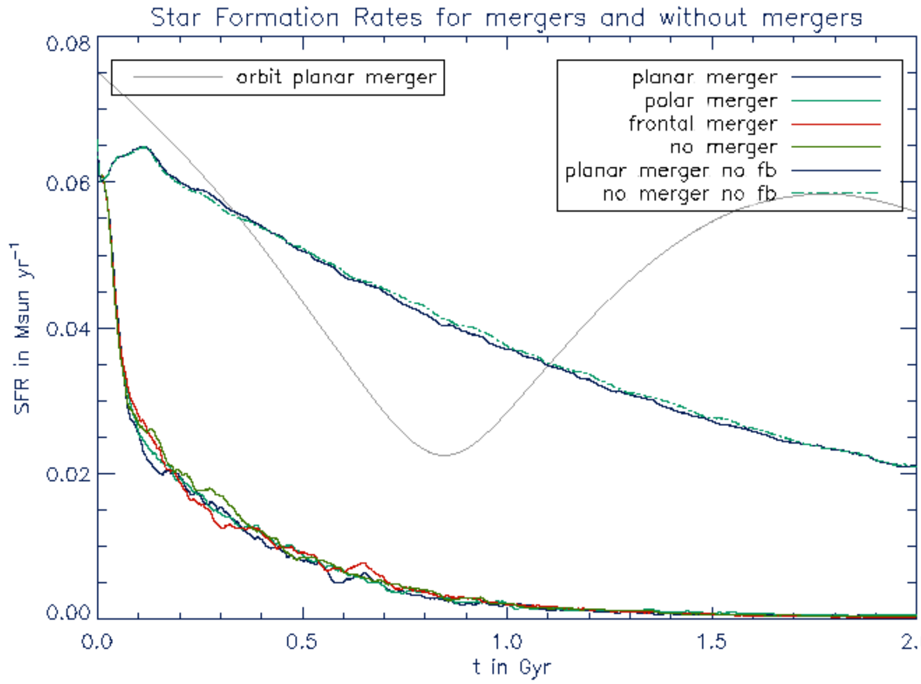

Figure 5.1: *Star formation rate for the initial settings of the dwarf galaxy with gas, in isolation and with an infalling satellite, and with and without feedback.*

simulations can be found in tables 2.2 through 2.4.

As can be seen in Figure 5.1 even though the star formation rate is very low after the initial peak for the isolated dwarf system the dark satellite does not have a significant effect on the star formation rate. Suspecting the initial burst of star formation caused a dilution of the gas and thereby almost inhibited further star formation, we performed a simulation in isolation and with the satellite on a planar orbit without supernova feedback. Even in this case the merger does not have an effect on the star formation rates of the dwarf galaxy. Figure 5.2 supports this view. The figure shows the gas mass within the inner 1 kpc for the host system for the isolated case and the case with the satellite on the planar orbit, both with and without the implementation of supernova feedback. It is clear from Figure 5.2 that the merger with a dark satellite in these cases does not induce a gas flow to the center of the host and does not enhance the star formation in the host system. As this is the case for three quite different orbits of the satellite we suspect that the cause of the absence of any significant effect of the merger on the host lies with a too small mass ratio between the virial masses of the dwarf system and the satellite or in the setup of the dwarf galaxy and in the density of the satellite. In Section 3.2 a number of reasons are given why we needed to change the initial conditions for the dwarf galaxy. These changes were seen to have an effect on the star formation rates. Therefore we now explore a subset of those initial conditions in the case of the merger with a dark satellite.

Considering the results presented in Section 3.2, we subsequently performed simulations of the merger of a dwarf galaxy and a dark satellite using the dwarf galaxy models H4 1 and H4 14. The properties that changed for these simulations with respect to those discussed above can be found in table 2.4. Besides changes in the initial conditions of the host dwarf system and the physical parameters governing star formation, we also changed the mass of the satellite. For satellites falling into a Milky Way-like galaxy the satellites generally really perturb the host disk if they have a mass ratio of approximately 1:5 or larger. Therefore we set the mass of our new satellite to $0.2 M_{\mathrm{vir,\,host}} =$

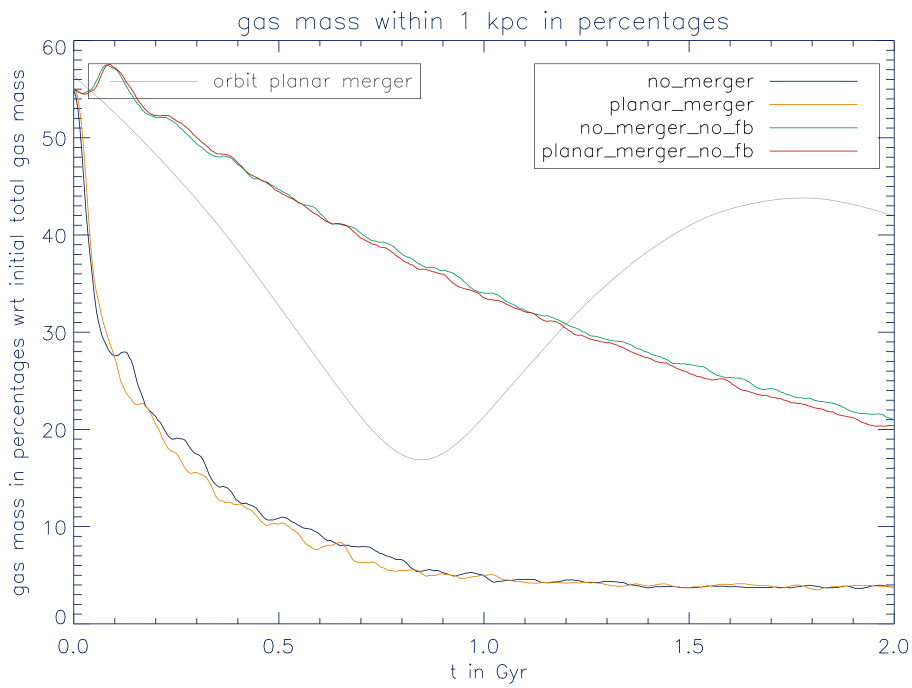

Figure 5.2: *Gas mass within the inner 1 kpc in percentages with respect to the total gas mass for the initial settings of the dwarf galaxy with gas, in isolation and with an infalling satellite on a planar orbit, and with and without feedback.*

$2 \times 10^9 M_{\odot}$. Haloes of this size are in a transition region, and may be completely dark but some could also host a luminous galaxy.

Merger simulations of dwarf galaxy model H4 14 are performed with the more massive satellite on the planar, polar, frontal and $i = 30$ orbits. The star formation rates for these simulations can be found in Figure 5.3. The figure shows that most of the mergers do not change the star formation rates by more than a factor 2 or 3, they are slightly smaller around the first pericenter and slightly larger later on. However, the merger on the planar orbit has a significant burst of star formation with an increase in the SFR of a factor 10. This starburst however, is not centrally concentrated, but shows two epicentres. Figure 5.4 shows how in the second encounter the dark satellite catches gas from a spiral arm that was formed as a result of the first close tidal interaction. There are two main star forming regions: the gas that starts to form stars in the center of the dark satellite, and the star formation in the center of the host system. This means that the satellite on the planar orbit did induce a starburst but not just the conventional one where gas is channelled to the center of the primary system due to tidal forces from the encounter. One could even see this as a way for dark systems to light up, even though the satellite will eventually be ripped apart and absorbed by the dwarf galaxy.

Figure 5.6 shows the consumption of gas for all merger cases and the isolated case for the H4 14 model and a planar merger case for the H4 1 model. The H4 1 model has the conventional values for the star formation parameters, $\rho_{\mathrm{thresh}} = 0.1\ \mathrm{cm}^{-3}$, $\gamma_{\mathrm{eff}} = 4/3$ and there is 30 % gas in the disk. Model H4 14 has a gas fraction fo $f_g = 0.5$, a star formation threshold of $\rho_{\mathrm{thresh}} = 10\ \mathrm{cm}^{-3}$ and $\gamma_{\mathrm{eff}} = 1.4$. In the H4 1, planar merger, simulation a similar event takes place as with the H4 14, planar merger simulation. As there is less gas in total the star formation rate peak due to the satellite catching in some gas, cannot be as high as for model H4 14. That this is indeed the case, can be seen in Figure 5.5. Keep in mind however that the isolated model H4 1 also has a slightly lower star formation rate

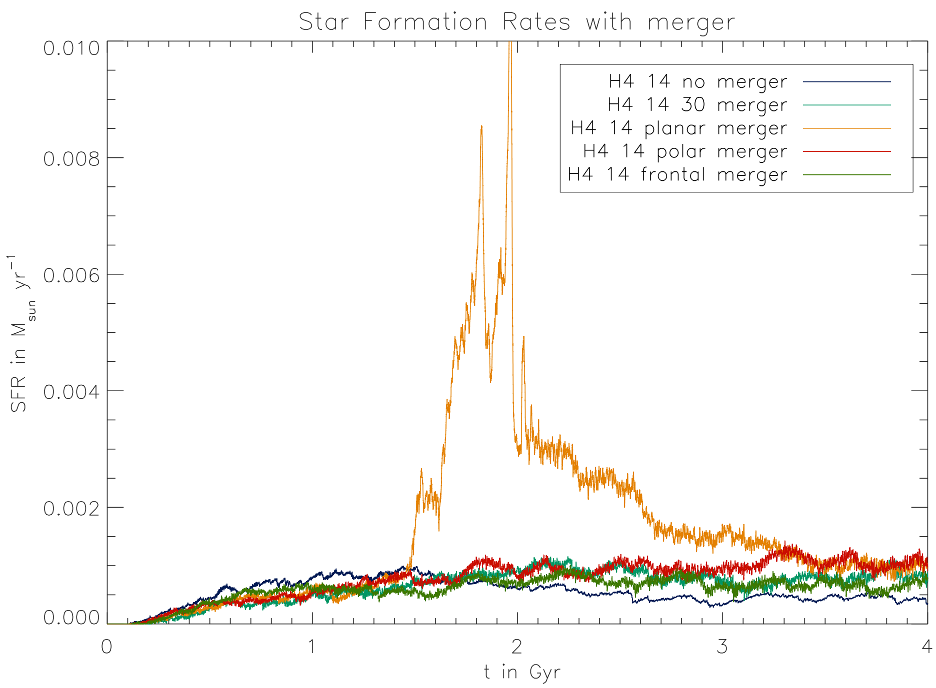

Figure 5.3: *Star formation rate for the H4 14 model for the dwarf galaxy with gas, in isolation and with an infalling satellite on 4 different orbits.*

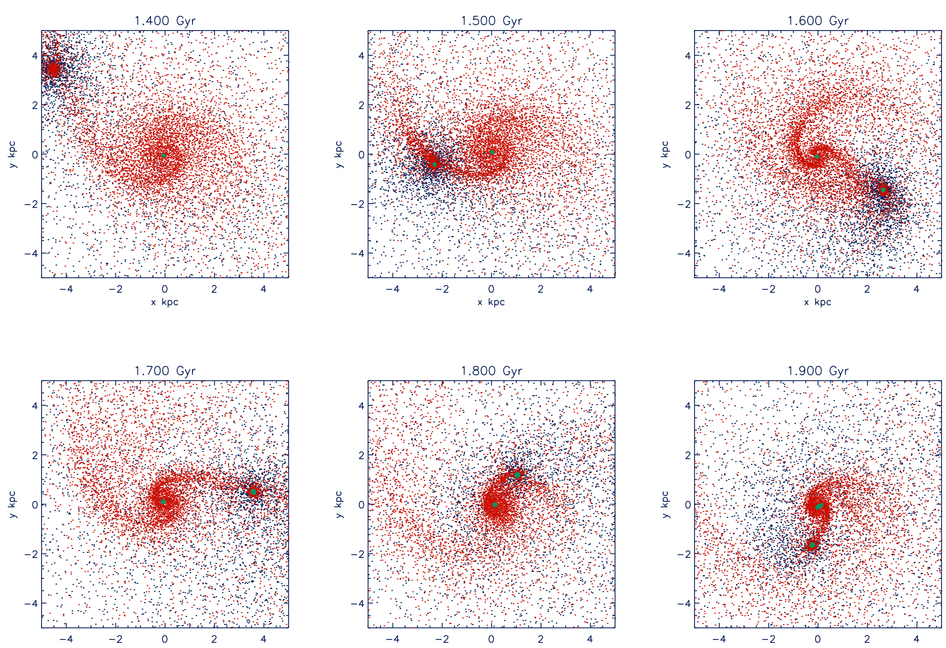

Figure 5.4: *Snapshots around the time of the second encounter for the H4 14 model for the dwarf galaxy with gas and the dark satellite on the planar orbit. Shown are the dark matter halo of the satellite (dark blue; 2% of all particles shown), the gas in the disk of the dwarf galaxy (red; 20% of all particles shown) and the locations of current star formation (green).*

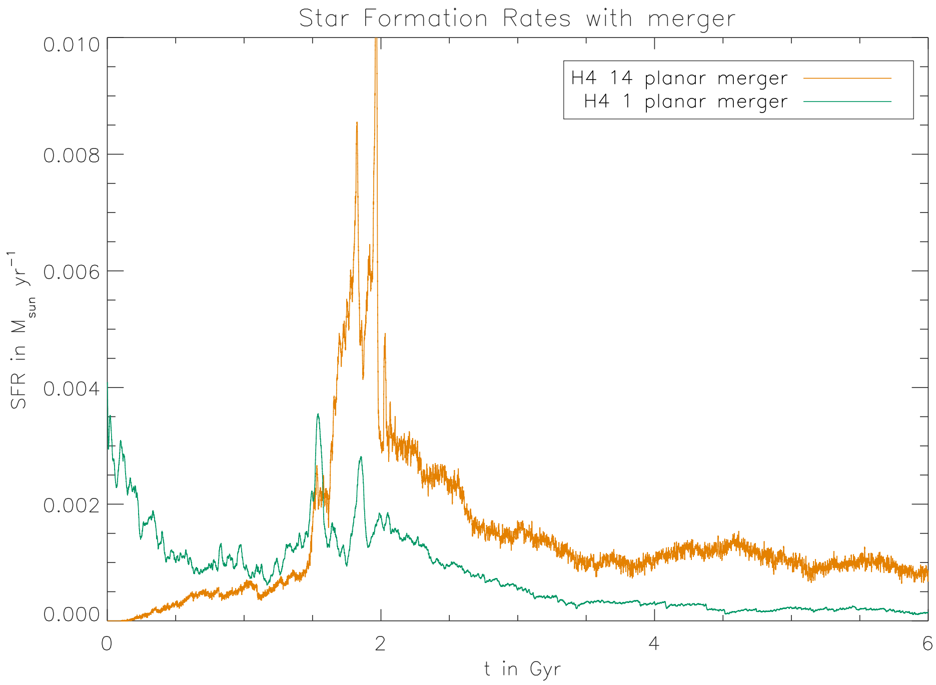

Figure 5.5: *Star formation rate for the H4 14 and the H4 1 model for the dwarf galaxy with gas, with an infalling satellite on the planar orbit.*

than model H4 14 as is discussed in Section 3.2 and shown in Figure 3.11. And with respect to Figure 5.6 one should note that the percentage of the consumed gas with respect to the initial total gas mass is decreasing faster initially for the H4 1 model than for the H4 14. After 6 Gyr the gas consumption is similar again.

The above simulations show that though the mergers with dark satellite do perturb the gas disk of the dwarf galaxy models the effect on the star formation is small, and only an increase of a factor of few is observed in most cases. The only exceptions are when gas gets caught in the center of the dark satellite and therefore then gets dense enough to form stars. Considering the discussion in Section 3.2 about the star formation in the dwarf galaxy models the problem lies more with the star formation prescription in general. The satellites do effect the gas just as the stars. This is shown in Figure 5.7. The fraction of gas in the inner 1 kpc does not change dramatically due to the merger but effects can be seen around the first pericenter for most of the simulations and after the second pericenter for the planar orbit and polar orbit for the model H4 14. Increasing the star formation in the isolated dwarf galaxy should enhance these small effects. Then the dark satellites probably would induce a starburst-like event.

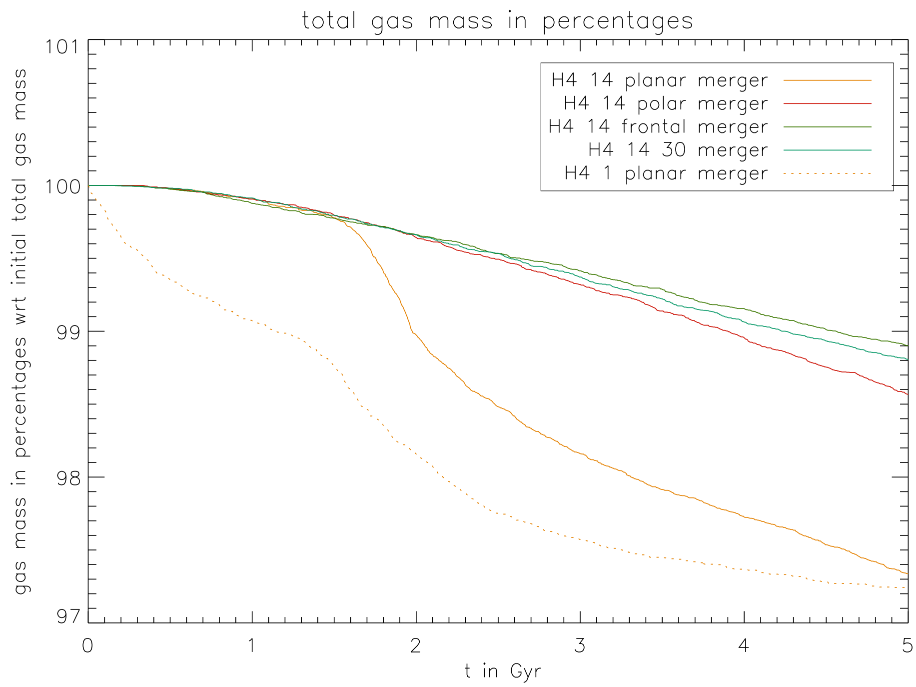

Figure 5.6: *Total gas mass in percentages with respect to the initial gas mass for the H4 14 and the H4 1 model for the dwarf galaxy with gas, with an infalling satellite on a planar orbit for the H4 1 model and on 4 different orbits for the H4 14 model.*

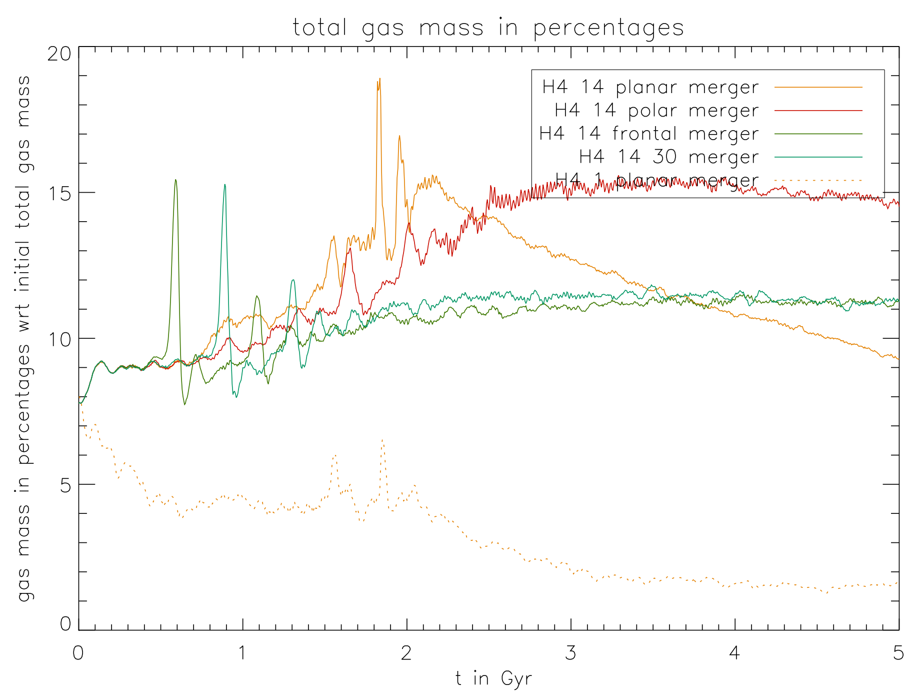

Figure 5.7: *Same as Figure 5.6 except plotting the gas mass within the inner 1 kpc in percentages with respect to the initial total gas mass.*

Chapter 6

Summary and conclusions

The structure we see in the Universe is thought to have been formed in a hierarchical manner. The ΛCDM standard cosmogony prescribes that galaxies, and structures in general, grow through merging. For galaxies this means that not only the dark matter haloes merge to form one bigger halo but that also the baryonic content of those haloes is subjected to this process. In a CDM paradigm however, there should be starless haloes; haloes below a certain (mass) threshold have not been able to form stars due to ionizing radiation, too low a baryonic mass to develop the instabilities that lead to star formation, and gas loss. In cosmological simulations based on the cold dark matter theory these small dark haloes are abundant. Dwarf galaxies, for example those in the Local Group, are above that threshold but seem to have a larger mass-to-light ratio and have had less efficient star formation than larger galaxies. These dwarf galaxies sometimes have bursty star formation histories, and show a wide variety in gas content, structural properties, kinematics and metallicity. According to cosmological simulations like the Aquarius simulations (Springel et al. 2008), these satellites, or the dwarf galaxies that will become satellites can have substructure themselves. They accrete smaller haloes and occasionally can have a major merger. The satellites in that case however then should be predominantly dark.

A number of the Local Group dwarfs are clearly influenced by the dominant large galaxies as the Milky Way and have been subject to tidal effects. They are expected to eventually end up as the streams which are observed in the Milky Way halo and around other galaxies or to perturb or heat the disk if their pericenter is close enough. These minor mergers can perturb the disk of a host galaxy but there is no agreement in the literature on the dependence of the thickening of the disk on the ratio between the total satellite mass and that of the disk itself. For example Toth & Ostriker (1992) propose a linear dependence, while Hopkins et al. (2008) on the other hand claim that the relation is quadratic.

This thesis presents a suite of controlled simulations of dwarf galaxies and dark satellites. The initial conditions are inspired by data from the Aquarius-C-2 simulation provided by Laura Sales. Our dwarf galaxy model is based on the $M_{\rm vir} = 10^{10} M_\odot$ dwarf model by Dalla Vecchia & Schaye (2008). The dark satellite is modelled following a Navarro, Frenk & White (1996) profile. We evolved both satellite and dwarf galaxy in isolation and simulate their mergers both with and without gas in the dwarf galaxy.

For the simulations without gas three dwarfs with different disk masses are modelled. While the masses vary the Toomre stability parameter Q is kept fixed. In this way the thickening of the galaxy disks due to the same infalling satellite can be measured with respect to the changing disk mass. Combining simulations from Villalobos & Helmi (2008), Moster et al. (2009), Purcell, Kazantzidis & Bullock (2009) and Velázquez & White (1999) we find that the thickening of a disk depends linearly with $M_{\rm vir,sat}/M_{\rm disk}$ and not quadratically as suggested by Hopkins et al. One reason for this difference, is that we have considered a much larger range of mass ratios over which the thickening is measured. However, we have also noticed several incorrect assumptions in the Hopkins et al. analyses. The mass ratio of the satellite to the disk is clearly of importance in the thickening process: while keeping the other possible parameters fixed the thickening increases visibly for lower disk masses. For our lowest mass dwarf galaxy the disk hardly has an exponential radial density profile any more, the luminosity distribution is more boxy and the disk seems completely destroyed. Therefore such dissipationless mergers with a dark satellite, will turn a disky dwarf into a spheroidal-like system.

In the simulations with gas, the challenge was to establish whether a dark satellite could induce a starburst in a dwarf galaxy. We first focused on setting up a realistic starforming dwarf galaxy. This turned out to be quite difficult: in general most of our systems have too low star formation rates. We have explored varying the parameters characterizing star formation, namely the initial cold gas distribution, the star formation density threshold, the effective equation of state and the fraction of gas present in the disk based upon literature studies and observations. This did affect the star formation rates for the isolated dwarf galaxy only for a short time, on average the star formation rate stayed on a similar low level.

Nonetheless, we performed simulations between two of our starforming dwarfs and a dark satellite. The satellites are placed in the dwarf systems' haloes on four different orbits with inclinations of 0 (planar), 30 and 90 (polar) degrees and a purely radial orbit. For three of these orbits the satellite affects the disk but does not increase the star formation by more than a factor 2 to 3. The satellite on the planar ($i \approx 0$) orbit however, does induce a starburst, with an increase in the star formation by almost a factor of 10. This increase in star formation is at least partly due to the dark satellite accreting gas from the dwarf system and so facilitating star formation in its central region. The starburst is present in the simulations including the dark satellite for both dwarf galaxy models although the star formation rates are lower for the simulations with a lower initial gas fraction.

These simulations show that a dark satellite is very well able to significantly perturb a dwarf galaxy: to thicken the stellar disk and even to induce a starburst. Further research however, should first be done on the isolated dwarf galaxies especially regarding the star formation. When the star formation process and the parameters influencing it are better understood, our understanding of the probability of a dark satellite inducing a starburst in a dwarf galaxies can be significantly improved. For further research we therefore propose to explore the parameters governing the supernovae feedback and possibly different star formation laws. We then will have a better view on how to model a realistic dwarf galaxy that then can be subjected to mergers with dark satellites.

Bibliography

[1] Arp, H., 1965, ApJ, 142, 402
[2] Arp, H., 1966, ApJS, 14, 1
[3] Balsara, D. S., 1995, Journal of Computational Physics, 121, 357
[4] Barnes, J.E., Hernquist, L., 1992, ARA&A, 30, 705
[5] Bate, M. R. and Burkert, A., 1997, MNRAS, 288, 1060
[6] Bekki, K. and Chiba, M., 2006, ApJ, 637, L97
[7] Benson, A. J., Lacey, C. G., Frenk, C. S., Baugh, C. M. and Cole, S., 2004, MNRAS, 351, 1215
[8] Bigiel, F., Leroy, A., Walter, F., et al., 2008, AJ, 136, 2846
[9] Bigiel, F., Leroy, A., Walter, F., et al., 2010, AJ, 140, 1194
[10] Bournaud, F., *Invited lecture at Evry Schatzman School 2010*, 2011, arXiv:1106.1793
[11] Bullock, J. S., Kravtsov, A. V. and Weinberg, D. H., 2000, ApJ, 539, 517
[12] Cox, T.J. Jonsson, P., Somerville, R. S., Primack, J. R. and Dekel A., 2008, MNRAS, 284, 285
[13] Dalcanton, J. J. and Bernstein, R. A., 2002, ApJ, 124, 1328
[14] Dalla Vecchia, C. and Schaye, J., 2008, MNRAS, 387, 1431
[15] Davies, J. I., Disney, M. J., Minchin, R. F., Auld, R. and Smith, R., 2006, MNRAS, 368, 1479
[16] Davies, J., Minchin, R., Sabatini, S., et al., 2004, MNRAS, 349, 922
[17] Dekel, A. and Silk, J., 1986, ApJ, 303, 39
[18] Di Matteo, P., Bournaud, F., Martig, M., et al., 2008, A&A, 492, 31
[19] Di Matteo, P., Combes, F., Melchior, A.-L. and Semelin, B., 2007, A&A, 468, 61
[20] Duc, P.-A., Bournaud, F., 2008, ApJ, 673, 787
[21] Ferland, G. J., 2000, *Revista Mexicana de Astronomia y Astrofisica Conference Series*, 9, 153
[22] Font, A. S., Navarro, J. F., Stadel, J. and Quinn, T., 2001, ApJ, 563, L1
[23] Gilmore, G., Wilkinson, M. I., Wyse, R. F. G., et al., 2007, ApJ, 663, 948
[24] Gingold, R. A. and Monaghan, J. J., 2001, MNRAS, 181, 375
[25] Governato, F., Brook, C., Mayer, L., et al., 2010, Nature, 463, 203
[26] Grebel, E. K., Gallagher, J. S. III and Harbeck, D., 2003, ApJ, 125, 1926
[27] Haardt F. and Madau P., 2001, In *Proc. XXXVIth Recontres de Moriond, Clusters of Galaxies and the High Redshift Universe Observed in X-rays*, eds Neumann, D. M. and Van, J. T. T.
[28] Hayashi, H. and Chiba, M., 2006, Publ. Astron. Soc. Japan, 58, 835
[29] Helmi, A. and White, S. D. M., 2001, MNRAS, 323, 529
[30] Hernquist, L., 1993, ApJS, 86, 389
[31] Hernquist, L. and Katz, N., 1989, ApJS, 70, 419
[32] Hopkins, P. F., Hernquist, L., Cox, T. J., Younger, J. D. and Gurtina, B., 2008, ApJ, 688, 757
[33] House, E. L., Brook, C. B., Gibson, B. K., et al., 2011, MNRAS, 415, 2652
[34] Huang, S. and Carlberg, R. G., 1997, ApJ, 480, 503
[35] Hunter, D. A., Elmegreen, B. G. and Baker, A. L., 1998, ApJ, 493, 595
[36] Ibata, R., Irwin, M., Lewis, G., Ferguson, A. M. N. and Tanvir, N., 2001b, Nature, 412, 491
[37] Ibata, R., Irwin, M., Lewis, G. and Stolte, A., 2001a, ApJ, 547, 133

[38] Immeli, A., Samland, M., Gerhard, O. and Westera, P., 2004, A&A, 413, 547
[39] Kazantzidis, S., Magorrian, J. and Moore, B., 2004, ApJ, 601, 37
[40] Kazantzidis, S., Łokas, E. L., Mayer, L., Knebe, A. and Klimentowski, J., 2011, ApJL, 740, L24
[41] Kazantzidis, S., Zentner, A. R., Kravtsov, A. V., Bullock, J. S. and Debattista, V. P., 2009, ApJ, 700, 1896
[42] Kennicutt, R. C. Jr., 1998, ApJ, 498, 541
[43] Kent, B. R., Giovanelli, R. and Haynes, M. P., 2007, ApJ, 665, L15
[44] Klypin, A., Kravtsov, A. V., Valenzuela, O. and Prada, F., 1999, ApJ, 522, 82
[45] Kormendy, J., 1985, ApJ, 295, 73
[46] Kregel, M. and van der Kruit, P. C., 2005, 2005, MNRAS, 358, 481
[47] Kregel, M., van der Kruit, P. C. and Freeman, K. C., 2005, 358, 503
[48] Larson, R. B., 1974, MNRAS, 169, 229
[49] Lucy, L. B., 1977, Astronomical Journal, 82, 1013
[50] Macciò, A. V., Dutton, A. A. and van den Bosch, F. C., 2008, MNRAS, 391, 1940
[51] Mac Low, M.-M. and Ferrara, A., 1998, In *Lecture Notes in Physics Vol. 506: The Local Bubble and Beyond*, 559, Proceedings of the IAU Colluquium No. 166, ed. Breitschwerdt, D., Freyberg, M. J. and Truemper, J., Springer-Verlag
[52] Mac Low, M.-M. and Ferrara, A., 1999, ApJ, 513, 142
[53] Mayer, L., Governato, F., Colpi, M., et al., 2001a, ApJ, 547, L123
[54] Mayer, L., Governato, F., Colpi, M., et al., 2001b, ApJ, 559, 754
[55] Mayer, L., Moore, B., Quinn, T., Governato, F. and Stadel J., 2002, MNRAS, 336, 119
[56] Mihos, J. C. and Hernquist, L., 1994, ApJ, 437, 611
[57] Mo, H. J., Mao, S. and White, S. D. M., 1998, MNRAS, 295, 319
[58] Monaghan, J. J., 1992, ARA&A, 30, 543
[59] Moore, B., Ghigna, S., Governato, F., et al., 1999, ApJ, 524, L19
[60] Moster, B. P., Macciò, A. V., Somerville, R. S., Johansson, P. H. and Naab, T., 2010, MNRAS, 403, 1009
[61] Muñoz Cuartas, J. C., Macciò, A., Gottlöber, S. and Dutton, A., 2010, In *Proceedings of Cosmic Radiation Fields: Sources in the early Universe (CRF 2010)*, 16, Ed. Raue, M., Kneiske, T., Horns, D., Elsaesser, D. and Hauschildt, P.
[62] Navarro, J. F., Frenk, C. S. and White ,S. D. M., 1996, ApJ, 462, 563
[63] Okamoto, T., Frenk, C. S., Jenkins, A. and Theuns, T., 2010, MNRAS, 406, 208
[64] Okamoto, T. and Frenk, C. S., 2009, MNRAS, 399, L174
[65] Parry, O. H., Eke, V. R., Frenk, C. S. and Okamoto, T., 2011, arXiv:1105.3474
[66] Pelupessy, F. I., van der Werf, P. P. and Icke, V., 2004, A&A, 422, 55
[67] Press, W. H., Schechter, P., 1974, ApJ, 187, 425
[68] Press, W. H., Teukolsky, S. A., Vetterling, W. T. and Flannery, B. P., 1992, *Numerical recipes. The art of scientific computing*, Cambridge: University Press
[69] Purcell, C. W., Kazantzidis, S. and Bullock, J. S., 2009, ApJ, 694, L98
[70] Qu, Y., Di Matteo, P., Lehnert, M. D. and van Driel, W., 2011, A&A, 530, 10
[71] Quinn, P. J. and Goodman, J., 1986, ApJ, 309, 472
[72] Quinn, P. J., Hernquist, L. and Fullagar, D. P., 1993, ApJ, 403, 74
[73] Read, J. I., Pontzen, A. P. and Viel, M, 2006, MNRAS, 371, 885
[74] Rees, M. J. and Ostriker, J. P., 1977, MNRAS, 179, 541
[75] Ricotti, M., 2009, MNRAS, 392, L45
[76] Roychowdhury, S., Chengalur, J. N., Begum, A. and Karachentsev, I. D., 2009, MNRAS, 397, 1435
[77] Saitoh, T. R., Daisaka, H., Kokubo, E., et al., 2008, Publ. Astron. Soc. Japan, 60, 667

[78] Sales, L. V., Helmi, A., Starkenburg, E., et al. in prep.
[79] Sales, L. V., Navarro, J. F., Abadi, M. G. and Steinmetz, M., 2007, MNRAS, 379, 1475
[80] Sawala, T., Guo, Q., Scannapieco, C., Jenkins, A. and White, S., 2011, MNRAS, 413, 659
[81] Sawala, T., Scannapieco, C., Maio, U. and White S., 2010, MNRAS, 402, 1599
[82] Schaye, J., 2004, ApJ, 609, 667
[83] Schaye, J. and Dalla Vecchia, C., 2008, MNRAS, 383, 1210
[84] Schweizer, F., 1990, In *Dynamics and Interactions of Galaxies*, ed. Wielen, R., Springer, 60, New York
[85] Sofue, Y., 1994, ApJ, 423, 207
[86] Somerville, R. S., 2002, ApJ, 592, L23
[87] Springel, V., 2005, MNRAS, 364, 1105
[88] Springel, V., Di Matteo, T. and Hernquist, L., 2005, MNRAS, 361, 776
[89] Springel, V., Frenk. C. S. and White, S. D. M., 2006, Nature, 440, 1137
[90] Springel, V., Yoshida, N. and White, S. D. M., 2001, New Astronomy, 6, 79
[91] Springel, V., Wang, J., Volgesberger, M., et al., 2008, MNRAS, 391, 1685
[92] Springel, V. and White, S. D. M., 1999, MNRAS, 307, 162
[93] Springel, V., White, S. D. M., Jenkins, A., et al., Nature, 435, 629
[94] Stinson, G. S., Dalcanton, J. J., Quinn, T., Kaufmann, T. and Wadsley, J., 2007, ApJ, 667, 170
[95] Starkenburg, E., et al., 2011, in prep.
[96] Steinmetz, M., 1996, MNRAS, 278, 1005
[97] Strigari, L. E., Bullock, J. S., Kaplinghat, M., et al., 2007, ApJ, 669, 676
[98] Strigari, L. E., Bullock, J. S., Kaplinghat, M., et al., 2008, Nature, 454, 1096
[99] Swaters, R. A., van Albada, T. S., van der Hulst, J. M. and Sancisi, R., 2002, A&A, 390, 829
[100] Tamman G. A., 1994, In *Dwarf Galaxies*, 3, ed. Meylan, G. and Prugniel, P., Eur. South. Obs. Astrophys. Symp., 49, Garching: ESO
[101] Tasker, E. J. and Bryan, G. L., ApJ, 673, 810
[102] Tolstoy, E., Hill, V. and Tosi, M., 2009, ARA&A, 47, 371
[103] Toomre, A., 1977, In *The Evolution of Galaxies and Stellar Populations*, eds. Tinsley, B. M., and Larson, R. B., Yale University Observatory
[104] Toomre, A. and Toomre, J., 1972, ApJ, 178, 623
[105] Toth, G. and Ostriker, J. P., 1992, ApJ, 389, 5
[106] Trentham, N., MÃűller, O.and Ramirez-Ruiz, E., 2001, MNRAS, 322, 658
[107] Van der Kruit, P. C. and Freeman, K. C., 2011, ARA&A, 49, 301
[108] Velázquez, H. and White, S. D. M., 1999, MNRAS, 304, 254
[109] Verde, L., Heavens, A. F., Percival, W. J., et al., 2002, MNRAS, 335, 432
[110] Villalobos, Á. and Helmi, A., 2008, MNRAS, 391, 1806
[111] Wadepuhl, M. and Springel, V., 2011, MNRAS, 410, 1975
[112] Walker, M. G., Mateo, M., Olszewski, E. W., et al., 2009, ApJ, 704, 1274
[113] Walker, I. R., Mihos, J. C. and Hernquist, L., 1996, ApJ, 460, 121
[114] Walter, F. and Brinks, E., 2001, Astronomical Journal, 121, 3026
[115] Weisz, D. R., Dalcanton, J. J. and Williams, B. F., 2011, ApJ, 739, 5
[116] White, S. D. M. and Rees, M. J., 1978, MNRAS, 183, 341
[117] Wilman, R. J., Gerssen, J., Bower, R. G., et al., 2005, Nature, 438, 227
[118] Xu, G., 1995, ApJS, 98, 355
[119] Young, L. M., Skillman, E. D., Weisz, D. R. and Dolphin A. E., 2007, ApJ, 659, 331
[120] Younger, J. D., Hopkins, P. F., Cox, T. J. and Hernquist, L., 2008, ApJ, 686, 815

Chapter 7

Acknowledgements

Though this thesis is finished, and I will be graduating next week, I feel like I'm not really up to writing acknowledgements at this point. First of all, I have to confess that I do not feel like I am finishing something. I will continue the research presented above in the coming years (as still much is to be done!), at the same institute with almost the same people. I still find the subject of merging dwarf galaxies and dark satellites very interesting and I am very much looking forward to continue with the science discussions, new analyses and new simulations now that the writing is finished (for the moment).

Secondary, as I (hopefully) will continue working with the people I worked with for this project I do not want to just say 'thank you'. Amina, I am very grateful for your guidance and support, for our discussion and the inspiration I got from them. But more than this I would like to say that I very much enjoy working with you and that I am very much looking forward to continue working with you for the next years!

Laura and Claudio, thanks a lot for letting me visit you in Munich, for advising and supporting me, for providing me with code and for always being willing to answer my questions. I would very much like to work with you again. Thanks, particulary for the reasearch presented in this thesis, also goes to Alvaro Villalobos and Volker Springel for providing code and to Joop Schaye for some useful discussions and comments.

I really enjoyed the useful and the funny discussions I had with everyone from Amina's group, the Kapteyn students, my family and friends and especially Else and Roel. Discussions do not have to be about science to help you in your research! I would love to continue these with you all in the future.